

Diffuse Reflectance Spectroscopy Characterization for Extraction of Tissue Physiological

Parameters

by

Janelle Elise Phelps

Department of Biomedical Engineering
Duke University

Date: _____

Approved:

Nirmala Ramanujam, Supervisor

Tuan Vo-Dinh

Adam P. Wax

Mark W. Dewhirst

Allan B. Shang

Dissertation submitted in partial fulfillment of
the requirements for the degree of Doctor of Philosophy in the Department of
Biomedical Engineering in the Graduate School of
Duke University

2010

ABSTRACT

Diffuse Reflectance Spectroscopy Characterization for Extraction of Tissue Physiological

Parameters

by

Janelle Elise Phelps

Department of Biomedical Engineering
Duke University

Date: _____

Approved:

Nirmala Ramanujam, Supervisor

Tuan Vo-Dinh

Adam P. Wax

Mark W. Dewhirst

Allan B. Shang

An abstract of a dissertation submitted in partial fulfillment of
the requirements for the degree of Doctor of Philosophy in the Department of Biomedical
Engineering in the Graduate School of
Duke University

2010

Copyright by
Janelle Elise Phelps
2010

Abstract

Variations in hemoglobin concentration can be indicative of a number of serious complications, including blood loss and anemia. Rapid, noninvasive measurements of hemoglobin are important in applications where blood status is reflective of patient well-being, such as in the emergency room, operating room, or the battlefield. Probe-based diffuse reflectance spectroscopy is capable of noninvasively quantifying tissue optical properties, including hemoglobin concentration. The quantification of hemoglobin concentration using optical methods is complicated by tissue scattering and the robustness of the algorithm and instrumentation used to interrogate the tissue. The sensing depth of diffuse reflectance spectroscopy can be tailored by the wavelengths of light and probe design used.

In this thesis, the accuracy and clinical viability of different diffuse reflectance spectroscopy implementations are presented. The robustness of an inverse Monte Carlo model, in which tissue optical properties are determined from measured reflectance using ultraviolet-visible (UV-VIS) wavelengths and a steady-state instrument, was tested using laboratory measurements. From the laboratory measurements, a set of references was identified which provided accurate absorption and scattering measurements, independent of the optical properties of the target. In addition, the ability to quantify hemoglobin concentration and saturation over large ranges and concentrations of multiple absorbers was established.

Following the laboratory measurements, a clinical study in which UV-VIS spectra were measured from the sublingual mucosa of patients undergoing surgeries was carried out. From this study, the correlations of extracted hemoglobin to expected blood hemoglobin were found to be improved when a simple ratiometric method based on isosbestic wavelengths of hemoglobin was used. During this study, the probe positioning in the mouth was found to be unwieldy, and so the transition to a more secure probe that could be taped to the hand was made.

In order to penetrate the overlying skin, near-infrared (NIR) wavelengths with a different probe geometry was explored. Further investigation of the inverse Monte Carlo model with NIR wavelengths was executed, and while in theory this combination should yield accurate optical property estimation, laboratory measurements indicated large errors, presumably due to the instrument or low magnitude and reduced spectral features of hemoglobin absorption in the NIR. Instead, the use of a well-established frequency-domain instrument coupled with diffusion approximation was implemented to measure spectra from the thenar eminence of volunteers undergoing induced hypovolemia and subsequent retransfusion. There were some moderate correlations with blood hemoglobin, but because both this method and the Monte Carlo method with mucosal probe placement showed higher variability with probe pressure than the isosbestic ratiometric method, further development of the ratiometric method was made.

The ratiometric method was developed using simulations and validated with phantoms and clinical data. Monte Carlo modeled reflectance was generated for a large range of biologically-relevant absorption and scattering values. The modeled reflectance was scaled by a calibration spectra obtained from a single laboratory phantom measurement so that linear regression equations relating hemoglobin concentration to ratios could be applied directly to clinical or laboratory measurements. Ratios which could best estimate hemoglobin concentration independent of saturation and scattering were determined through the simulation and laboratory measurements. Three isosbestic ratios - 545/390, 452/390, and 529/390 nm - were determined to best estimate hemoglobin concentration, and ratiometric-extracted hemoglobin was shown to correlate well to Monte Carlo-extracted hemoglobin in clinical measurements. Because only a single calibration measurement (which can be measured on a different day) is required per instrument and probe combination, this method can be implemented in near real-time and is thus appropriate for applications where hemoglobin concentration must be measured rapidly.

Contents

| | |
|---|-----|
| Abstract..... | iv |
| List of Tables..... | x |
| List of Figures..... | xii |
| Symbols/Abbreviations | xv |
| Acknowledgements..... | xvi |
| 1. Introduction..... | 1 |
| 1.1 Clinical Problem: Quantitative Measurements of Hemoglobin | 1 |
| 1.2 Hemoglobin | 2 |
| 1.3 Invasive Measurements of Hemoglobin Concentration and Saturation | 3 |
| 1.4 Diffuse Reflectance Spectroscopy..... | 4 |
| 1.5 Assessment of the Robustness of the Inverse Monte Carlo Algorithm | 8 |
| 1.6 Noninvasive Measurements of Hemoglobin Concentration and Saturation | 10 |
| 1.7 Probe-Tissue Interfacing..... | 13 |
| 1.8 UV-VIS Measurements of the Sublingual Mucosa During Surgery | 15 |
| 1.9 NIR Measurements of the Thenar Eminence During Induced Hypovolemia | 17 |
| 1.10 Ratiometric Method to Estimate Hemoglobin..... | 18 |
| 1.11 Major Outcomes | 21 |
| 2. Assessment of the Robustness of the Inverse Monte Carlo Model | 23 |
| 2.1 Introduction | 23 |
| 2.2 Methods | 23 |
| 2.2.1 Phantom Preparation and Calculations | 23 |
| 2.2.2 Phantom Variations..... | 25 |
| 2.2.2.1 Single absorber phantoms | 26 |
| 2.2.2.2 Double absorber phantoms | 27 |

| | |
|--|----|
| 2.2.2.3 Hemoglobin saturation phantoms | 28 |
| 2.2.2.4 Hemoglobin concentration phantoms..... | 29 |
| 2.2.3 Optical Measurements | 29 |
| 2.3 Results..... | 30 |
| 2.3.1 Single Absorber Phantoms..... | 30 |
| 2.3.2 Double Absorber Phantoms..... | 34 |
| 2.3.3 Hemoglobin Concentration Phantoms | 35 |
| 2.3.4 Hemoglobin Saturation Phantoms..... | 36 |
| 2.4 Discussion | 38 |
| 3. <i>In Vivo</i> Diffuse Reflectance Measurements from the Sublingual Mucosa in Patients Undergoing Surgery | 41 |
| 3.1 Introduction | 41 |
| 3.2 Methods | 41 |
| 3.2.1 Patient Study | 41 |
| 3.2.2 Optical Measurements | 43 |
| 3.2.3 Data Analysis | 43 |
| 3.2.3.1 Inverse Monte Carlo model | 43 |
| 3.2.3.2 Ratiometric method | 44 |
| 3.2.4 Probe Pressure in Volunteers | 44 |
| 3.3 Results..... | 46 |
| 3.3.1 Inverse Monte Carlo Model | 46 |
| 3.3.2 Ratiometric Method | 46 |
| 3.3.3 Simulations | 52 |
| 3.3.4 Probe Pressure in Volunteers | 55 |
| 3.4 Discussion | 58 |
| 4. NIR Measurements Using an Inverse Monte Carlo Model and a Steady-State System..... | 62 |

| | |
|--|----|
| 4.1 Introduction | 62 |
| 4.2 Methods | 64 |
| 4.2.1 Simulated NIR Data from Phantoms..... | 64 |
| 4.2.2 Phantoms..... | 68 |
| 4.3 Results..... | 70 |
| 4.3.1 Simulated NIR Data from Phantoms..... | 70 |
| 4.3.2 Phantoms..... | 73 |
| 4.4 Discussion | 75 |
| 5. <i>In Vivo</i> Diffuse Reflectance Measurements from the Thenar Eminence in Volunteers Undergoing Hypovolemia..... | 79 |
| 5.1 Introduction | 79 |
| 5.2 Methods | 79 |
| 5.2.1 Patient Study | 79 |
| 5.2.2 Optical Measurements | 83 |
| 5.2.3 Data Analysis | 83 |
| 5.2.4 Probe Pressure in Volunteers | 84 |
| 5.3 Results..... | 85 |
| 5.3.1 Correlations with Arterial Blood Gas Hemoglobin Concentration | 85 |
| 5.3.2 Correlations with Other Noninvasive Measures of Hemoglobin Concentration..... | 87 |
| 5.3.3 Correlations with Other Noninvasive Measures of Hemoglobin Saturation | 89 |
| 5.3.3 Probe Pressure in Volunteers | 90 |
| 5.4 Discussion | 92 |
| 6. Development of a Ratiometric Method to Estimate Hemoglobin Concentration..... | 94 |
| 6.1 Introduction | 94 |
| 6.2 Methods | 94 |
| 6.2.1 Determination of the Best Ratios Using Monte Carlo Simulations..... | 96 |

| | |
|---|-----|
| 6.2.2 Testing on Synthetic Tissue-Mimicking Phantoms | 98 |
| 6.2.3 Sensitivity Analysis | 101 |
| 6.2.4 Clinical Applicability | 102 |
| 6.3 Results..... | 102 |
| 6.3.1 Determination of the Best Ratios | 102 |
| 6.3.2 Testing: Phantoms with Variable Hemoglobin Saturation | 104 |
| 6.3.3 Testing: Phantoms with Variable Scattering and Hemoglobin Concentration..... | 105 |
| 6.3.4 Sensitivity Analysis | 107 |
| 6.3.5 Clinical Applicability | 108 |
| 6.4 Discussion | 109 |
| 7. Conclusions and Future Directions | 114 |
| 7.1 Conclusions | 114 |
| 7.2 Future Directions | 117 |
| Appendix A: Neutron Stimulated Emission Computed Tomography for the Diagnosis of Breast Cancer..... | 120 |
| A.1 Introduction | 120 |
| A.2 Methods | 121 |
| A.2.1 Simulations | 121 |
| A.2.2 Peak-Identification Algorithm | 123 |
| A.2.3 ROC Analysis..... | 124 |
| A.2.4 Dose Calculations..... | 125 |
| A.3 Results..... | 125 |
| A.4 Discussion | 128 |
| References | 131 |
| Biography | 140 |

List of Tables

| | |
|---|-----|
| Table 1: Advantages and disadvantages for diffuse reflectance measurements from the sublingual tissue and thenar eminence. | 15 |
| Table 2: Comparisons of the advantages and disadvantages associated with the isosbestic ratiometric method and pulse oximetry. | 21 |
| Table 3: Absorber and scatterer levels used in single absorber (hemoglobin) phantoms. | 26 |
| Table 4: Absorber levels used in single absorber (crocin) phantoms. | 27 |
| Table 5: Absorber levels used in double absorber (hemoglobin and crocin) phantoms. | 27 |
| Table 6: Absorber and scattering levels used for phantoms spanning a large range of concentrations. | 29 |
| Table 7: Average percent errors for single-absorber hemoglobin and crocin phantoms. | 31 |
| Table 8: Absorber-scatterer levels with corresponding wavelength-averaged optical properties for the 11 master reference phantoms, which had <10% error in μ_a and μ_s' | 33 |
| Table 9: Extraction accuracy using master reference phantoms common to SA_Hb_a and SA_Hb_b across all targets for difference probe and instrument combinations. | 34 |
| Table 10: Types of surgeries, number of ABG and optical measurements, and range of hemoglobin obtained from the ABG. | 43 |
| Table 11: Average percent errors for μ_a and μ_s' using diffuse reflectance generated from 600-900 nm with a forward- and side-firing geometry probe. | 72 |
| Table 12: Average percent errors in μ_a and μ_s' for inversions from 450-600 and 600-800 nm in phantom studies. | 74 |
| Table 13: Volunteer demographics and number and range of hemoglobin obtained from the ABG. | 82 |
| Table 14: r values for correlations between hemoglobin saturation measured with the frequency-domain system and the three VIS probes. | 90 |
| Table 15: Concentrations of oxy- and deoxyhemoglobin used in the Monte Carlo simulations. . | 97 |
| Table 16: μ_s' for each of the five scattering levels as a function of isosbestic wavelength. The scattering levels were selected to be approximately evenly spaced by 5 cm^{-1} per level. | 97 |
| Table 17: %error for the simulations and the three testing phantom sets. | 107 |
| Table 18: Ranges of scattering slope, b , for which the six best ratios were still considered best ratios. | 107 |

| | |
|--|-----|
| Table 19: Average percent error when $g=0.7$, 0.9 , and 0.95 were used for Sets 1-3 measured with the CCD-based instrument..... | 108 |
| Table 20: Applications of the ratiometric isosbestic method, which can provide rapid measurements of hemoglobin concentration | 113 |
| Table 21: Percent composition of the four major elements and twelve primary trace elements in normal and malignant breast tissue..... | 122 |
| Table 22: Energy levels for the isotopes that registered in over half of the normal or malignant models using the peak identification algorithm..... | 126 |
| Table 23: ROC A_z values for each of the 10 isotopes determined to be peaks in over half of the normal or malignant models for each of the six incident neutron levels. | 127 |

List of Figures

| | |
|---|----|
| Figure 1: Effects of temperature, pH, and pCO ₂ on the oxygen-hemoglobin dissociation curve. | 3 |
| Figure 2: Extinction coefficients for oxy- and deoxyhemoglobin from 350-600 nm | 18 |
| Figure 3: Error grids for μ_a (top) and μ_s' (bottom) for all reference-target combinations in the single absorber phantoms. | 32 |
| Figure 4: Extraction accuracy of hemoglobin (top) and crocin (bottom) in DA_HbCr when five master reference phantom measured on a different day were used. | 35 |
| Figure 5: Extraction accuracy of hemoglobin using same-day master reference phantoms..... | 36 |
| Figure 6: Extracted HbO ₂ and HbH as a function of measured pO ₂ (top) and extracted vs. expected hemoglobin saturation (bottom)..... | 37 |
| Figure 7: Photograph of the optical probe with tubing applied for the volunteer measurements. | 45 |
| Figure 8: Monte Carlo-extracted total hemoglobin versus ABG hemoglobin for all 10 patients combined. | 46 |
| Figure 9: Grids showing the strength of linear correlation between ABG hemoglobin and all numerator-denominator optical ratios..... | 48 |
| Figure 10: 529/500 nm (top) and 520/509 nm (bottom) with versus ABG hemoglobin for all 10 patients combined. | 50 |
| Figure 11: Feasibility for hemoglobin monitoring over time using the 529/500 nm optical ratio. | 52 |
| Figure 12: Relationship between 529/500 nm and hemoglobin concentration as determined from simulations..... | 54 |
| Figure 13: Diffuse reflectance for Volunteer 1 (top) and Volunteer (2) for the Right 1 site per pressure..... | 56 |
| Figure 14: Monte Carlo-extracted hemoglobin (top), 529/500 (middle), and 520/509 nm (bottom) for Volunteer 1 (left) and Volunteer 2 (right) as a function of increasing probe pressure per site. | 57 |
| Figure 15: Flow chart summarizing the steps taken to assess the feasibility of Monte Carlo on steady-state measurements at NIR wavelengths. | 63 |
| Figure 16: Phantom-extracted μ_a (top) and μ_s' (bottom) from 350-600 nm (solid blue line) and corresponding extrapolated optical properties (dashed black line) from 600-900 nm. | 66 |
| Figure 17: Probe geometries for the forward- (top) and side-firing (bottom) probes..... | 67 |

| | |
|--|-----|
| Figure 18: Computer model of the top piece for the probe-reflectance standard adaptor. | 69 |
| Figure 19: Diffuse reflectance generated for the forward- (top) and side-firing (bottom) probes from 350-900 nm. | 71 |
| Figure 20: Extracted versus expected μ_a (left) and μ_s' (right) for different-day reference-target inversions using extrapolated data from 600-900 nm. | 73 |
| Figure 21: Errors in μ_a and μ_s' for 600-800 nm using different-day reference-target phantoms. | 75 |
| Figure 22: Average percent errors in μ_s' for the steady-state (top) and frequency-domain (bottom) phantoms inverted with different-day references. | 76 |
| Figure 23: Measurements made on the reflectance standard with different probe cleaning methods..... | 78 |
| Figure 24: Photograph showing the setup of the hypovolemia study; the arrow indicates where the NIR probe was securely taped. | 80 |
| Figure 25: Timeline illustrating when each clinical data point (yellow box) and arterial blood gas (green box) were taken..... | 81 |
| Figure 26: Total hemoglobin concentration as extracted from the optical measurements versus ABG hemoglobin for subjects 1-5. | 85 |
| Figure 27: Total hemoglobin concentration as extracted from the optical measurements versus ABG hemoglobin for subjects 6-15, and separated by gender (top) and BMI (bottom). | 86 |
| Figure 28: Correlation of NIR and Casmel hemoglobin for subjects 1-5 (top) and 6-15 (bottom). | 88 |
| Figure 29: Baseline-subtracted concentrations averaged over all volunteers for each clinical data point. | 89 |
| Figure 30: Diffusion approximation-extracted hemoglobin for Volunteer 1 (top) and Volunteer 2 (bottom) as a function of increasing probe pressure per site..... | 91 |
| Figure 31: Flowchart summarizing steps taken to find and test the best ratios. | 95 |
| Figure 32: Expanded flowchart illustrating the steps taken for testing the best ratios from the simulations. | 100 |
| Figure 33: Histogram showing the %error from the simulations for ratios with %error within 20%. | 103 |
| Figure 34: Hemoglobin versus averaged ratio for the 545/390 nm, which had the lowest %error of 2.3%. | 103 |
| Figure 35: %error with corresponding standard deviation for Phantom Set 1 for the 25 best ratios from the simulations. | 104 |

Figure 36: %error for Phantom Set 2 (top) and Phantom Set 3 (bottom) measured with the CCD-based instrument. 105

Figure 37: %error for Phantom Set 2 (top) and Phantom Set 3 (bottom) measured with the PMT-based instrument. 106

Figure 38: Monte Carlo and ratiometrically-extracted hemoglobin concentration for the three best ratios from the simulations and phantoms: 545/390 (top), 452/390 (middle), and 529/390 nm (bottom) for the *in vivo* cervical measurements. 109

Figure 39: Orientation of the bulk breast tissue and surrounded HPGe detectors used in the Monte Carlo simulations. 121

Figure 40: Peak-identification results from one of the 10 million incident neutron simulations for normal breast tissue. 124

Figure 41: Average A_z values for the five prominent energy levels as a function of number of incident neutrons. 127

Figure 42: Combined normal (blue) and malignant (red) spectra with arrows indicating the five isotopes which were found to have high discriminatory ability. 128

Symbols/Abbreviations

| | |
|------------------|---|
| BMI | Body mass index |
| BP | Bandpass |
| CCD | Charge-coupled device |
| Cr | Crocin |
| DOS | Diffuse optical spectroscopy |
| FD | Frequency-domain |
| Hb | Hemoglobin |
| HbH | Deoxyhemoglobin |
| HbO ₂ | Oxyhemoglobin |
| NA | Numerical aperture |
| NIR | Near-infrared wavelengths (700-2500 nm) |
| NSECT | Neutron Stimulated Emission Computed Tomography |
| PMT | Photomultiplier tube |
| pO ₂ | Partial pressure of oxygen |
| ROC | Receiver Operating Characteristic |
| RTE | Radiative Transfer Equation |
| SS | Steady-state |
| UV | Ultraviolet wavelengths (10-400 nm) |
| VIS | Visible wavelengths (400-700 nm) |
| μ_a | Absorption coefficient |
| μ_s' | Reduced scattering coefficient |

Acknowledgements

I would first like to acknowledge the amazing mentorship I received from the two advisors I had while pursuing my Ph.D. at Duke University. Dr. Carey E. Floyd was a patient and kind mentor who I can thank for helping me get into Duke in the first place. Carey was a compassionate teacher, and his love for his work encouraged me to be a better scientist. Unfortunately, Carey passed away in August 2006 from cancer. The mentoring I received from him in my formative years of graduate school helped define me as the scientist I am today. The appendix of this document is a publication I wrote on the research I did in Carey's lab.

In light of Carey's untimely passing, I had the privilege to join Dr. Nirmala (Nimmi) Ramanujam's lab. I admire Nimmi for the amount of enthusiasm and drive she has for her research. She has always been there for me, and I appreciate the opportunity to learn and grow as a part of her lab. Although the mentoring styles of Carey and Nimmi could not have been more different, they both helped me grow and identify my strengths and weaknesses, which have led me towards my future goals.

Also, I owe a big thanks to Drs. Allan Shang and Gene Moretti. As clinical collaborators for the surgery study, you both really opened my eyes to what goes on in the operating room. I never would have guessed that I would get to be in the room during actual surgeries, and that turned out to be one of my favorite parts of graduate school! I always have had an interest in the medical field and surgery; being able to experience that in conjunction with engineering was extremely interesting. You both are great collaborators, and I thank you for all your scientific input and for just getting us in the clinic!

I would also like to thank my lab mates from Carey and Nimmi's labs. Never have I had the opportunity to work with a group of such intelligent individuals who were always ready to lend a helping hand. In particular, the post-docs in Nimmi's lab - Karthik Vishwanath, Quincy Brown, and Bing Yu - these three guys are the most helpful and smartest people I've had the

honor to work with! In addition, I want to acknowledge Stacy Millon, who is not only a lab member but a great friend. And Stacy...you do owe me that bottle of wine; I always told you we would defend around the same time!

Finally, but most importantly, I want to thank my parents, Jeff and Jenny Bender, my sister, Jessica Bender, my grandmother, Granny, and my husband, Andrew Phelps. Each of you have been there for me through thick and thin, and by believing in me (probably more than I believe in myself), you have all helped me tremendously in this long path to the Ph.D. I thank you all for your patience, love, and for reading my publications! To you especially Andrew; your love and support when you are near and far has helped me exponentially in both grad school and in life in general. I love you!

1. Introduction

1.1 Clinical Problem: Quantitative Measurements of Hemoglobin

Hemoglobin concentration is a metric used for many applications in the medical field, including anemia diagnosis and blood transfusion guidance. The current standard-of-care for determining hemoglobin concentration is invasive, where blood is drawn from an artery and sent to a laboratory for further analysis. This process is time-consuming, subject to operator error, and carries the risk of infection. Therefore the need exists for a non-invasive technique that can rapidly and accurately predict hemoglobin concentration in human and/or animal tissues. If such a device and method were portable, it would have wide applicability in various areas where rapid hemoglobin measurements are required, such as in the emergency or operating room, in the back of an ambulance, in the battlefield, and in less developed countries for blood screening. To assess the status of a patient undergoing surgery, measurements of both hemoglobin saturation and concentration are important, because even in cases of extreme anemia the saturation can still be at a normal level. The hemoglobin saturation gives an indication of how well-ventilated a patient is, but to determine the amount of oxygen present in the blood, the concentration must be known [1].

Additionally, hemoglobin concentration could serve as a surrogate indicator for neovascularization. In cervical dysplasia, neovascularization has been shown to be associated with poor prognosis and is has been linked to greater risk of recurrence and death [2, 3]. Early angiogenic changes are also indicative of neoplastic changes in different organ sites, including the prostate [4], head and neck [5], and gastrointestinal systems [6]. Characterization of neovascularization has mostly been performed by invasive and tissue destructive immunohistochemistry on formaldehyde-fixed and paraffin-embedded tissues using various antibodies [7], and so the need exists for a noninvasive method of measuring neovascularization.

Diffuse reflectance spectroscopy, which utilizes light delivered and collected through a fiber optic probe, has the capability to measure hemoglobin concentration noninvasively and without causing damage to the tissue [8]. The studies in this thesis have investigated and validated different implementations of diffuse reflectance spectroscopy and analytical methods in the laboratory and clinic. A ratiometric method, based on simple ratios of diffuse reflectance has been shown to provide accurate measurements of hemoglobin concentration independent of scattering and hemoglobin saturation [9]. The results from these studies provide guidance for future studies using diffuse reflectance spectroscopy. The combination of wavelengths used, instrumentation, biological site, and analytical method have impact on the ability to noninvasively measure hemoglobin from tissue.

1.2 Hemoglobin

Hemoglobin is responsible for oxygen transport in red blood cells of humans and other vertebrates. The heme molecule is protoporphyrin IX (PpIX) containing an iron atom. Each heme molecule in hemoglobin is connected with four globin chains. The formation of heme is highly regulated and a disruption to the heme cycle can be indicative of a number of medical conditions or complications [10]. For example, anemia occurs when there is less iron available to couple with the PpIX molecule. A classification of diseases called porphyrias can occur due to malfunctions at various stages of heme synthesis. Lead poisoning can inhibit the ferrochelatase enzyme, which controls the final stage of heme synthesis where iron is incorporated into PpIX. The concentration of hemoglobin in the blood is the product of the volume fraction of erythrocytes in the blood and the total concentration of hemoglobin in them [11]. The fraction of erythrocytes in the blood is also referred to as hematocrit.

Hemoglobin has the ability to reversibly bind with oxygen molecules to form oxyhemoglobin. The unbound form is referred to as deoxyhemoglobin. While heme synthesis occurs in the mitochondria and cytosol of all normal mammalian cells, it does not occur in the mature erythrocyte. The delivery of oxygen to different parts of the body is dependent upon

the blood oxygen content, and it is the task of the erythrocyte, or red blood cell, to carry this oxygen. The percent saturation, or hemoglobin saturation, is the amount of oxygen being carried by hemoglobin. The oxygen-hemoglobin dissociation curve gives the relationship between hemoglobin saturation and the partial pressure of oxygen, pO_2 . It has a sigmoidal shape, where low saturation (i.e. less oxygen bound) corresponds to low pO_2 . The steep portion of the curve describes the rapid unloading of oxygen when the pO_2 drops below a certain level. As illustrated in Figure 1, the curve can be shifted by various factors that influence the affinity of oxygen binding to hemoglobin, such as temperature, pH, and partial pressure of CO_2 (pCO_2) [1, 12]. The partial pressure at which hemoglobin is 50% saturated, or p_{50} , indicates the degree of pO_2 required to maintain 50% oxygen saturation. When the curve shifts, the p_{50} subsequently is affected.

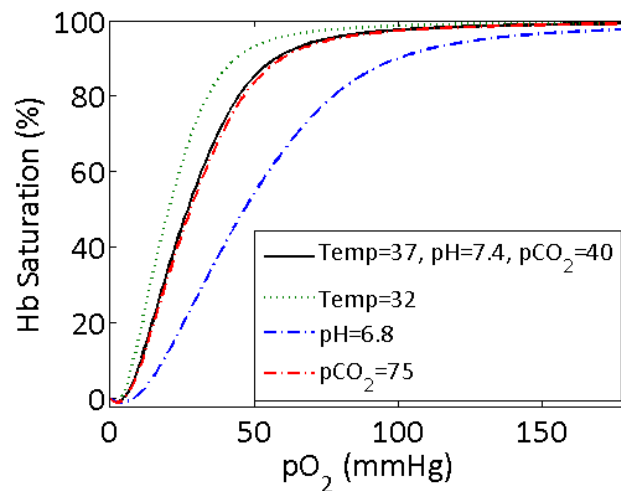


Figure 1: Effects of temperature (“Temp”), pH, and pCO_2 on the oxygen-hemoglobin dissociation curve. Temperature is shown in degrees Celsius and pCO_2 is shown in mmHg. A decrease in temperature causes a leftward shift of the curve, while a decrease in pH or increase in pCO_2 causes a rightward shift.

1.3 Invasive Measurements of Hemoglobin Concentration and Saturation

The process of measuring hemoglobin concentrations in *ex vivo* blood samples is relatively straight-forward, as the desired component(s) of blood can be removed from the

body. Invasive measurements of hemoglobin concentration typically involve the analysis of a blood sample by a CO-oximeter. The typical CO-oximeter operates through the use of multiple wavelengths of light, where transmission of light through a blood sample is measured with a photodetector, then used to calculate absorbance and concentration [13]. The addition of more wavelengths allows for the assessment of more analytes. The transmission can be used to calculate hemoglobin concentration using Beer's Law, which relates transmission (T) to extinction coefficient (ϵ) and concentration (c) by:

$$T = \frac{I}{I_0} = 10^{-\epsilon cl} \quad (1)$$

L is the path length and I and I_0 are the transmitted and incident light intensity, respectively. The absorbance is related to transmission and thus the extinction coefficient and concentration by:

$$A = \log\left(\frac{1}{T}\right) \quad (2)$$
$$A = \epsilon cl$$

Measurements of hemoglobin saturation generally involve a blood gas analyzer, which measures the pO_2 with an oxygen-sensitive electrode. The pO_2 is then used to calculate the hemoglobin saturation, based on empirical formulae developed by the manufacturers of the blood gas machines [1]. Alternatively, the fractional or functional oxygen saturation can be calculated using a CO-oximeter. The fractional saturation is the ratio of oxyhemoglobin to all hemoglobin, whereas functional saturation is the ratio of oxyhemoglobin to all other functional hemoglobin. In other words, the fractional saturation includes the contribution of dyshemoglobins, such as methemoglobin [14].

1.4 Diffuse Reflectance Spectroscopy

Probe-based diffuse reflectance spectroscopy can be used to noninvasively measure structural and functional properties of tissue. When light is shone into a turbid medium such as

biological tissue, it is diffusely reflected. The propagation of light in the medium is dependent upon the absorption (μ_a) and reduced scattering (μ_s') coefficients of the tissue, where μ_a relates to the concentration of chromophores in the tissue, and μ_s' describes the size and density of scattering centers. The primary absorber in the tissue is hemoglobin, and because the absorption shape of oxy- and deoxyhemoglobin are different, diffuse reflectance spectroscopy can be used to differentiate between the two thus providing independent concentration measurements and a calculated hemoglobin saturation [15]. One of the primary tasks of tissue optics is to determine the μ_a and μ_s' from the measured reflectance. Light is both absorbed and scattering by blood and other tissue structures, and so a model of light propagation is required to deconstruct the reflectance spectrum [15]. The Radiative Transfer Equation (RTE) is an energy balance equation that can mathematically describe light propagation in tissue [16]. The RTE accounts for losses due to divergence plus absorption and scattering away from the incident beam, as well as gains due to the light source and scattering directed towards the beam, but because the RTE cannot be solved analytically, assumptions must be made to provide approximations.

Empirical methods, the diffusion approximation to the RTE, and Monte Carlo are all methods which can be used to model light propagation in tissue. The diffusion approximation is applicable when the source-detector separation is large enough and the absorption contrast is much lower than the scattering (i.e. in the NIR) [8]. It is an analytical approximation to the RTE using boundary conditions and assumptions that the source is quasi-isotropic, and that the time variation of the source is slow relative to the mean photon collision time [17]. Monte Carlo is a numerical modeling technique for the RTE, which is valid for a larger range of wavelengths and optical properties than the diffusion approximation, but it suffers from computational time [18]. The Monte Carlo method involves random sampling of probability density functions related to the absorption and scattering characteristics of a medium. Diffuse reflectance spectroscopy can be measured using steady-state (SS), frequency-domain (FD), or time-domain

instrumentation. Because only SS and FD methods were used in the research discussed in this dissertation, the discussion will be limited to those methods.

SS diffuse reflectance in the UV-VIS involves either a broadband or monochromatic source. The diffuse reflectance contains information about the wavelength-dependent absorption and scattering properties of the tissue. The typical instrumentation of a diffuse reflectance system consists of a broadband light source and a detector, both of which are coupled to a fiber probe and controlled with a laptop computer. Because the SS diffuse reflectance measurements described here were taken in the UV-VIS, where the magnitude of scattering and absorption are comparable, the diffusion approximation would break down, and so Monte Carlo modeling was used.

FD systems, as described in this dissertation, use a sinusoidally intensity-modulated source and heterodyne detection capable of measuring the decrease in modulation depth (or amplitude attenuation) and phase shift of the propagated photon density wave, which is a progressively decaying wave of intensity [19]. The phase lag and amplitude attenuation are functions of μ_a and μ_s' and depend upon the source-detector separation distance and modulation frequency of the source [20]. The measurements can involve either different modulation frequencies at one source-detector separation or multiple source-detector separations for one modulation frequency [21]. In the studies described herein, two steady-state diffuse reflectance instruments and one frequency-domain system were used; therefore they will all be described.

Steady-state systems: The SkinSkan spectrofluorometer (JY Horiba, Edison, NY) source components includes a 125 W continuous output xenon (Xe) lamp with output from 240-1000 nm and an excitation monochromator. A UV-enhanced silicon photodiode serves as the reference detector which monitors and corrects for time- and wavelength-dependent lamp and power supply variations. The emission monochromator collects light in synchrony with excitation, and the light is then delivered to an extended red (200-850 nm) photomultiplier tube (PMT), which converts the light signal into an electronic signal to be read by the

computer. The other instrument (JY Horiba, Edison, NY) is comprised of a 450 W Xe arc lamp and excitation monochromator as the source, with an imaging spectrograph and charge-coupled device (CCD) to convert light to electronic charge on the detector end. The PMT is a single channel detector, which collects reflectance on a wavelength-to-wavelength basis, whereas the CCD is a multi-channel photodetector that can collect wavelength and position information simultaneously. The monochromator on the second instrument is not necessary, since we just use white light, but even with the monochromator the intensity of light is sufficient for the described applications.

Frequency-domain system: The FD system [22] incorporates intensity-modulated (50-250 MHz continuously) light sources. The light sources are six laser diodes: 654, 683, 779, 805, 847, and 905 nm (JDS Uniphase, Milpitas, CA). An RF switch (8769K and 11713A, Agilent Technology, Palo Alto, CA) is used to select the laser diode for modulation, and this is coupled to an 8x8 optical switch (GP700, DiCon Fiberoptics, Inc., Richmond, CA). The optical switch functions to deliver the light from each of the six laser diodes first through the short then through the long separation fiber of the probe. The collection end of the probe is coupled to an avalanche photodiode (APD) module (C5658, Hamamatsu Corp., Japan). The μ_a and μ_s' are obtained through a nonlinear least square fitting based on the measured amplitude and phase.

The steady-state and frequency-domain instruments described here have their share of advantages and disadvantages. The CCD-based instrument is superior to the other two instruments in terms of speed of spectral acquisition. One spectra can be obtained in under a second, whereas for the PMT-based and FD instruments, the acquisition time is closer to one minute. The CCD allows for collection of all wavelength points simultaneously, whereas the PMT-based instrument has a scanning configuration, and the FD instrument uses an optical switch to rotate through different laser diodes and probe separations. On the other hand, when just comparing the steady-state instruments, we have found the PMT-based instrument to be more accurate in terms of optical property extractions, possibly due to the difficulties

encountered in maintaining signals within the linear range of the CCD-based instrument [23]. For the frequency-domain instrument, because the phase shift and amplitude attenuation measurements are not intensity-dependent, there is no requirement to correct for day-to-day variations in instrument source intensities. This is an asset, because calibration procedures can be complicated by adherence to guidelines for repeatable reflectance standard measurements over time. Finally, the steady-state and frequency-domain instruments are designed to measure different wavelength ranges. The two steady-state instruments are designed for measurements in the UV-VIS wavelength range, so that fluorescence of common tissue fluorophores can also be obtained. On the other hand, the frequency-domain instrument measures in the far-red and NIR. Based on these specifications, the selection of instrument is dependent upon the target measurement of interest, where UV-VIS wavelengths are relevant for mucosal surface and NIR wavelengths are applicable for thicker tissues with overlying skin.

1.5 Assessment of the Robustness of the Inverse Monte Carlo Algorithm

Monte Carlo is based on the theory that photons undergo a random walk in tissue, and the step size and direction of scattering can be determined by stochastic sampling of probability distributions [24]. The forward Monte Carlo model refers to the calculation of diffuse reflectance for a given μ_a , scattering coefficient, μ_s , and anisotropy coefficient, g , which describes the amount of forward scattering retained after a photon encounters scattering event. The reduced scattering coefficient describes isotropic scattering and is related to μ_s and g by $\mu_s' = \mu_s(1-g)$. The equation governing the step size, x , is given by:

$$x = \frac{-\ln \xi}{\mu_a + \mu_s} \quad (3)$$

ξ is a pseudorandom number between 0 and 1. This equation is derived from Beer's Law.

Determination of the scattering angle, θ , is derived from the Henyey-Greenstein phase function [25], and is represented by:

$$\theta = \arccos \left\{ \frac{1}{2g} \left[1 + g^2 - \left(\frac{1 - g^2}{1 - g - 2g\xi} \right)^2 \right] \right\} \quad (4)$$

By assuming azimuthal symmetry, the equation for the azimuthal angle, φ , is governed by:

$$\varphi = 2\pi\xi \quad (5)$$

However, the true problem in our application of tissue optics is to determine the μ_a and μ_s' from a measured reflectance spectrum. For this problem, the inverse Monte Carlo model must be used [18].

The inverse Monte Carlo model developed in our lab is based on an approach that uses scaling relationships that help speed up the simulations [26]. Only a single baseline simulation is required to form a lookup table (i.e. look up reflectance for a given set of optical properties) that greatly reduces the computational time of the calculations. The inverse Monte Carlo model has been described extensively [18, 27], so only a brief synopsis is included here.

One of the main components of the inverse Monte Carlo model is a reference phantom, which is required to put the forward modeled reflectance on the same scale as the measured reflectance [18]. The modeled signal is on an absolute scale, while the measured signal includes an instrument and lamp response. Phantoms, as described within this thesis, are liquid standards with known optical properties that can be used to test the quantitative accuracy of different methods. The reference phantom, which has known μ_a and μ_s' , is measured using the same instrument and probe as the target phantom or tissue, and so a scaling factor derived from the reference measurement can be applied to the target measurement to scale it for comparison to the forward modeled reflectance. Once a scaling factor is determined between the measured and modeled reflectance, this can be applied to a new measurement (inverse model). First an initial guess for the target μ_a and μ_s' is made, which can then be used to determine the reflectance from the forward model. The scaling factor from the reference phantom is applied to the modeled reflectance, thus giving the predicted reflectance. The sum of squares error (SSE) between the new measurement and the predicted reflectance is

calculated, and the entire process is repeated until the SSE is minimized. The μ_a and μ_s' corresponding to the minimal SSE obtained from this iterative process are the “extracted optical properties.”

Validation of the inverse Monte Carlo model was detailed in papers by Palmer and Ramanujam [18, 28], and an assessment of the robustness of the algorithm was provided by Bender, et al. [23]. The robustness study identified a set of master reference phantoms for future clinical studies as well as tested the robustness of the model in quantifying large ranges of hemoglobin concentration and saturation, quantifying concentrations of multiple absorbers in a dual-absorber phantom set, and assessed the effect of different probe and instrument configurations on extracted optical properties.

1.6 Noninvasive Measurements of Hemoglobin Concentration and Saturation

The measurement of hemoglobin concentration becomes complicated *in vivo* because the blood is contained in capillaries under the tissue surface. In mucosal surfaces, such as the sublingual tissue (floor of the mouth), the blood-filled capillaries are found under a nonkeratinized epithelium, which is $190 \pm 40 \mu\text{m}$ thick [29]. Along with the capillaries, fibroblasts, connective tissue, and extracellular matrix are also found in this lamina propria layer [30]. For skin-covered surfaces, such as the palm of the hand, the blood-filled vessels are underneath an epidermal layer that is $1.7 \pm 0.4 \text{ mm}$ thick [31]. Because of the great variability in the location of blood-filled vessels depending on the location in the body, noninvasive methods for hemoglobin concentration determination must be adaptable to probing different depths of tissue. In addition, the disentanglement between absorption of blood and scattering of structures, such as collagen fibrils, is a main problem for understanding blood *in vivo*.

It is of clinical interest to have a monitor that can measure hemoglobin concentration and saturation from tissue noninvasively. Research has been conducted in this field with optical, ultrasonic, and optoacoustic methods [32]. The technique that is closest to becoming

standard of care for noninvasive hemoglobin measurements is pulse oximetry. Pulse oximetry is based on similar principles as CO-oximetry, but rather than requiring a blood sample, a monitor is placed directly on a tissue surface where light transmission is possible, typically the fingertip. The wavelengths and design of pulse oximeters are proprietary, but in general they consist of light sources (red to near-infrared (NIR) wavelengths) and a photodetector. The pulse oximeter can distinguish between the variable absorption of the pulsatile arterial blood and the absorption from the static arterial and venous blood and tissue itself [33]. Because the pulse oximeter relies on this pulsatile nature of blood flow, it cannot be used in cases where the blood flow is continuous, such as during cardiac bypass surgery [34]. Additionally, pulse oximeters are pre-calibrated and so may suffer from inaccuracies at extremes of hemoglobin saturation and concentration. Despite these limitations, there have been significant advances in the field of pulse oximetry, particularly in the addition of wavelengths to allow measurements of more blood components. The Masimo Corporation's SpHb™ monitor has recently been initiated for full market release (2009). The system has been validated in 19 surgical patients and 9 volunteers undergoing hemodilution yielding hemoglobin concentrations ranging from 4.4-15.8 g/dl with a correlation coefficient of $r=0.898$ when compared to arterial hemoglobin concentration [35], and feasibility for monitoring hemoglobin concentrations between 5.8-10.3 g/dl has been carried out in a single liver transplant case, with a reported precision of 0.74 g/dl [36].

Optoacoustic and ultrasound methods have been tested for non-invasive hemoglobin measurements from the radial and brachial arteries, respectively. The studies using optoacoustic measurements required further development of sophisticated algorithms for accurate *in vivo* measurements of hemoglobin plus assessments of the effects of skin pigmentation on the accuracy [37]. Humans have variable amounts of melanin in their skin, and because melanin is a strong absorber in the UV-VIS-NIR wavelength ranges, skin pigmentation can be an unwanted source of contrast in optical measurements on surfaces with overlying

skin. Ultrasonic measurements have been shown to correlate with arterial hematocrit ranging from 32.0-49.3% with absolute mean error of 3.24% and standard deviation of 3.27%, but like pulse oximetry, ultrasound only measures arterial components of tissue [38].

Optical polarization imaging studies of vessel segment density from the sublingual mucosa have been shown to measure hemoglobin with a correlation coefficient of $r=0.93$ for predicted versus reference hemoglobin measured from venipuncture from the forearm. However, these measurements have no direct analog in existing laboratory measures, and so the clinical viability of this technique is still unclear [39]. UV-VIS and NIR diffuse reflectance spectroscopy have also been investigated to measure hemoglobin concentration [40-44].

UV-VIS Diffuse Reflectance: In the UV-VIS wavelength regime, the absorption of hemoglobin is high, and so a biological site with vasculature close to the surface would be most appropriate. Because the thickness of the skin can be on the order of several millimeters, a biological site without skin would be a suitable target. Non-skin sites include mucosal surfaces, such as the inside of the mouth or the lining of the esophagus. Several studies have investigated UV-VIS spectroscopy to assess hemoglobin status of the tissue. The Spectros T-Stat® is an FDA-approved VIS light spectroscopy device sensitive to ischemia, but to the best of our knowledge only saturation has been validated *in vivo* [40]. Another study using a research spectroscopy system tested two different algorithms (partial least-squares and discrete region modeling) on diffuse reflectance measurements at VIS wavelengths from the mucosal inner lining of the eyelid in patients with hemoglobin ranging from 7.3-16.7 g/dl [43]. Depending on the algorithm used, the authors achieved sensitivity of 86% and 57% and specificity of 91% and 100%, indicating the importance of exploring these models further.

NIR Diffuse Reflectance: Because the absorbance of hemoglobin and water is low in the NIR, tissue is relatively transparent in this wavelength regime [45]. In other words, the light will penetrate deeper, and a skin-covered site could be an appropriate target. Several studies in the literature have used NIR methods to measure hemoglobin content in the tissue, either

due to some biological trigger (such as anemia) or induced hemorrhage. One study using VIS-NIR temperature-controlled photometer measurements from the forearm identified one anemic blood donor out of 19, but the estimates of hemoglobin were affected by the skin pigmentation of the calibration population [41]. In a different study utilizing NIR reflectance measurements from the forearm of cardiac bypass patients with hematocrit ranging from 14.3-44.2%, a correlation coefficient of $r=0.71$ was achieved when compared to arterial hemoglobin, but the predictive ability of the algorithm was again affected by skin pigmentation [42]. In another study using a diffuse optical spectroscopy (DOS) system (frequency domain photon migration (FDPM) combined with steady-state NIR spectrometry), lower body negative pressure (LBNP) was induced in healthy volunteers to simulate hemorrhage [44]. In that study, the authors saw decreases in total hemoglobin and hemoglobin saturation with increases in LBNP ($p < 0.001$).

The studies discussed here were limited by providing measurements limited to specific body sites [35, 36, 38, 39, 44], utilizing complicated algorithms [37, 38, 40, 43], or suffering from inter-patient variability [41, 42], and so the opportunity exists to explore new approaches that can address all of these issues.

1.7 Probe-Tissue Interfacing

A handful studies have tested the effect of probe pressure on measured diffuse reflectance and extracted optical properties. One study on *ex vivo* human and animal tissue samples showed there to be a decrease in reflectance and a subsequent increase in the μ_a and μ_s' with increasing probe pressure [46]. Another study investigating the effect of probe pressure when applied to mouse thigh muscle saw a decrease in reflectance, oxygen saturation, blood vessel radius, and Mie slope along with an increase in μ_s' at 700 nm with increased pressure [47]. Another study looking at the effect of pressure when applied to the rat heart and liver found that when pressure was applied the hemoglobin became less oxygenated and overall absorption was reduced [48]. The pressure threshold required to induce these changes in the reflectance spectra was found to be tissue-type dependent. A different study saw changes in

the diffuse reflectance shape when skin spectra were obtained with varying pressures [49]. These authors included preliminary simulations to try to elucidate the effect of increased probe pressure, namely an increase in scatterers at the measurement site and a decrease in blood volume fraction and oxygenation.

Furthermore, one group found the effects of pressure using a handheld DOS probe on breast tissue to be minimized based on their tissue-probe interfacing [50]. They attribute the variations of only 6-7% to the low overall force distributed over a large probe surface area and the combination of frequency-domain (FD) and broadband steady-state being insensitive to absolute optical power. Thus, it is important to realize the probe design can have a major effect on the ability to control the pressure applied to a biological area. In addition, because the maximum depth that NIR wavelengths can probe is deeper than UV-VIS wavelengths [45], the amount of contrast due to pressure may be less of an effect in the NIR. In other words, the portions of the tissue that the NIR wavelengths interrogate are further from the site of pressure.

There are several advantages and disadvantages for measuring either mucosal sites, such as the sublingual tissue, or skin-covered sites, such as the thenar eminence (the muscle on the palm of the hand by the thumb). These are summarized in Table 1.

Table 1: Advantages and disadvantages for diffuse reflectance measurements from the sublingual tissue and thenar eminence. Mucosal sites which lack a thick epidermal layer are better suited to the UV-VIS wavelengths, where the absorption of hemoglobin is high and so light cannot travel as deep in the tissue. Skin sites are more suited to NIR wavelengths, where the absorption of hemoglobin is lower, and so the tissue is relatively transparent to light. Coupled with a probe with a sufficient source-detector separation, this enables light to reach the deeper blood-filled components of the tissue.

| | MUCOSA (sublingual tissue) | SKIN (thenar eminence) |
|----------------------|---|---|
| Advantages | <ul style="list-style-type: none"> • Not covered by skin (can use UV-VIS and any fiber geometry) • Well-perfused • Low melanin content • Small variability in thickness between patients | <ul style="list-style-type: none"> • Lower fat and melanin content than other skin-covered sites • Easy to secure probe • Can visualize tissue-probe interface • Can be placed away from other instruments |
| Disadvantages | <ul style="list-style-type: none"> • Difficult to secure probe • Cannot visualize tissue-probe interface • In way of other devices during surgery • Uncomfortable for patient unless anesthetized | <ul style="list-style-type: none"> • Thick skin-covered surface (need NIR and large fiber separations) • Temperature can fluctuate in area thus affecting collected signals • Some variability in melanin and thickness between patients |

From the table, it is clear that both mucosal and skin-covered surfaces suffer some disadvantages, but depending on the study design, one site may be more appropriate than another. For example, when performing measurements on non-anesthetized patients, it would be difficult to maintain probe placement in the oral cavity, whereas on patients under anesthesia, this would be less of an issue. On the other hand, the temperature of the skin may vary a lot during surgery, and there may be many intravenous devices on the hand, and so a probe placement in the mouth may be better suited for surgical applications.

1.8 UV-VIS Measurements of the Sublingual Mucosa During Surgery

One of the key concerns for anesthesiologists during surgeries is to determine when transfusions are required. Transfusions of biological fluids can be in the form of whole blood or any of its constituents: red blood cells, white blood cells, platelets, and plasma [51]. In addition, blood substitutes, which are used to transport oxygen and expand blood volume, can

be delivered to the patient [52]. These blood substitutes include, but are not limited to, saline, Ringer's lactate, which is isotonic to blood, and Hextend®, which is isotonic to plasma [53].

Hemoglobin concentration is traditionally measured in the surgical setting through the use of a blood draw from a catheter that generally remains in the artery throughout the duration of the surgery. The blood sample is then subjected to CO-oximeter and/or blood gas measurements of hemoglobin concentration, along with other parameters such as pH, pCO₂, and pO₂, as described in “1.3 Invasive Measurements of Hemoglobin Concentration and Saturation.” Normal hemoglobin levels range from 12-16 g/dl in humans, with women tending towards the lower end of normal [10]. Blood transfusions are indicated when hemoglobin drops to 6-10 g/dl, depending upon other patient-specific factors, such as signs of organ ischemia [54]. Blood draw determination of hemoglobin is limited in that it is an invasive procedure, it is costly to the patient, it is time-consuming and requires a wait-time to receive results, it subjects the technician to blood borne pathogens, and if the sample is not directly analyzed, there is the possibility of the measurements not accurately reflecting the biological environment at the time of the draw.

On the other hand, a noninvasive monitor, such as probe-based diffuse reflectance spectroscopy, is capable of making repeat measurements throughout the course of the surgery, can provide rapid results, and causes no harm to the patient. Noninvasive measurements have been used in the medical field for centuries, such as for blood pressure or pulse measurements, and throughout the years, more noninvasive procedures such as computed tomography, magnetic resonance imaging, and ultrasound, to name a few, have become routine in hospitals and clinics. The future of hemoglobin concentration measurements clearly points towards the adoption of a noninvasive device capable of delivering rapid results. Because of the versatility of light penetration depth (by tailoring the wavelength and probe design) for probe-based diffuse reflectance spectroscopy, this technique is well-suited to measure hemoglobin concentration from many different biological sites in humans. The study described by Bender,

et al. implemented UV-VIS diffuse reflectance spectroscopy with a probe suitable for measurements in the sublingual tissue of the mouth, in patients undergoing surgeries [55].

1.9 NIR Measurements of the Thenar Eminence During Induced Hypovolemia

Measurements in the NIR wavelength range coupled with a probe with sufficient source-detector separations allow for interrogation of skin-covered areas, as the hemoglobin absorption is lower and so NIR wavelengths travel deeper into the tissue than UV-VIS wavelengths. Measuring from skin sites enables enhanced probe-tissue stability compared to measurements in mucosal sites. Through the use of a side-firing optical probe which can easily be taped directly to the skin, these measurements can be assumed to be more robust as they will help mitigate the effects of probe pressure and movement.

Several studies in the literature have used NIR diffuse reflectance to look at regional variations in tissue optical properties during hypovolemia and resuscitation. One group has investigated diffuse optical spectroscopy (DOS) as a method to assess the efficacy of resuscitation via *in vivo* measurements on the hind thigh of rabbits [56]. In this study, an increase in DOS-measured hemoglobin was observed during resuscitation with artificial blood products, while the serum-measured hemoglobin did not increase. In a different study, probe-based NIR spectroscopy measurements from the thenar eminence revealed the hemoglobin saturation to be an indicator of shock in a human study including normal subjects and patients undergoing resuscitation due to shock [57]. Another study investigated the use of NIR spectroscopy to measure blood loss in humans, based on the changes in the hemoglobin oxygenation measured from the cerebral cortex and calf muscle [58]. In that study they saw tissue oxygenation drop as a function of blood loss.

In “5. *In Vivo* Diffuse Reflectance Measurements from the Thenar Eminence in Volunteers Undergoing Hypovolemia,” a study is discussed that used NIR diffuse reflectance

spectroscopy with a side-firing probe suitable for measurements from the thenar eminence, in patients undergoing induced hypovolemia.

1.10 Ratiometric Method to Estimate Hemoglobin

Ratiometric methods are of interest in settings where rapid results are desired, as they generally involve simple calculations, such as the division of the reflectance at one wavelength point to another point. The ratios may be determined empirically, but the selection of wavelength points can be guided by the biological feature they are intended to measure. For diffuse reflectance and/or fluorescence measurements of most human tissue, the primary absorber is hemoglobin. Because hemoglobin can be either oxygenated or deoxygenated, there are two tasks: (1) measure the total hemoglobin (oxyhemoglobin + deoxyhemoglobin) and (2) measure the hemoglobin saturation (oxyhemoglobin/total hemoglobin). The molar extinction coefficients of oxy- and deoxyhemoglobin overlap at eight wavelengths (isosbestic points) in the UV-VIS wavelength range: 390, 422, 452, 500, 529, 545, 570, and 584 nm (Figure 2) [59].

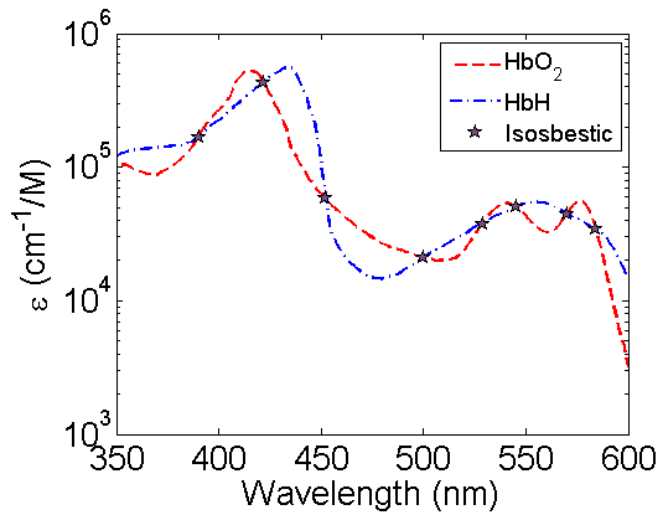


Figure 2: Extinction coefficients for oxy- and deoxyhemoglobin (HbO₂ and HbH, respectively) from 350-600 nm [59]. The stars indicate the isosbestic points where the extinction coefficients for HbO₂ and HbH are equal.

When the extinction coefficients of the two hemoglobin species are equal, measurements taken at those points are independent of hemoglobin saturation. On the other

hand, measurements taken where there are maximal differences between the two species will provide information about hemoglobin saturation [15]. Studies from the literature have used ratios involving both isosbestic and non-isosbestic points as a metric to grade malignancy or disease [60-64], to estimate vessel depth [65-67], and quantify hemoglobin saturation [68, 69] and hemoglobin concentration [70].

Grading malignancy or pathology: One study utilized a reflectance ratio, 615/460 nm, measured from diffuse spectral imaging to quantify and map erythema spatial distribution *in vivo* in the human gingiva [60]. Another study found the spectral reflectance ratio of 580/680 nm to be an indicator of grade of cartilage degeneration from *ex vivo* spectrophotometric measurements of human articular cartilage [61]. An additional study found a reflectance and fluorescence ratiometric classifier capable of disease classification in an *ex vivo* pancreatic tissue study [62]. Another group found that both a fluorescence ratio (500/685 nm) and reflectance ratio (545/575 nm), each using one isosbestic point, could be used to grade degrees of malignancy in an *ex vivo* oral cancer study [63, 64].

Estimating vessel depth: The average depth of blood regions in the skin has been estimated using isosbestic points at 420 and 585 nm [65, 66]. The addition of a third isosbestic wavelength (800 nm) has been shown in Monte Carlo simulations, as well as agar gel phantoms and human veins, to estimate both vessel depth and thickness [67].

Hemoglobin saturation and concentration: Several studies in the literature have capitalized on isosbestic points to measure hemoglobin saturation, by using a ratio consisting of one isosbestic point and one where there are maximal differences between oxy- and deoxyhemoglobin [63, 64, 68]. In one study, a microdensitometer was used to measure oxygen saturation in capillaries of the hamster cheek pouch, through the use of a ratio including the 420 nm isosbestic point and 431 nm non-isosbestic point [68]. Other studies have used ratios involving two or more isosbestic wavelengths of hemoglobin. One study used 520 and 546 nm to determine the contribution of scattering to optical density measurements of whole blood [69]. The scattering term could then be used to calculate hemoglobin absorption at the two

isosbestic points plus a third wavelength where the oxy- and deoxyhemoglobin extinction coefficients were different. This, in turn could then be used to calculate hemoglobin saturation. Another study using fluorescence emission measurements from phantoms comprised of flavin adenine dinucleotide, hemoglobin, and polystyrene spheres, found the ratio of fluorescence intensity at two isosbestic points, 500 and 570 nm, could be used to measure total hemoglobin concentration. This ratio was independent of scattering and hemoglobin saturation [70]. Furthermore, the authors determined that the ratio calculated as the product of 540/560 and 578/560 nm was related to hemoglobin saturation.

It is evident from the studies in the literature that simple, rapidly calculated reflectance ratios can give details about the biological processes that light can probe. The selection of wavelengths depends on the optical parameter of interest. Phelps, et al. have developed a method to estimate hemoglobin concentration, independent of saturation and scattering using several different isosbestic points, and this method has thus far been shown to be instrument-independent and shows promise in estimating hemoglobin concentration from clinical measurements of the human cervix [9]. Table 2 compares the advantages and disadvantages of this ratiometric isosbestic method over traditional pulse oximetry.

Table 2: Comparisons of the advantages and disadvantages associated with the isosbestic ratiometric method and pulse oximetry. The ratiometric isosbestic method and some newer implementations of pulse oximetry can both provide rapid measurements of hemoglobin concentration. The major advantages of the ratiometric method are that it can be used even when the blood flow is not pulsatile and it provides hemoglobin measurements independent of saturation and scattering.

| | RATIOMETRIC METHOD | PULSE OXIMETRY |
|----------------------|---|---|
| Advantages | <ul style="list-style-type: none"> • Can be used when blood flow is not pulsatile (i.e. cardiac bypass) • Calibrated using simulated data with known optical properties • Independent of saturation and scattering • Flexibility in probe and instrument design | <ul style="list-style-type: none"> • Can measure pulse • Flexibility in wavelengths used • Can achieve range of penetration depth with NIR wavelengths • Can measure more blood components by using more wavelengths |
| Disadvantages | <ul style="list-style-type: none"> • Cannot measure pulse • Penetration depth limited by wavelengths where there are isosbestic points of oxy- and deoxyhemoglobin • Can only measure hemoglobin | <ul style="list-style-type: none"> • Pulsatile blood flow required • Typically pre-calibrated to normal population so can have inaccuracies at low saturations • Less flexibility in design • Not all monitors can measure concentrations |

1.11 Major Outcomes

The major outcomes of my dissertation are as follows:

1. I have identified a set of master reference phantoms which can be used to ensure more accurate extraction of optical properties from laboratory and clinical measurements and evaluated the robustness of the inverse Monte Carlo model using UV-VIS wavelengths and a steady-state instrument (2. Assessment of the Robustness of the Inverse Monte Carlo Model).
2. I have conducted a clinical study measuring sublingual UV-VIS diffuse reflectance in patients undergoing general surgery and correlated the optical measurements to invasive hemoglobin concentration values. Both the inverse Monte Carlo model and a preliminary isosbestic ratiometric method were evaluated for this study (3. *In Vivo* Diffuse Reflectance Measurements from the Sublingual Mucosa in Patients Undergoing Surgery).

3. I have used simulations and laboratory measurements to assess the quantitative accuracy of hemoglobin concentration estimation using NIR wavelengths and a steady-state instrument with Monte Carlo. While the simulations implied the Monte Carlo model should be feasible in the NIR, the laboratory results indicated a reduced ability to quantify hemoglobin in the NIR thus pointing towards the use of a frequency-domain system and diffusion approximation (4. NIR Measurements Using an Inverse Monte Carlo Model and a Steady-State System).
4. I have implemented a clinical study measuring NIR diffuse reflectance in volunteers undergoing induced hypovolemia. The extracted hemoglobin concentration and saturation were compared to arterial hemoglobin as well as optical properties determined from other noninvasive optical monitors (5. *In Vivo* Diffuse Reflectance Measurements from the Thenar Eminence in Volunteers Undergoing Hypovolemia).
5. I have developed a ratiometric method to rapidly determine hemoglobin concentration, independent of scattering and hemoglobin saturation. This method utilizes linear regression equations generated from simulations that can be applied directly to laboratory or clinical measurements (3. *In Vivo* Diffuse Reflectance Measurements from the Sublingual Mucosa in Patients Undergoing Surgery and 6. Development of a Ratiometric Method to Estimate Hemoglobin Concentration).
6. I have evaluated the sensitivity of Neutron Stimulated Emission Computed Tomography (NSECT) for detection of breast cancer using Monte Carlo simulations (Appendix A).

2. Assessment of the Robustness of the Inverse Monte Carlo Model

2.1 Introduction

One of the biggest challenges for diffuse reflectance spectroscopy is the ability to accurately quantify absorption and scattering from the medium being interrogated. Because the optical properties of tissue are not “known,” the best solution is to rigorously test tissue-mimicking phantoms with known optical properties and use those results to guide the methodology for tissue measurements. The inverse Monte Carlo model [18] requires a reference phantom, the selection of which can have a large impact on the extracted optical properties. The purpose of this chapter was to test a series of tissue-mimicking phantoms that could be used to guide the choice of reference phantoms for clinical studies. In addition to finding the best references, the robustness of the algorithm in measuring large ranges of hemoglobin saturation and concentration was tested, as well as the effect of different instruments and probes on the extracted μ_a and μ_s' . Furthermore, the ability of the algorithm to extract information about two absorbers in a multi-absorber phantom was tested. All of the factors that were tested were designed to mock the clinical problem as closely as possible. A majority of this chapter is drawn from [23].

2.2 Methods

2.2.1 Phantom Preparation and Calculations

Phantoms consisted of a combination of absorber(s), scatterer, and solvent. The solvent was research-grade water, unless otherwise noted. Phantoms are constructed with known optical properties, and so the extraction ability of said optical properties can be evaluated. The scatterer used for all phantom studies was 1 μm diameter monodisperse polystyrene spheres (07310, Polysciences, Inc., Warrington, PA), and the absorbers were powdered forms of human hemoglobin A₀ (H0267 ferrous stabilized, Sigma Co., St. Louis, MO)

and/or crocin (17304 standard Fluka, Fluka, Allentown, PA). The hemoglobin could be assumed to be 100% oxygenated, unless a reducing agent was added to the solution. Crocin has a similar absorption spectrum to beta carotene, an absorber which is found in breast tissue and has been shown to differentiate benign and malignant tissues [71]. Phantoms generally consist of additions of either absorber or scatterer to one or more initial scattering or absorbing levels, respectively. The addition of either component causes a dilutional effect on whichever component is not being added, and this can be accounted for as the added volumes are controlled.

To set up for a phantom experiment, the desired μ_a and μ_s' for each phantom in a set ($\mu_{a,phan}$ and $\mu_{s',phan}$) is first established. Stock solutions of absorber and scatterer that form the phantoms are then created. For the absorber, a concentrated stock solution is created, then the absorption spectrum of the stock ($\mu_{a,stock}$) determined by measuring a diluted stock sample. For the scatterer, the μ_s' for the stock ($\mu_{s',stock}$) was determined from Mie Theory using freely available software, given the size, density, and refractive index of the polystyrene spheres, as well as the refractive index of the surrounding medium [72].

Calculations for a phantom set involving addition of absorber are described here, where the volume of each addition of absorber must be predetermined. To calculate for addition of scatterer, similar steps are taken, but μ_a is fixed. When the phantoms consisted of additions of absorber, $\mu_{s',phan}$ was defined only for the initial scattering level, then the subsequent values of μ_s' were calculated based on the dilutional effect of adding absorber to the phantom. Likewise, if scatterer was added, the subsequent μ_a values were calculated based on the dilutional effect of adding scatterer.

First the initial volume for the first phantom, V_{start} , was set (typically 8 mL). The absorber and scatterer volumes for the first phantom (V_{a1} and V_s) were then calculated by:

$$\begin{aligned}
V_{a1} &= V_{start} \frac{\mu_{a,phan1}}{\mu_{a,stock}} \\
V_s &= V_{start} \frac{\mu_{s,phan}}{\mu_{s,stock}}
\end{aligned}
\tag{6}$$

The water volume, V_{water} , was simply calculated by subtracting V_{a1} and V_s from V_{start} . Next, the total volume of absorber for the next phantom was calculated by:

$$V_{a2} = \frac{V_s + V_w}{\frac{\mu_{a,stock}}{\mu_{a,phan2}} - 1}
\tag{7}$$

The actual volume of absorber to add could then be calculated by $V_{a2} - V_{a1}$. The new total volume was then calculated in the same manner. The dilution effect on μ_s' was calculated as the original volume divided by the new total volume (V_{total}). The subsequent additions of absorber were then calculated in a similar manner. The concentration of absorber was calculated as shown for phantom 2 by:

$$[absorber] = \frac{mg_{stock} \cdot \frac{V_{a2}}{mL_{stock} \cdot V_{total}}}{MW}
\tag{8}$$

The MW is the molecular weight of the absorber in g/mol, and mg_{stock} and mL_{stock} refer to the mass of powdered absorber dissolved in a given volume to create the stock. For the hemoglobin used in these experiments, the concentration had to also be multiplied by 0.5, because the product was approximately 50% protein. For phantom experiments where the concentration of absorber was set, rather than the μ_a , the same equations for could be rearranged to calculate the absorber volumes.

2.2.2 Phantom Variations

Several sets of phantoms were used to test different facets of the inverse Monte Carlo model in this study. Single absorber phantoms were used to assess the effect of different instruments and probes on extracted optical properties and to identify a set of master

reference phantoms that yielded low errors for both extracted μ_a and μ_s' . Double absorber phantoms were used to test the ability to extract concentrations of both hemoglobin and crocin when they were combined in phantoms. Hemoglobin concentration phantoms were tested to determine the robustness of the algorithm in extracting expanded ranges of concentration. Hemoglobin saturation phantoms were used to test the ability to extract saturation when the hemoglobin concentration was held constant.

2.2.2.1 Single absorber phantoms

Hemoglobin or crocin were used independently in single absorber phantoms. There were two sets of hemoglobin phantoms, one of which consisted of five hemoglobin additions to two initial scattering levels (SA_Hb_a) while the other consisted of five scatterer additions to two initial absorber levels (SA_Hb_b). Table 3 shows the absorption and scattering levels for the SA_Hb phantoms. The range and mean for the optical properties is given over the wavelength range 350-600 nm.

Table 3: Absorber (A1-A5) and scatterer (S1-S5) levels used in single absorber (hemoglobin) phantoms (SA_Hb_a and SA_Hb_b). SA_Hb_a phantoms consisted of two scatterer levels (S2 and S4), which were subjected to five additions of hemoglobin, yielding absorption levels A1-A5. On the other hand, the SA_Hb_b phantoms included two absorber levels (A2 and S4), which were subjected to five additions of polystyrene spheres yielding scattering levels S1-S5. The addition of absorber caused a slight dilution in scattering for SA_Hb_a, while the addition of scatterer caused a dilution in absorption for SA_Hb_b, all of which was accounted for in the inverse Monte Carlo model. There were 10 total phantoms for both SA_Hb_a and SA_Hb_b.

| Absorber levels | | | | Scatterer levels | | |
|-----------------|-----------------------------------|----------------------------------|---------------|------------------|------------------------------------|-----------------------------------|
| | μ_a range (cm ⁻¹) | Mean μ_a (cm ⁻¹) | Hb (μ M) | | μ_s' range (cm ⁻¹) | Mean μ_s' (cm ⁻¹) |
| A1 | 0.01 - 0.8 | 0.2 | 0.7 | S1 | 7.5 - 11.0 | 9.9 |
| A2 | 0.08 - 7.1 | 1.5 | 6.4 | S2 | 11.2 - 16.5 | 14.9 |
| A3 | 0.11 - 10.4 | 2.2 | 9.2 | S3 | 14.9 - 22.1 | 19.9 |
| A4 | 0.14 - 12.8 | 2.7 | 11.4 | S4 | 18.6 - 27.6 | 24.8 |
| A5 | 0.17 - 15.9 | 3.3 | 14.2 | S5 | 22.4 - 33.1 | 29.7 |

Crocin phantoms (SA_Cr) consisted of four crocin additions for three initial scattering levels (S2-S4), as shown in Table 4. The absorption levels for crocin were selected to be fractions of the A2 absorber level shown in Table 3.

Table 4: Absorber levels used in single absorber (crocin) phantoms (SA_Cr). Crocin was added in four increments to three scattering levels (S2-S4). The μ_a was set to be a fraction of the A2 level in the SA_Hb_a and SA_Hb_b phantoms. The addition of crocin caused a dilution in scattering, which was accounted for in the inverse Monte Carlo model. There were 12 total phantoms for SA_Cr.

| Absorber levels | | | |
|-----------------------------------|----------------------------------|----------------|---------------|
| μ_a range (cm ⁻¹) | Mean μ_a (cm ⁻¹) | Fraction of A2 | Cr (μ M) |
| 0.002 - 2.2 | 0.8 | 0.5 | 123.1 |
| 0.003 - 3.3 | 1.2 | 0.75 | 184.5 |
| 0.004 - 4.4 | 1.6 | 1 | 246.8 |
| 0.005 - 5.5 | 2 | 1.25 | 308.5 |

2.2.2.2 Double absorber phantoms

Hemoglobin and crocin were used as absorbers in a double-absorber phantom set (DA_HbCr). For this phantom set, there were 20 total phantoms, with four combinations of initial hemoglobin and scattering levels. For each of the four levels, the initial phantom contained only hemoglobin as the absorber, and then each of the four subsequent phantoms had additions of crocin (Table 5). The initial hemoglobin levels were A2 and A4, and scattering levels S2 and S4 were tested for each of those two levels. As with the SA_Cr phantom set, the crocin levels were fractions of the initial hemoglobin level. Additions of crocin caused a dilutional effect to scattering and hemoglobin.

Table 5: Absorber levels used in double absorber (hemoglobin and crocin) phantoms (DA_HbCr). These phantoms were composed by incrementally adding crocin to four hemoglobin and polystyrene sphere phantoms, with initial absorber-scatterer levels of A2-S2, A2-S4, A4-S2, and A4-S4. The first phantom had only hemoglobin as the absorber, and then four additions of crocin were made. Dilutional effects of added crocin were accounted for in the inverse Monte Carlo model for both the hemoglobin μ_a and μ_s '.

| Hb level A2 | | | | Hb level A4 | | | |
|-----------------------------------|----------------------------------|-----|-----|-----------------------------------|----------------------------------|-----|-----|
| μ_a range (cm ⁻¹) | Mean μ_a (cm ⁻¹) | | | μ_a range (cm ⁻¹) | Mean μ_a (cm ⁻¹) | | |
| | Total | Hb | Cr | | Total | Hb | Cr |
| 0.08 - 7.8 | 1.6 | 1.6 | 0 | 0.14 - 13.9 | 2.9 | 2.9 | 0 |
| 0.07- 9.2 | 2.4 | 1.6 | 0.8 | 0.14 - 16.2 | 4.1 | 2.8 | 1.3 |
| 0.07 - 10.0 | 2.7 | 1.6 | 1.1 | 0.14 - 17.4 | 4.7 | 2.8 | 1.9 |
| 0.08 - 10.7 | 3.1 | 1.6 | 1.5 | 0.14 - 18.6 | 5.4 | 2.8 | 2.6 |
| 0.08 - 11.4 | 3.5 | 1.6 | 1.9 | 0.14 - 19.7 | 6.0 | 2.8 | 3.2 |

2.2.2.3 Hemoglobin saturation phantoms

Hemoglobin saturation phantoms (Sat_Hb) as described in [73] were constructed by the addition of Baker's yeast to a phantom with absorber-scattering level A5-S2 (Table 3). The yeast caused a gradual deoxygenation of the hemoglobin, which was measured as percent oxygen with an oxygen-sensitive electrode (MI-730, Microelectrodes, Inc., Bedford, NH). The A5-S2 phantom was the fifth phantom in a subset of phantoms with the same construction as SA_Hb_a. The phantoms which did not undergo desaturation were used as references for the desaturation phantom. The solvent for these phantoms was 10x PBS to maintain a constant pH of 6.94. The room temperature was held constant at 24 °C, and the phantom was continuously stirred using a magnetic stir bar. Percent oxygen and optical measurements were taken approximately every minute for one hour.

The oxygen-sensitive electrode was calibrated for 100% and 0% in an air-saturated water sample and a water sample completely deoxygenated by the addition of sodium dithionite ($\text{Na}_2\text{S}_2\text{O}_4$), respectively. A subroutine reported by Kelman [12] was used to calculate the expected hemoglobin saturation using the inputs of temperature, pH, partial pressure of carbon dioxide ($p\text{CO}_2$), and partial pressure of oxygen ($p\text{O}_2$). The $p\text{CO}_2$ was derived from percent CO_2 in ambient air, and the $p\text{O}_2$ was calculated assuming a linear relationship with percent oxygen. To test the efficacy of the optical measurements of hemoglobin saturation, comparisons between the Hill's coefficient, n , and the partial pressure of oxygen at which hemoglobin is 50% saturated, p_{50} , were calculated. These coefficients were calculated as described in [74] via fitting to the Hill Equation over the range of 20-80% hemoglobin saturation. The Hill Equation is given by:

$$\text{Hb saturation} = \frac{p\text{O}_2^n}{p\text{O}_2^n + p_{50}^n} \quad (9)$$

2.2.2.4 Hemoglobin concentration phantoms

A set of 17 phantoms with incremental additions of hemoglobin from 1-50 μM (Conc_Hb) were constructed for one initial scattering level, approximately equal to S5 (Table 3). Table 6 shows the absorber and scattering levels for these phantoms. These phantoms were measured using the PMT-based instrument and a similar probe design to Probe A, described below.

Table 6: Absorber and scattering levels used for phantoms spanning a large range of concentrations (Conc_Hb). The initial μ_s' level was set to be S5. The hemoglobin concentrations were set to be spaced in 3 μM increments. The dilution effect of added hemoglobin is mirrored in the reduction of μ_s' from H1 to H17.

| Phantom | Absorption | | Hb (μM) | Scattering | |
|---------|------------------------------|------|----------------------|-------------------------------|------|
| | μ_a (cm^{-1}) | | | μ_s' (cm^{-1}) | |
| | Range | Mean | | Range | Mean |
| H1 | 0.03 - 2.2 | 0.5 | 2.0 | 22.5 - 32.6 | 29.3 |
| H2 | 0.1 - 5.5 | 1.1 | 5.0 | 21.9 - 31.8 | 28.6 |
| H3 | 0.1 - 8.7 | 1.8 | 8.0 | 21.3 - 30.9 | 27.8 |
| H4 | 0.2 - 12.0 | 2.5 | 11.0 | 20.7 - 30.1 | 27.0 |
| H5 | 0.2 - 15.3 | 3.2 | 14.0 | 20.1 - 29.2 | 26.3 |
| H6 | 0.3 - 18.5 | 3.9 | 17.0 | 19.5 - 28.3 | 25.5 |
| H7 | 0.3 - 21.8 | 4.6 | 20.0 | 18.9 - 27.5 | 24.7 |
| H8 | 0.4 - 25.1 | 5.2 | 23.0 | 18.3 - 26.6 | 23.9 |
| H9 | 0.5 - 28.3 | 6.0 | 26.0 | 17.7 - 25.8 | 23.2 |
| H10 | 0.5 - 31.6 | 6.6 | 29.0 | 17.2 - 24.9 | 22.4 |
| H11 | 0.6 - 34.9 | 7.3 | 32.0 | 16.6 - 24.1 | 21.6 |
| H12 | 0.6 - 38.2 | 8.0 | 35.0 | 16.0 - 23.2 | 20.9 |
| H13 | 0.7 - 41.4 | 8.7 | 38.0 | 15.4 - 22.4 | 20.1 |
| H14 | 0.7 - 44.7 | 9.4 | 41.0 | 14.8 - 21.5 | 19.3 |
| H15 | 0.8 - 48.0 | 10.1 | 44.0 | 14.2 - 20.6 | 18.6 |
| H16 | 0.8 - 51.2 | 10.8 | 47.0 | 13.6 - 19.8 | 17.8 |
| H17 | 0.9 - 54.5 | 11.4 | 50.0 | 13.0 - 18.9 | 17.0 |

2.2.3 Optical Measurements

Diffuse reflectance measurements were taken using both the PMT and CCD-based steady-state instruments described in “1.4 Diffuse Reflectance Spectroscopy.” Two different probes were used, both of which were custom-designed then manufactured by RoMack, Inc. (Williamsburg, VA). Probe A had a 19-fiber illumination core surrounded by an 18-fiber collection ring, and Probe B had 29 illumination fibers arranged around 29 collection fibers. For

Probe A, the NA was 0.22 for illumination and collection fibers; for Probe B, the NA of the illumination fibers was 0.125 while for the collection fibers it was 0.12. Both probes had 200 μM illumination and collection fiber diameters. Probe geometry is accounted for in the inverse Monte Carlo model by integration over all illumination-collection fibers [18], as calculated by assessing an image of the common end of the probe using ImageJ [75].

For the CCD-based instrument, two bandpasses were tested: 1.9 nm and 10 nm. The bandpass of the PMT-based instrument was fixed at 5 nm. For both instruments, spectra were collected from 350-600 nm. For the CCD-based instrument with the 1.9 nm bandpass, two scans were required with a 10 nm overlap to cover the whole wavelength range. The two scans were combined by selecting the pixel of closest overlap within the 10 nm region then averaging the remainder of the overlapping points. For the PMT-instrument and the 10 nm bandpass of the CCD-instrument, only one scan was required to cover the whole wavelength range. Both instruments had dark subtract enabled to account for noise from the dark signal. The exposure time of the initial phantom in a set was adjusted to reach a maximum signal-to-noise ratio (at 500 nm) of greater than 100 for both instruments.

2.3 Results

2.3.1 Single Absorber Phantoms

The quantitative accuracy for estimating μ_a and μ_s' was tested using the three single absorber phantom sets measured with the CCD-based instrument with the 1.9 nm bandpass and Probe A. The quantitative accuracy was determined for wavelength-averaged parameters over all reference-target phantom combinations (Table 7). The accuracy is reported as average percent error \pm standard deviation.

Table 7: Average percent errors for single-absorber hemoglobin (SA_Hb_a and SA_Hb_b) and crocin (SA_Cr) phantoms. The errors in μ_s' are lowest for SA_Cr phantoms, possibly because they were composed of more combinations of absorption and scattering levels than the hemoglobin phantoms.

| | SA_Hb_a | SA_Hb_b | SA_Cr |
|----------------------------|-------------|-------------|------------|
| Mean error in μ_a (%) | 9.08 ± 11.9 | 9.68 ± 10.3 | 7.84 ± 7.2 |
| Mean error in μ_s' (%) | 5.30 ± 4.1 | 6.79 ± 7.1 | 1.95 ± 1.5 |

The single absorber phantoms were also used to test which reference levels provided the best accuracy for all target levels. Figure 3 shows the average percent error for all reference-target combinations. Each square is a single reference-target combination, with the references as columns and targets as rows. Each 5x5 sub-grid represents one of the five scattering levels, with each smaller square pertaining to an absorber level. The absorber levels are indicated for scattering level S1 but they are the same for each of the other scattering levels. Blue squares indicate errors <10%, yellow squares indicate errors between 10-20%, and red squares indicate errors >20%. White squares indicate combinations that were not tested.

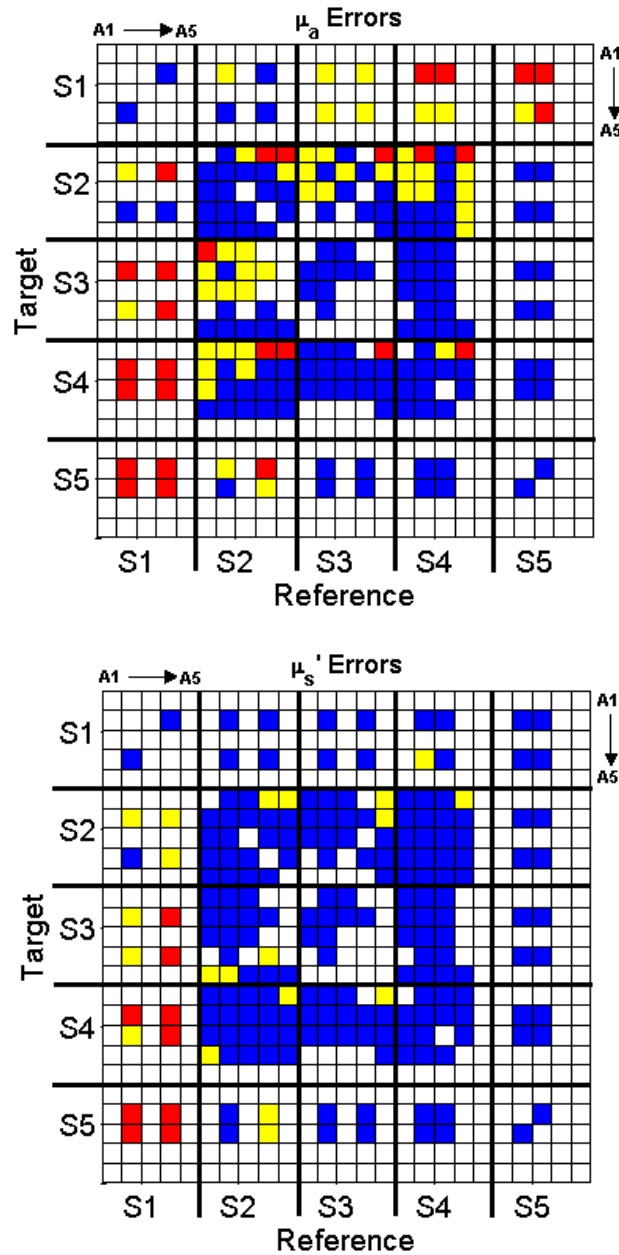


Figure 3: Error grids for μ_a (top) and μ_s' (bottom) for all reference-target combinations in the single absorber phantoms. Each small square represents a single reference-target phantom combination, defined by an absorption and scattering level. The scattering levels are split by each of the larger 5x5 squares, which consist of 5 absorber levels as noted for the S1. The blue squares indicate <10% error, yellow squares between 10-20% error, and red squares >20% errors. For μ_a errors, it is evident that A1 is a poor target compared to other absorption levels, presumably because the μ_a for A2-A5 were evenly spaced, while the μ_a for A1 was much lower. It is also evident from the μ_a grid that low scattering references (S1-S2) perform worse for high scattering targets (S3-S5), and also high scattering references perform worse for low scattering targets. This is also seen on a lesser scale with the μ_s' errors for the S1 reference and S3-S5 targets.

Based on the errors depicted in Figure 3, a master phantom reference list was generated. The 11 phantoms that comprised this list yielded average errors in μ_a and μ_s' less than 10% when used as a reference for all measured targets. Table 8 summarizes the master reference phantoms with corresponding optical properties.

Table 8: Absorber-scatterer levels with corresponding wavelength-averaged optical properties for the 11 master reference phantoms, which had <10% error in μ_a and μ_s' . Master reference phantoms were selected based on the errors in extracted μ_a and μ_s' from the SA_Hb_a, SA_Hb_b, and SA_Cr phantom sets.

| Phantom | Mean μ_a (cm ⁻¹) | Mean μ_s' (cm ⁻¹) |
|---------|----------------------------------|-----------------------------------|
| A1-S3 | 0.2 | 19.9 |
| A1-S4 | 0.2 | 24.8 |
| A2-S2 | 1.5 | 14.9 |
| A2-S3 | 1.5 | 19.9 |
| A2-S4 | 1.5 | 24.8 |
| A2-S5 | 1.5 | 29.7 |
| A3-S2 | 2.2 | 14.9 |
| A3-S3 | 2.2 | 19.9 |
| A3-S4 | 2.2 | 24.8 |
| A3-S5 | 2.2 | 29.7 |
| A4-S3 | 2.7 | 19.9 |

The master reference phantoms were used to test the effect of different instruments and probes on the extracted optical properties. SA_Hb_a and SA_Hb_b were tested using Probe A and both instruments and Probe B with the PMT-based instrument. Probe adaptors were custom-designed to allow Probe A to be compatible with both instruments. For Probe A and the CCD-based instrument, both the 1.9 and 10 nm bandpass settings were tested for SA_Hb_a. The three master reference phantoms common to both phantom sets - A3-S4, A2-S2, and A2-S4 - were used for all phantom targets. Table 9 shows the average percent errors in μ_a and μ_s' for all probe-instrument combinations.

Table 9: Extraction accuracy using master reference phantoms common to SA_Hb_a and SA_Hb_b across all targets for difference probe and instrument combinations. The errors in μ_a were significantly higher when the 10 nm bandpass setting for the CCD-based instrument was used. For the other instrument and probe combinations, there were no significant differences in either μ_a or μ_s' .

| | Probe A PMT | Probe B PMT | Probe A CCD | |
|----------------------------|-----------------|----------------|----------------|------------------|
| | | | 1.9 nm BP | 10 nm BP |
| SA_Hb_a | | | | |
| Mean error in μ_a (%) | 8.42 ± 11.3 | 4.66 ± 5.4 | 6.03 ± 5.9 | 23.20 ± 35.4 |
| Mean error in μ_s' (%) | 3.44 ± 2.1 | 5.32 ± 3.4 | 4.87 ± 3.4 | 3.18 ± 2.5 |
| SA_Hb_b | | | | |
| Mean error in μ_a (%) | 4.48 ± 4.9 | 3.94 ± 3.2 | 6.30 ± 6.4 | - |
| Mean error in μ_s' (%) | 4.21 ± 2.6 | 5.61 ± 3.7 | 4.27 ± 2.9 | - |

There were no significant differences in μ_a or μ_s' for any instrument and probe combination for either phantom set using the 1.9 nm bandpass setting for the CCD-based instrument, indicating the adaptability of the inverse Monte Carlo model to different system setups. When the 10 nm bandpass setting was used, the μ_s' errors were similar, but there was a significant increase in the μ_a errors. This indicates the increased accuracy in extracting the absorption coefficient when a narrow bandpass setting is used, possibly because the narrow bandpass enables hemoglobin spectral features to be captured.

2.3.2 Double Absorber Phantoms

The quantitative accuracy in extracting hemoglobin and crocin concentrations in double-absorber phantoms was tested. The effect of having reference-target phantoms from different days was assessed by using the five phantoms from SA_Hb_a contained in the master reference set - A3-S4, A2-S2, A2-S4, A1-S4, and A3-S2 - as references for the double-absorber phantoms. Figure 4 shows the expected versus extracted concentrations for hemoglobin (upper panel) and crocin (lower panel).

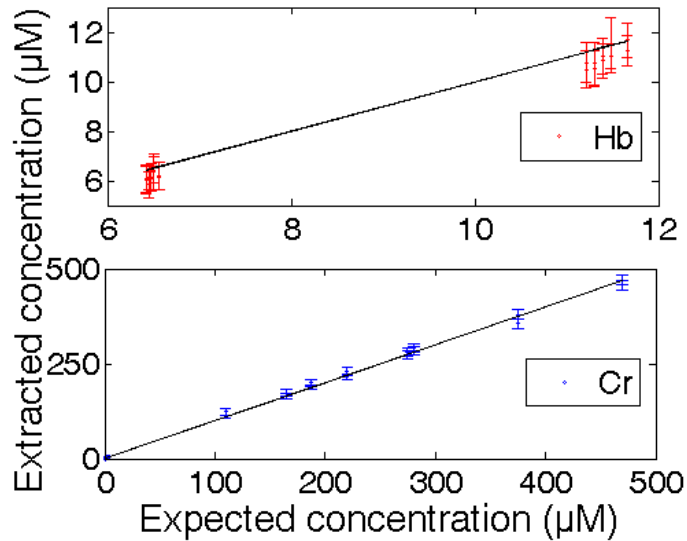


Figure 4: Extraction accuracy of hemoglobin (top) and crocin (bottom) in DA_HbCr when five master reference phantom measured on a different day were used. The means and standard deviations were calculated over the different reference phantoms. The proximity of the extracted to expected concentrations indicates the feasibility for the inverse Monte Carlo model to distinguish concentrations of individual absorbers. The hemoglobin concentrations are separated, because crocin was added incrementally to two initial levels of hemoglobin. The fluctuations in expected hemoglobin concentration are due to the dilutional effects of adding crocin.

The average percent error in extracting the concentrations of hemoglobin and crocin were $7.69 \pm 3.6\%$ and $4.40 \pm 4.0\%$, respectively. This shows excellent ability to extract concentrations when two absorbing species are present using reference phantoms measured on a different day.

2.3.3 Hemoglobin Concentration Phantoms

The quantitative accuracy in extracting hemoglobin over a large range of concentrations was tested using two reference levels contained in the master phantom set - A2-S5 and A3-S4, corresponding to phantoms H2 through H4 - and all targets in Conc_Hb. Figure 5 shows the concentration extraction accuracy using these same-day reference phantoms.

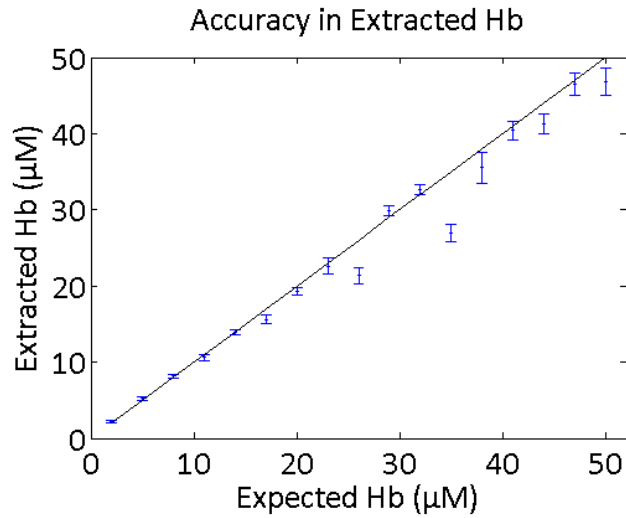


Figure 5: Extraction accuracy of hemoglobin using same-day master reference phantoms. Some of the phantoms towards the higher concentration levels had an underestimation of hemoglobin, which could be possibly be attributed to the fact that these phantoms covered absorption ranges beyond those shown in Figure 3.

The average percent error in extracted hemoglobin over these reference-target combinations was $6.37 \pm 6.6\%$, for μ_a it was $6.31 \pm 6.6\%$, and for μ_s' it was $8.15 \pm 8.5\%$.

2.3.4 Hemoglobin Saturation Phantoms

The concentration of oxy- and deoxyhemoglobin were extracted for the Sat_Hb phantom using the two same-day reference phantoms contained in the master reference set: A2-S2 and A3-S2. The extracted values are shown in Figure 6 (top). The expected hemoglobin saturation [12] was calculated for the range of measured oxygen partial pressures at $T=24\text{ }^\circ\text{C}$ and $\text{pH } 6.94$. The extracted and expected hemoglobin saturation is shown in Figure 6 (bottom).

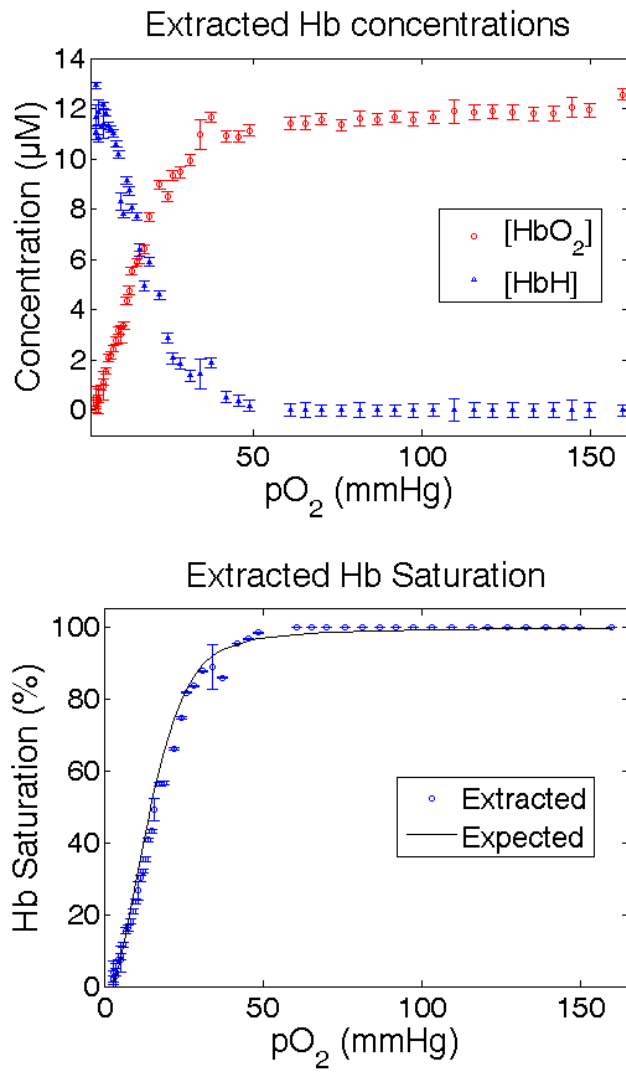


Figure 6: Extracted HbO₂ and HbH as a function of measured pO₂ (top) and extracted vs. expected hemoglobin saturation (bottom). The addition of yeast to the phantom resulted in a sharp initial desaturation of the phantom. Around 30 mmHg, the saturation began to level off, as indicated by the relative concentrations of HbO₂ and HbH and the composite hemoglobin saturation. Measurements were continued over an hour to ensure the desaturation process was complete.

The expected value for n and p_{50} are 2.44 and 14.46 mmHg, respectively. The extracted values for n and p_{50} from our phantoms were 2.40 ± 0.05 and 16.28 ± 0.3 mmHg, respectively, indicating excellent agreement with the predicted values.

2.4 Discussion

The studies discussed in this chapter were designed to assess how well the inverse Monte Carlo model performs in clinically-relevant laboratory experiments. Laboratory diffuse reflectance studies are advantageous in that the optical properties are known. Contrastingly, the optical properties of tissue are unknown, and so the model first has to be tested on a range of optical properties to assess the strengths and limitations. There were several conclusions from these studies. For one, the quantitative accuracy of extracting μ_a was enhanced when a 1.9 nm spectral bandpass compared to a 10 nm spectral bandpass was used on the CCD-based instrument. One potential explanation of the increased accuracy of μ_a with a smaller bandpass is that the structural features of hemoglobin can be more effectively captured.

Additionally, these studies identified a set 11 master reference phantoms with absorber-scatterer levels A3-S3, A4-S3, A1-S3, A2-S3, A3-S5, A2-S5, A3-S4, A2-S4, A2-S2, A1-S4, and A3-S2, in order of increasing percent error. These phantoms spanned from the A1 to A4 absorber level and the S2 to S5 scattering level. These reference phantoms gave the highest degree of accuracy in extracted μ_a and μ_s' for a wide range of target phantoms. These references serve as a guideline for measurements where the target tissue optical properties are unknown. If the scattering level of the target tissue could be known *a priori*, it would be best to use a reference phantom with a similar scattering level. If a reference phantom from level S1 or S2 was used to extract the optical properties from a target in S3-S5, the μ_a was typically overestimated. Conversely, when a reference from S3-S5 was used for a target in S1 or S2, the μ_a was typically underestimated. But because the target optical properties are unknown, the master reference set is the current solution to minimize errors in extracted absorption and scattering. Additionally, by having a set of reference phantoms to use for all samples measured in a particular clinical study, there is a reduction in the experimental bias that may arise from taking reference measurements on a daily basis.

Another important finding from these studies was that the concentrations of hemoglobin and crocin in a double-absorber phantom could be extracted with very good accuracy. The reference phantoms used to extract these concentrations were measured on a different day and contained only hemoglobin as the absorber. This is directly translatable to single absorber phantoms being used as references for tissue measurements in the clinical setting. However, in this study, and in other studies involving different-day reference-target phantoms, there are limitations in extracting μ_s' . The average percent error using the same reference phantoms discussed in “2.2.2.2 Double absorber phantoms” yielded μ_s' errors of $57.71 \pm 9.4\%$. The μ_a errors were comparable to the concentration errors: $5.52 \pm 2.8\%$. The inability to extract μ_s' accurately is a persistent problem and can likely be linked to the calibration procedure. Because μ_s' is primarily intensity-dependent while μ_a is shape-dependent, the accuracy suffers if the calibration standard cannot be measured in a repeatable manner. Development of calibration standard-probe adaptors is discussed in “4.2 Methods.”

From the Conc_Hb phantoms, phantoms from the master reference set were able to accurately extract the μ_a from all target phantoms. There was some offset noted at the higher concentrations, where the hemoglobin was somewhat underestimated. The underestimation of hemoglobin concentration as a function of concentration could perhaps be attributed to the differences in the signal levels between the low and high absorption phantoms. Because the integration time within the experiment was not varied as the concentration of hemoglobin increased, the signal level decreased. This signal mismatch may have caused an amplification of the noise and thus the errors. A mismatch in scattering could have also contributed to the errors in μ_a as the scattering level decreased from S4 to S2, due to the addition of absorber. Further work is required to develop a method to correct for the mismatch of scattering and absorption between the reference and target phantom or tissue.

The accuracy in measuring hemoglobin saturation values obtained from extracted HbO_2 and HbH concentrations in hemoglobin phantoms was investigated with the Hb_sat phantoms.

The values for the Hill coefficient and partial pressure of oxygen at which hemoglobin is 50% saturated were in excellent agreement with expected values.

The results from these phantom studies serves as a set of guidelines for parameters used in the collection and post-processing of clinical spectra which may potentially improve standard of care through increased quantitative accuracy.

3. *In Vivo* Diffuse Reflectance Measurements from the Sublingual Mucosa in Patients Undergoing Surgery

3.1 *Introduction*

Conventional measurements of hemoglobin concentration are invasive and time-consuming. In this chapter, a study in which the diffuse reflectance was measured from the sublingual mucosa (i.e. floor of the mouth) of patients undergoing major surgeries is discussed. A majority of this chapter is drawn from [55]. The sublingual mucosa was chosen because it is well-matched to interrogation with UV-VIS wavelengths; the area is highly vascular and perfused, and the thickness of the mucosal epithelium of the floor of the mouth is only 190 μm [29]. The sensing depths of the wavelengths and probe geometry discussed are on the order of 1-2 mm [55], making them well-suited to penetrate past the mucosal epithelium.

Initially, this study was designed to use the inverse Monte Carlo model [18] for noninvasive measurements of hemoglobin concentration. However, the correlations to expected hemoglobin measured invasively were weaker than expected, and so a ratiometric model capitalizing on the isosbestic points of oxy- and deoxyhemoglobin was developed instead. In the present chapter, results from both Monte Carlo and the ratiometric method are discussed. The ratiometric comparisons serve as preliminary data for “6. Development of a Ratiometric Method to Estimate Hemoglobin Concentration,” in which more rigorous simulation and phantom studies were involved in the development of the ratiometric algorithm.

3.2 *Methods*

3.2.1 Patient Study

Twenty patients undergoing surgery at Duke University Medical Center (Durham, North Carolina) were enrolled in this study. This study was conducted according to a protocol approved by the Duke University IRB and with the patient’s informed consent. During the course of the study, fibers in the probe broke, and this was assumed to start happening after

the fifth patient, based on comparative reflectance standard measurements from each patient. The cause of fiber damage was assumed to be due to the sterilization procedure. For the first 15 patients, the probe was sterilized in Cidex® along with other surgical equipment. Once the extent of the probe damage was realized, a new probe with the same fiber configuration as the original probe was manufactured and used for the remaining patients. For these last five patients, a different sterilization process was used, in which the probe was sterilized by ethylene oxide cold gas in an individual box away from other instruments. After each of the last five patients was measured, the probe was checked for damage by a microscope image of the common end of the fiber. No damage was observed over this time period. The data analysis here includes the 10 patients measured when the probe fibers were intact (the first five and last five patients).

After the patient was anesthetized, the anesthesiologist placed the sterilized fiber optic inside the patient's mouth, flush against the sublingual tissue. In most cases, the probe was taped to the endotracheal or nasogastric tube to stabilize against movement. In the first patient, the probe was taped directly to the side of the patient's mouth. For seven of the ten patients, the probe had to be either replaced or slightly readjusted during the procedure to ensure contact with the tissue. If the probe was dislodged during the surgery, as judged by the shape of the reflectance spectra, the anesthesiologist repositioned the probe as close to the original position as possible. Table 10 shows the types of surgery, number of data points, and range of hemoglobin values obtained from ABG for the 10 patients. Optical measurements were taken approximately every 15 minutes and every time an ABG was drawn. There were a total of 36 matched optical and ABG measurements for all patients.

Table 10: Types of surgeries, number of ABG and optical measurements, and range of hemoglobin obtained from the ABG. The surgeries were selected because they had the potential to result in a large amount of blood loss. Patient 3 had the highest range of Hgb out of all patients combined. The ABGs were collected as specified by standard of care, but optical measurements were collected in series approximately every 15 minutes.

| Patient | Surgery Type | # ABG | # Optical | Hgb range (g/dl) |
|---------|---------------------------|-------|-----------|------------------|
| 1 | Anterior spinal fixation | 4 | 68 | 8.2 - 12.4 |
| 2 | Radical hysterectomy | 3 | 62 | 10.1 - 12.3 |
| 3 | Liver resection | 7 | 111 | 4.5 - 15.3 |
| 4 | Exploratory laparotomy | 3 | 60 | 8.7 - 12.0 |
| 5 | Cervical spinal fusion | 2 | 31 | 12.2 - 12.5 |
| 6 | Pancreas whipple | 4 | 96 | 10.9 - 13.1 |
| 7 | Hernia | 3 | 43 | 11.0 - 14.4 |
| 8 | Abdominal aortic aneurysm | 3 | 17 | 9.0 - 12.3 |
| 9 | Bile duct resection | 2 | 27 | 10.0 - 11.0 |
| 10 | Radical prostatectomy | 6 | 96 | 6.2 - 13.5 |

3.2.2 Optical Measurements

Diffuse reflectance spectra were measured using the PMT-based instrument and probe described in “1.4 Diffuse Reflectance Spectroscopy.” The probe was 5 m in total length, 4 m of which was enclosed in Teflon coating, making it fairly flexible and adaptable to the operating room where due to space constraints the instrument could not always be placed directly next to the patient. The instrument was allowed to warm up for at least 15 minutes prior to the onset of measurements. The diffuse reflectance was collected from 350-600 nm, in 5 nm increments (51 data points), using an integration time of 0.1 s per data point for all measurements. At the beginning or end of a set of patient measurements, the diffuse reflectance from a Spectralon reflectance standard (SRS-99-010, Labsphere, Inc., North Sutton, NH) was measured using the same instrument settings to record day-to-day variations in instrument throughput.

3.2.3 Data Analysis

3.2.3.1 Inverse Monte Carlo model

The quantitative accuracy of using the inverse Monte Carlo model [18] was tested by correlating extracted optical total hemoglobin to ABG hemoglobin. Data was calibrated by a

reference phantom from the master reference set (Table 8) that was measured with the same instrument and probe. The inversion procedure involved calibration between the reference and phantom day-to-day instrument variations by dividing the target spectra by a ratio of the reflectance standard measured during the clinical case to the standard measured during the phantoms. Different wavelength ranges were tested for the analysis, but only the results for 460-600 nm are shown in the results, as they yielded the best correlations.

3.2.3.2 Ratiometric method

Because the correlations with the inverse Monte Carlo model were not very strong, the quantitative accuracy of using wavelength ratios was also tested, via correlations between all reflectance ratio pairs between 350-600 nm and ABG hemoglobin values. Because the spectra were collected in 5 nm increments, the data was first interpolated to a 1 nm increment using a cubic spline interpolation. Ratios were tested on raw data, due to the inconsistency of reflectance standard measurements throughout the course of the study. No adaptor was used to secure the probe to the reflectance standard, and the measurements were taken in different operating rooms with the overhead lights on.

For both the Monte Carlo and ratiometric data, correlations of both raw and baseline-subtracted values were tested. Baseline-subtraction was achieved by:

$$\Delta X(1:n-1) = X(2:n) - X(1) \quad (10)$$

The variable X represents the ABG, optical hemoglobin, or a wavelength ratio, and n refers to the total number of measurements for a given patient. Because the number of ABG time points per patient was highly variable, all data was combined for the analyses. Correlations were tested using Pearson's linear correlation coefficients, which assume the data is normally distributed.

3.2.4 Probe Pressure in Volunteers

The effect of probe pressure on Monte Carlo-extracted hemoglobin and the isosbestic ratios was tested in sub-studies using two volunteers. The probe was placed inside a rubber

tubing on which the volunteer bit lightly to hold the probe in place. Also surrounding the probe within the rubber tubing was a clear sheath to ensure additional security. The clear sheath extended past the rubber tubing and was clamped to the probe at the distal end for each measurement. The probe tip was not covered by the tubing or sheath (Figure 7). The security of the probe in the volunteer measurements was designed to be comparable to that of the clinical measurements, where the probe was taped in.

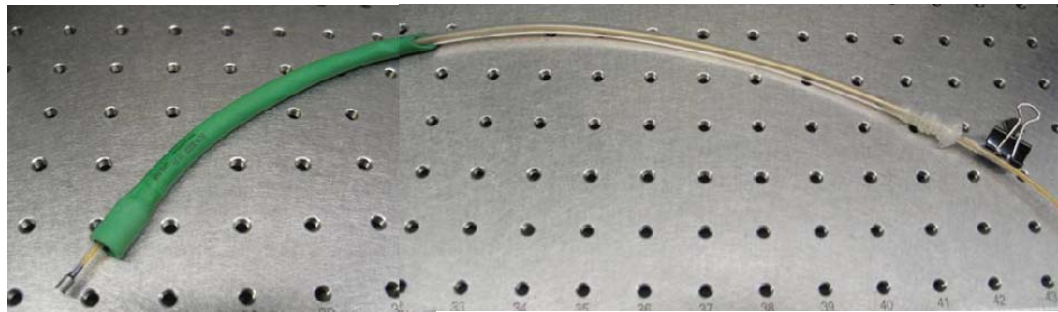


Figure 7: Photograph of the optical probe with tubing applied for the volunteer measurements. The green rubber tubing was added to allow the volunteer to bite and hold the probe in place without damaging the probe fibers. The clear sheath was used as a surface on which a clamp could be applied to ensure the probe did not move within the rubber tubing during the course of the measurements.

The probe was positioned on the sublingual tissue of a volunteer, and the instrument operator (myself) varied the pressure between “light,” “medium,” and “hard.” The pressure was qualitative, where the volunteer motioned when they felt like the pressure change was significant. For each pressure change, the clamp was secured on the clear sheath for the duration of the measurements. Measurements were taken from both the right and left side of the sublingual tissue, and each side was measured a second time after the probe was removed then replaced (Right 1, Right 2, Left 1, Left 2). Once the probe was replaced on a given side, it was situated with approximately the same starting pressure. Duplicate measurements were taken for each placement of the probe per site.

3.3 Results

3.3.1 Inverse Monte Carlo Model

The correlations of optically extracted total hemoglobin over 460-600 nm are shown for raw data (left) and baseline-subtracted data (right) using the Monte Carlo model (Figure 8).

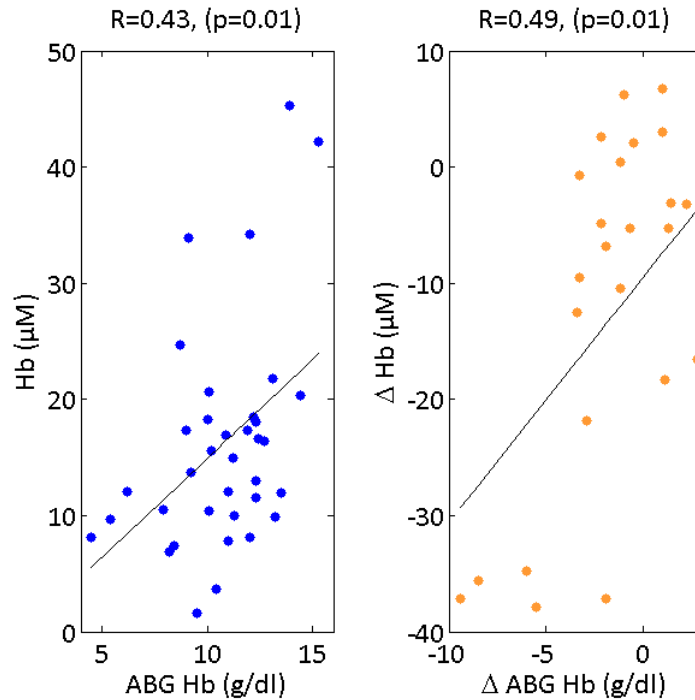


Figure 8: Monte Carlo-extracted total hemoglobin versus ABG hemoglobin for all 10 patients combined. The black line represents the best linear fit to the data. The p-values represent the test of the hypothesis of no correlation against nonzero correlation. Both the raw and baseline-subtracted data are show statistically significant correlations, but by visual inspection the correlations look somewhat weak.

The correlations between optical and ABG hemoglobin were significant for both raw and baseline-subtracted data, with a slight improvement in the correlation coefficients (from $r=0.43$ to 0.49) with baseline-subtraction.

3.3.2 Ratiometric Method

The correlations between all reflectance ratio pairs between 350-600 nm and ABG hemoglobin values were tested. The correlations are plotted in Figure 9 for raw (top) and baseline-subtracted (bottom) data. The color map represents the absolute value of the linear

correlation coefficient for ABG hemoglobin compared to each numerator-denominator pair, with red representing the highest correlation and blue representing the lowest. The color map is normalized to the range of r values, and so the colors can not be directly compared between the figures. The maximum r value for the baseline-subtracted data was higher than that for the raw data. The numerator and denominator are indicated by the y- and x-axis, respectively, the axes of which are labeled by the isosbestic points of oxy- and deoxyhemoglobin.

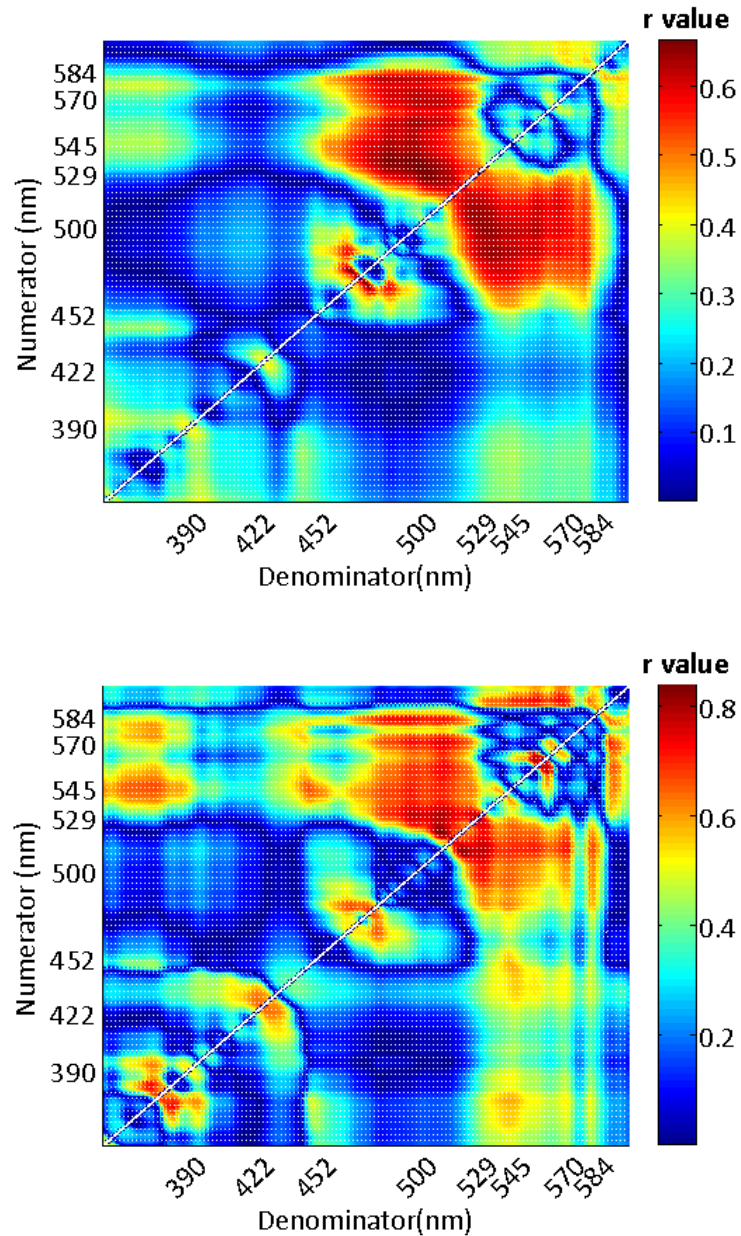


Figure 9: Grids showing the strength of linear correlation between ABG hemoglobin and all numerator-denominator optical ratios. Raw (top) and baseline-subtracted (bottom) comparisons are shown. The patterns for raw and baseline-subtracted data are similar, but the overall magnitude of the r value is generally higher for the baseline-subtracted data, indicating some correction for inter-patient variability.

The regions with the best raw correlations ($r > \pm 0.65$) were where the numerator was between 524-537 nm and the denominator between 482-507 nm, or when the numerators were 474-475 nm and denominators 466-467 nm. The reverse case where the numerator was 466-467

nm and the denominator was 474-475 nm also had $r > \pm 0.65$. The best correlation was for 532/499 nm ($r=-0.67$). The ratio of 532/499 nm is close to the isosbestic ratio of 529/500 nm ($r=-0.66$). Because the correlation coefficients were so similar for both these ratios, 529/500 nm was retained as the best raw optical correlate to ABG hemoglobin.

For baseline-subtracted data, the correlations were very strong ($r > \pm 0.8$) for numerators ranging from 519-522 nm and 508-510 nm and corresponding denominator ranges of 507-511 nm and 519-521 nm respectively. The ratio that had the best correlation was 520/509 nm, with $r=-0.84$. The nearest isosbestic points in this range are 529 and 500 nm, which correlated to delta ABG hemoglobin with $r=-0.75$ for 529/500 nm. The non-delta 520/509 nm correlation with ABG hemoglobin was $r=-0.61$. Figure 10 shows the raw and delta correlations for both 529/500 nm (top) and 520/509 nm (bottom).

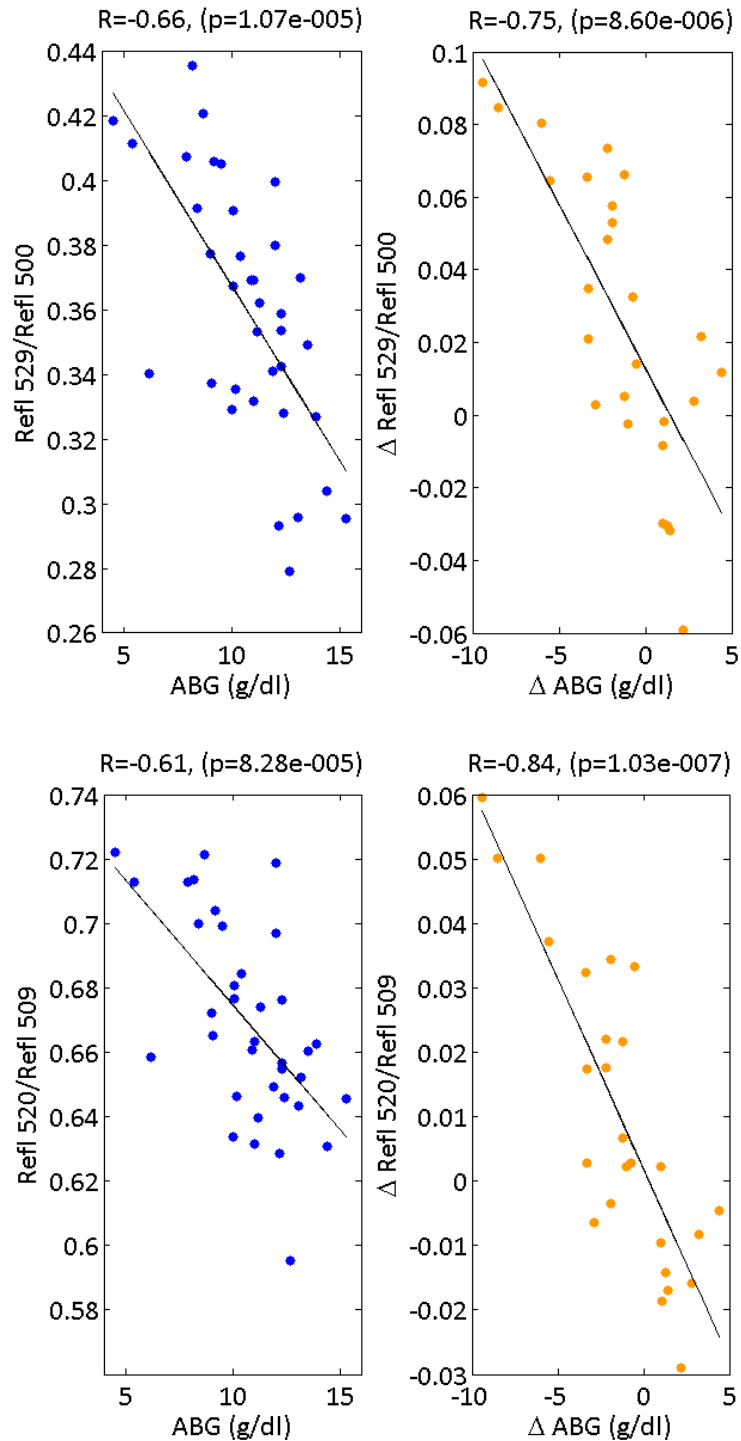


Figure 10: 529/500 nm (top) and 520/509 nm (bottom) with versus ABG hemoglobin for all 10 patients combined. The black line represents the best linear fit to the data. The p-values represent the test of the hypothesis of no correlation against nonzero correlation. For both ratios, the baseline-subtraction improved the linearity of the data, as evidenced by the higher r values.

To test the feasibility of the ratios in tracking hemoglobin concentration over time, a double y-axis plot of all measurements from the patient with the widest range of ABG hemoglobin values is shown (Figure 11), where the left axis and solid line show the continuous optical ratio measurements, and the right axis and blue dots show the intermittent ABG hemoglobin measurements. The shaded region was during the time where a cumulative blood loss volume of 1600 ml was noted on the anesthesia chart. The top figure shows the raw data and the bottom the baseline-subtracted data. It is evident in this single patient that the baseline-subtraction may help account some systematic offset in the raw measurements.

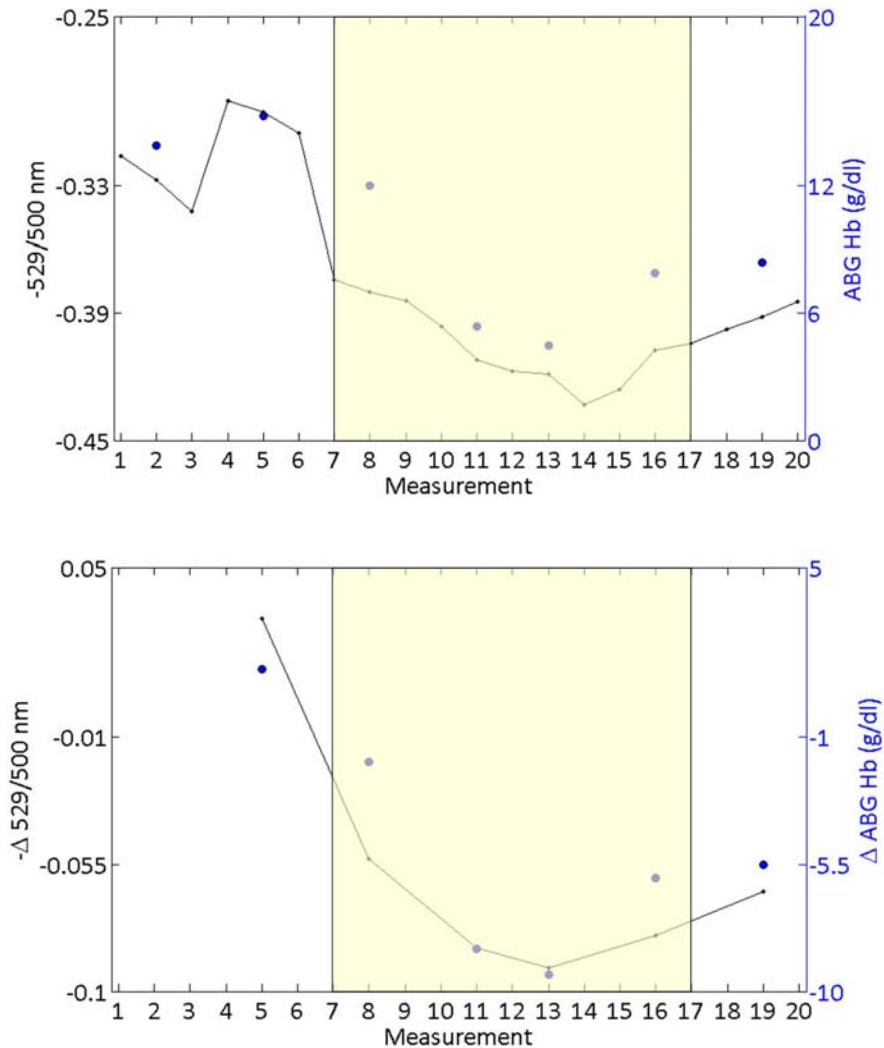


Figure 11: Feasibility for hemoglobin monitoring over time using the 529/500 nm optical ratio. The solid line shows optical ratios (left axis), and the blue dots show ABG hemoglobin (right axis). The top plot is raw comparisons, and the bottom plot is baseline-subtracted. The yellow box represents the time during which 1600 ml blood loss occurred. Both raw and baseline-subtracted optical ratios capture the trend of the blood loss, where a decrease in the ratio is seen with blood loss and a subsequent decrease in ABG hemoglobin. Data is from a single patient (Patient 3). The ratios are shown as negative, to illustrate the trends more intuitively.

3.3.3 Simulations

Monte Carlo simulations [76] were carried out to test the effect of a range of hemoglobin concentrations and saturations on the 529/500 nm isosbestic ratio. Nine tissue models were simulated with total hemoglobin levels between 4-35 μM and hemoglobin

saturations from 25-100%. The μ_s' was kept constant at 8.15 and 7.99 cm^{-1} for 529 and 500 nm, respectively (based on values from Table 3). The simulations used a probe geometry with a central illumination fiber diameter of 1.1 mm and detector fiber of 200 μm (both with NA = 0.22) with center-center source-detector separation being 0.71 mm. This probe geometry was selected to model the probe used for experimental measurements. The diameter of the illumination fiber was determined by measuring the effective diameter of the probe illumination core.

For all tissue models, the anisotropy factor, g , was set to 0.8, and the refractive indices for the fibers and tissue were set at 1.45 and 1.37, respectively [55, 77]. The simulation used one million photons and a homogeneous medium with thickness and radius of 3 cm, divided into grids of 0.01 cm (depth) x 3 cm (radial). Each model was simulated for one million photons and a semi-infinite homogeneous medium. The diffuse reflectance for the collection fiber in the simulations were used to determine the simulated reflectance at 529 and 500 nm, which in turn were used to compute the reflectance ratio. The relationship between the concentration and 529/500 nm optical ratio is shown in Figure 12.

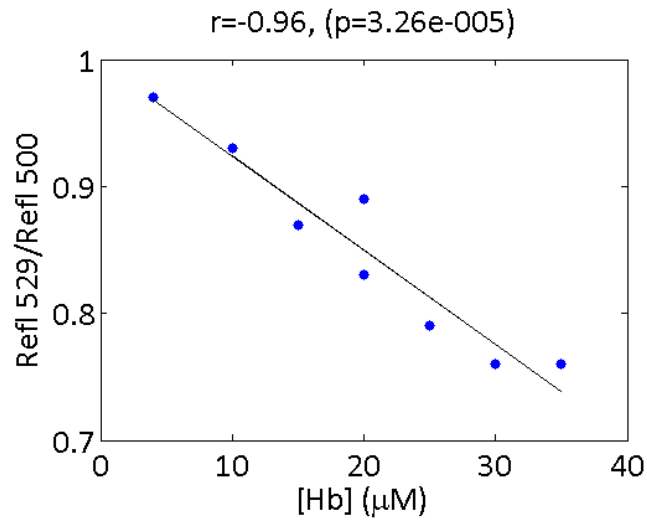


Figure 12: Relationship between 529/500 nm and hemoglobin concentration as determined from simulations. The black line shows the line of best fit for hemoglobin concentration. The results from these simulations show excellent correlation of the 529/500 nm ratio with hemoglobin, for the single scattering level on which it was tested.

The ratio was very strongly correlated to hemoglobin concentration with $r=-0.96$. The hemoglobin saturation, which ranged from 25-100%, did not exhibit a strong correlation with the reflectance ratio ($r=0.03$), which supports the theory that the isosbestic ratio should be independent of saturation.

The effect of scattering on the 529/500 nm reflectance ratio was tested for total hemoglobin concentrations of 4, 15, 25, and 35 μM . First, $\mu_s'(529 \text{ nm})$ was fixed at 8 cm^{-1} , and then different values of μ_s' at 500 nm were evaluated. The $\mu_s'(500 \text{ nm})$ was varied from 1, 1.5, 2, and 2.5 times the $\mu_s'(529 \text{ nm})$, to give respective $\mu_s'(529 \text{ nm}):\mu_s'(500 \text{ nm})$ ratios of 1, 0.67, 0.5, and 0.4. Linear regression was tested between 529/500 nm and hemoglobin; the slopes were relatively similar for different scattering ratios, but there was a linear offset in the decay line with variation in the scattering ratio. The equations describing the linear fits for $\mu_s'(529 \text{ nm}):\mu_s'(500 \text{ nm})$ ratios of 1, 0.67, 0.5, and 0.4 respectively were $y=-0.006x+0.9$, $y=-0.007x+0.7$, $y=-0.004x+0.5$, $y=-0.004x+0.4$, where x refers to the concentration and y refers to the 529/500 nm reflectance ratio. The intercepts were roughly equal to $\mu_s'(529 \text{ nm}):\mu_s'(500 \text{ nm})$.

3.3.4 Probe Pressure in Volunteers

Because pressure could not be controlled in the clinical study, the effects of probe pressure on the Monte-Carlo extracted hemoglobin and the 529/500 and 520/509 ratios were tested in two volunteers (Volunteer 1 and 2). Two sites (right and left) on the sublingual tissue were each tested twice (Right 1, Right 2, Left 1, Left 2), with three qualitative pressures per site. For Volunteer 1, the probe accidentally moved on the second scan for high pressure of site Right 2, so only the first scan was considered. Figure 13 shows the reflectance standard-calibrated diffuse reflectance spectra from Right 1 for both volunteers.

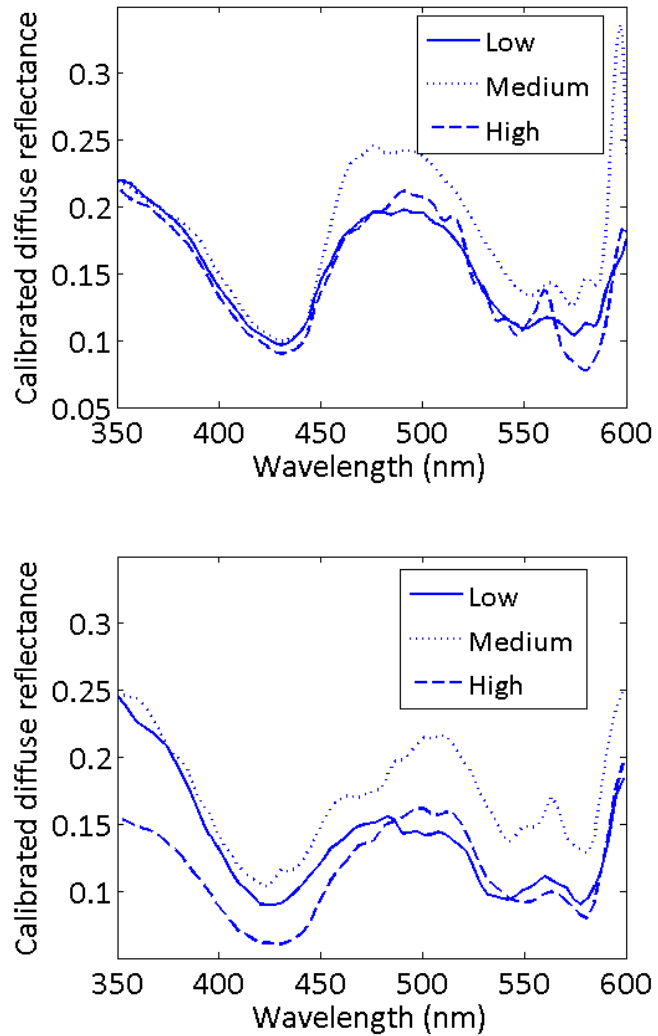


Figure 13: Diffuse reflectance for Volunteer 1 (top) and Volunteer (2) for the Right 1 site per pressure. The diffuse reflectance is divided by the spectrum of the reflectance standard for visualization, but the ratios were calculated from raw spectra.

Monte Carlo inversions were carried out using one reference phantom from the master reference set (Table 8) measured with the same instrument and probe. Ratios were calculated from the raw diffuse reflectance spectra. Figure 14 shows the extracted hemoglobin from Monte Carlo, the 529/500 nm ratio, and the 520/509 nm ratio for Volunteer 1 (left) and Volunteer 2 (right). The bars are in order of duplicate measurements of light, medium, and high pressure, as indicated for the first site.

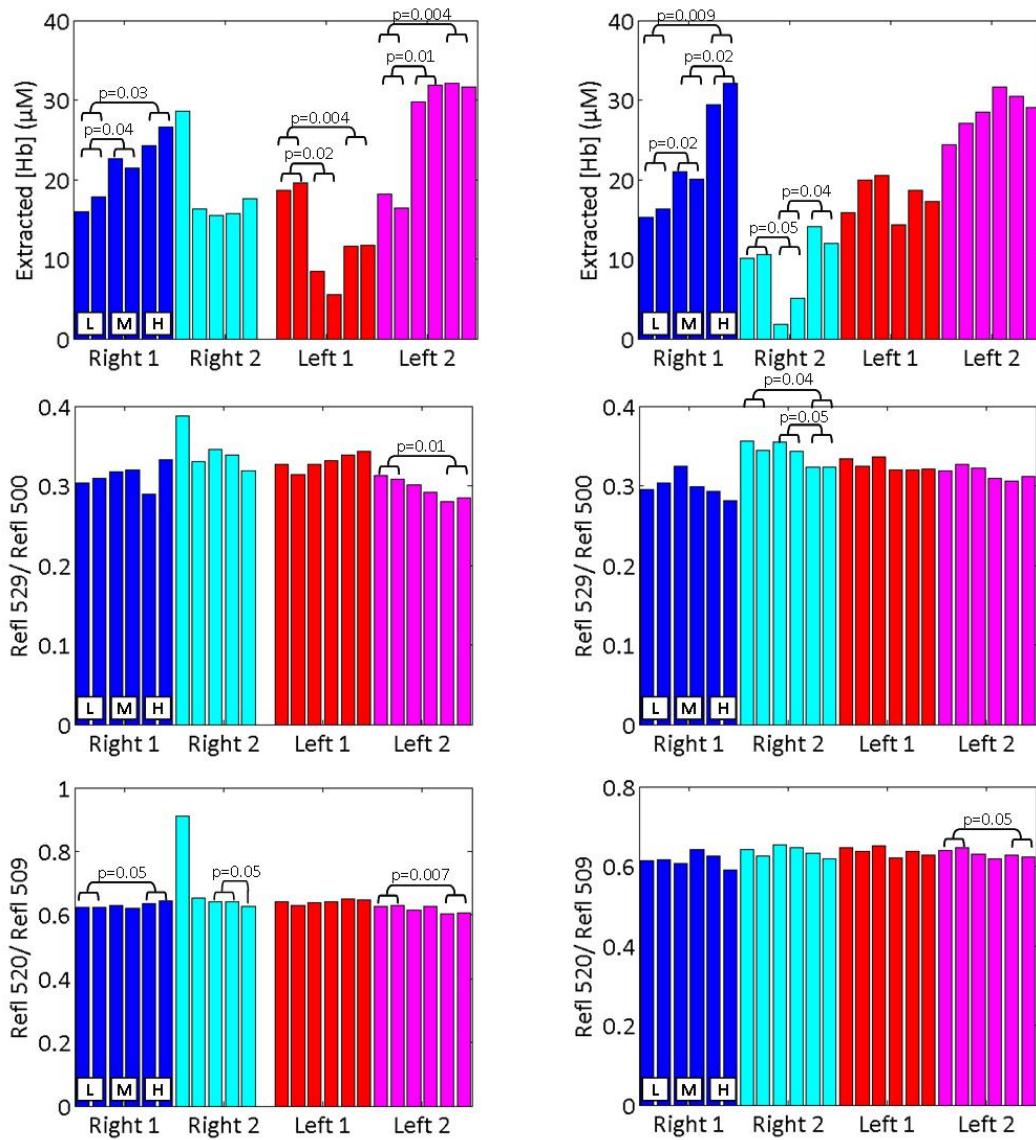


Figure 14: Monte Carlo-extracted hemoglobin (top), 529/500 (middle), and 520/509 nm (bottom) for Volunteer 1 (left) and Volunteer 2 (right) as a function of increasing probe pressure per site. The qualitative pressures are indicated for the first site as (L)ight, (M)edium, and (H)igh. The p value testing the statistical differences between the two measurements for any given set of pressures is shown if it was less than or equal to 0.05.

For Volunteer 1, there were statistically significant differences between light and medium pressure for Right 1, Left 1, and Left 2 as well as between light and high pressure for the same three sites using the Monte Carlo data. For the ratiometric comparisons, the only statistically significant differences for 529/500 nm were between light and high pressure for

Left 2, and for 520/509 nm, there were differences between light and high for Right 1 and Left 2, as well as between medium and high for Right 2. For Volunteer 2, for the Monte Carlo data there were differences between light and medium pressure as well as medium and high pressure for Right 1 and 2, plus there were differences between light and high for Right 1. For 529/500 nm, there were significant differences for Right 2 between high pressure with both light and medium pressure. For 520/509, there were only significant differences between light and high pressure for Left 2.

For the ratiometric data, there were no significant differences between light and medium pressure for either ratio, whereas for the Monte Carlo data there were. High pressure requires a lot of effort, and so the fact that there were statistically significant differences between low/medium and high pressure for several of the sites measured is not a significant concern. Based on this preliminary data, the 529/500 and 520/509 nm ratios are less susceptible to changes than the extracted hemoglobin from Monte Carlo. During the patient study, best efforts were made to maintain a low to medium pressure and avoid high pressures since that would be painful to the patient's mouth.

3.4 Discussion

The simulations presented here were limited compared to those presented in “6. Development of a Ratiometric Method to Estimate Hemoglobin Concentration.” The ones here were used simply to illustrate the relationship between the best isosbestic ratio and ABG hemoglobin as measured in the patient data. We show the potential to correlate simple diffuse reflectance ratios to hemoglobin values obtained from ABG measurements during intra-operative procedures in a pilot study. It is of clinical interest to have a simple monitor that is not complex in terms of the algorithm used; this is why ratios of diffuse reflectance were evaluated. The diffuse reflectance system used here can be built more compactly, thus increasing the portability. The isosbestic ratio 529/500 nm yielded good correlations with ABG hemoglobin, with $r=-0.66$ (compared to $r=0.43$ for Monte Carlo extracted hemoglobin). Delta

comparisons, measured by subtracting the baseline for both 529/500 nm and ABG hemoglobin, were improved, with $r=-0.75$. The best delta ratio was 520/509 nm, with an $r=-0.84$ (compared to $r=0.49$ for Monte Carlo extracted hemoglobin). Non-delta 520/509 correlated with ABG hemoglobin with $r=-0.61$. Delta comparisons helped improve correlations of ratios with ABG hemoglobin. By subtracting the baseline value in each patient, the comparisons are on the amount of change rather than on the absolute value. Given the improved correlations in the delta correlations, it can be presumed that the non-delta ratios did not completely account for inter-patient variations in pressure. The ability to extract hemoglobin better with the ratiometric method may be due to the fact that correction by the reflectance standard was not required.

For the first five patients alone, non-delta 529/500 nm was correlated to ABG hemoglobin with $r=-0.78$. Patient #10 was shown to negatively impact the correlations the most, as determined by adding the last five patients one at a time to the first five. The correlations for individually adding patients #6-10 to patients #1-5 were $r=-0.80$, $r=-0.79$, $r=-0.78$, $r=-0.75$, and $r=-0.65$, respectively. If patient #10 was excluded from the total patient population, the 529/500 nm ratio was correlated to ABG hemoglobin with $r=-0.77$. The delta correlation for the 520/509 nm ratio when patient #10 was excluded had $r=-0.85$, which is similar to the correlation when all patients were included. It is unclear at this time why patient #10 negatively impacted the non-delta correlations. In any case, delta comparisons seem to address any potential interpatient variability that might arise in the non-delta based correlations.

Diffuse reflectance ratios are expected to correlate well with hemoglobin, because absorption of hemoglobin is a primary source of contrast in the spectra. Isosbestic ratios are taken where the oxy- and deoxyhemoglobin molar extinction coefficients are equal, and so they would not be expected to correlate with the partial pressure of oxygen in the arterial plasma (PaO_2). For one of the patients, there was one PaO_2 value missing, giving a total of 35 paired optical and PaO_2 measurements. There was not a notable correlation between the

isosbestic reflectance ratio of 529/500 nm and PaO₂ ($r=0.25$, $p=0.15$), indicating the isosbestic ratio is influenced by hemoglobin but not PaO₂. The Monte Carlo simulations, carried out for a range of hemoglobin concentrations and saturations, justify the strong negative correlation expected from the 529/500 nm reflectance ratio with total hemoglobin ($r=-0.96$) and also demonstrate that this ratio is not influenced by changes in hemoglobin saturation. When the ratio of scattering between 500 and 529 nm was varied, the 529/500 nm reflectance ratio was still negatively correlated to hemoglobin with comparable slopes for different scattering ratios. However, the intercept of linear regression of 529/500 nm with hemoglobin was strongly dependent on the ratio of $\mu_s'(529)$ to $\mu_s'(500)$ ($r=1$). For the patient data, the intercept of the experimental 529/500 nm reflectance ratio versus ABG hemoglobin was 0.5, which was close to the averaged 529/500 nm ratio from the Spectralon reflectance standards for all 10 patients (0.4 ± 0.02). The reflectance standard is nearly spectrally flat in the wavelength range used, so the ratio effectively reflects the wavelength dependence of the system at 529 and 500 nm. It can be inferred that the intercept for the 529/500 nm ratio versus ABG hemoglobin in the patient data would be close to unity. Based on examination of the simulation data this suggests that the scattering values in the patient data are likely very similar at 500 and 529 nm reflecting an intercept close to unity. The slope for the experimental 529/500 nm reflectance ratio versus concentration was -0.01. In the simulations, the slope was -0.006 for the μ_s' ratio of 1, which was slightly lower than the experimental ratio.

The reflectance ratio also showed potential to correct for pressure variations of the probe against the tissue surface as measured in two volunteers. There were no significant differences between low and medium pressure for the ratios, whereas the differences were more pronounced for the Monte Carlo extracted hemoglobin. To the best of our knowledge, there have been no recommendations of ways to correct for pressure-induced differences in diffuse reflectance data. Based on the volunteer study described here, the isosbestic ratio 529/500 nm appears to help account for pressure variations.

We have demonstrated the ability to achieve good correlations of simple diffuse reflectance ratios and blood gas parameters in a preliminary set of patient data, despite the fact that the blood gas measurements probe on the systemic level and optical measurements probe on the tissue level. The ABG measures direct concentrations of hemoglobin in arterial blood, while diffuse reflectance measures a volume of tissue comprised of both arterial and venous components in capillary beds. The Fahraeus effect indicates the hematocrit in capillaries is generally lower than systemic hematocrit; this can be affected by capillary diameter and whether vasodilation is present [78, 79]. Because of the different probing areas between optical and ABG measurements, the relationship would not necessarily be linear. Additionally, the presence of other absorbers could affect the linearity. However, the linear correlations in this study serve as a first pass at correlating regional physiological information to global hemoglobin. The goal of this technique is to serve as a non-invasive technology for monitoring patient physiological parameters over time or guiding when ABG measurements should be drawn.

4. NIR Measurements Using an Inverse Monte Carlo Model and a Steady-State System

4.1 Introduction

Diffuse reflectance measurements using UV-VIS wavelengths are restrictive, because the absorption of hemoglobin is high in that regime. Thus, in a biological setting, only superficial vasculature will be exposed to the incident light [80]. For longer wavelengths (600-1300 nm), where the absorption of hemoglobin and melanin are relatively low, the light can penetrate deeper and over a larger volume and so these wavelengths are termed the optical window of tissue [80]. Because of this, NIR wavelengths are useful for measuring tissue surfaces covered by skin. The purpose of this chapter was to assess whether the inverse Monte Carlo model [18] can be used with measurements in the NIR. To date, the inverse Monte Carlo has only been validated in the UV-VIS wavelength regime [23, 28].

The probe geometry is also important when considering penetration depth of light. Short source-detector separation distances are suitable for superficial measurements, whereas longer separations are necessary to collect the reflectance that has traveled deeper in the tissue [81]. The probes used for Monte Carlo validation in the UV-VIS had short separations, and so a side-firing geometry with longer separations was modeled for the NIR wavelengths. The goal of the simulations and laboratory measurements described in this section was to find a way to transition to wavelengths where the probe placement could be on the skin surface. Placement on the skin is more secure than on a mucosal site, because the probe can be more easily affixed with the use of tape. The use of a side-firing geometry allows for more direct placement of the probe against the skin as well [22].

Figure 15 shows the steps taken to test the feasibility of Monte Carlo analysis for a steady-state instrument and NIR wavelengths. The goal of this chapter is to determine whether more accurate measurements in the NIR can be achieved with Monte Carlo and a steady-state instrument or diffusion approximation and a frequency-domain instrument. Bing Yu, who is a

member of our lab, has already done extensive validation of a FD photon migration system with NIR wavelengths and diffusion approximation [22].

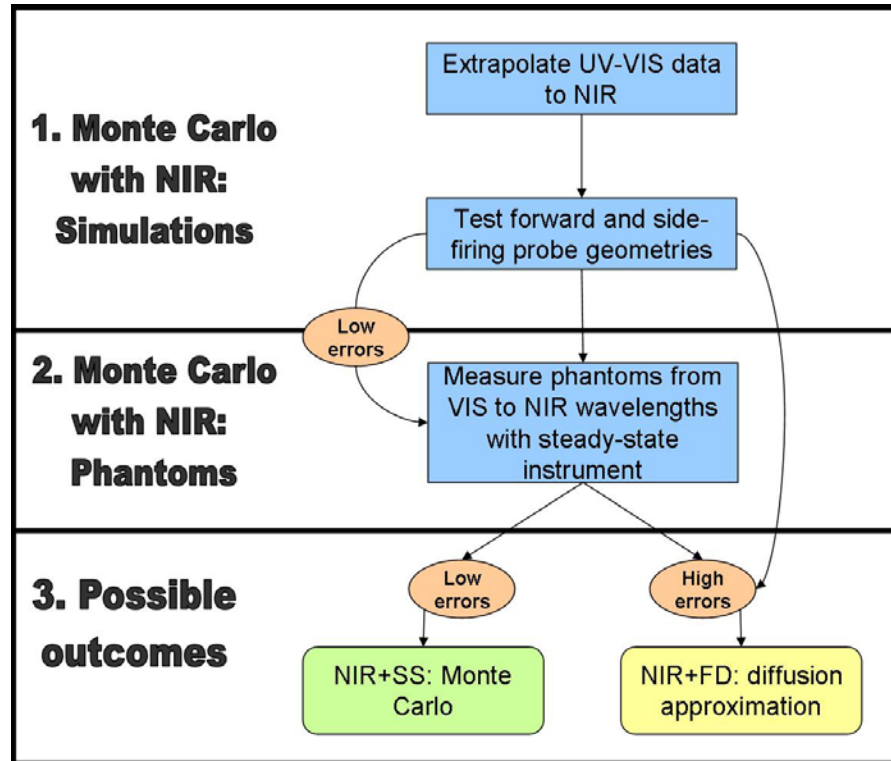


Figure 15: Flow chart summarizing the steps taken to assess the feasibility of Monte Carlo on steady-state measurements at NIR wavelengths. If the simulations or the phantom measurements indicate there are problems with steady-state Monte Carlo and NIR wavelengths, the backup plan is the use the well-characterized frequency-domain system with diffusion approximation analysis.

There were two main parts to this assessment of the inverse model with NIR wavelengths. First, the theoretical feasibility was tested by extrapolating UV-VIS phantom data into the NIR. The μ_a and μ_s' were extrapolated using knowledge about the absorber shape and the scattering properties, then these were used to generate a reflectance spectrum [18]. Because the reflectance was generated using the Monte Carlo model itself, the inverse case of extracting the constituent μ_a and μ_s' should provide an exact solution. The second part of the assessment incorporated liquid phantoms measured from the VIS to the NIR. The ability to extract the optical properties from these phantoms tested both the inverse Monte Carlo model as well as the instrument capabilities. For this portion of the experiments, an available

instrument with the best efficiency in the NIR was used to help minimize any biases due to the instrument.

4.2 Methods

4.2.1 Simulated NIR Data from Phantoms

The goal of the simulations was to test how well the Monte Carlo model could extract μ_a and μ_s' independent of instrument effects. To achieve this, phantom data measured in the UV-VIS was extrapolated to the NIR. The μ_a and μ_s' were first extrapolated to 600-900 nm, then used in conjunction with the exact probe geometry to generate the diffuse reflectance at the corresponding wavelengths using a lookup table. These steps were carried out using the Monte Carlo model [18], and so the extrapolation represents the best-case scenario, because the extrapolated reflectance was determined from the Monte Carlo lookup table. For the extrapolation procedure, one reference phantom contained in the master set (Table 8) was used to obtain the extracted μ_a and μ_s' from a set of 10 phantoms similar to the SA_Hb_a set described in “2.2.2.1 Single absorber phantoms” (Table 3). The reference and target phantoms were measured on the same day. The phantoms were measured with the PMT-based instrument.

For μ_a , the known extinction coefficients for oxyhemoglobin [59] were interpolated to match the increment for the extrapolation wavelengths (600-900 nm, with a 5 nm increment). Then the extracted hemoglobin concentration, Hb_{ext} , from a phantom inversion from 350-600 nm was used to calculate the extrapolated μ_a by:

$$\mu_{a:NIR} = Hb_{ext} \cdot \varepsilon_{HbO_2:NIR} \cdot \ln(10) \quad (11)$$

$\varepsilon_{HbO_2:NIR}$ is the wavelength-dependent extinction coefficient in the extrapolated wavelength range and the natural log of 10 is required to relate concentration to μ_a (Beer’s Law).

The μ_s' was extrapolated using the scatter size and scatter factor that were calculated by the inverse Monte Carlo model [18]. More specifically, the extrapolated μ_s' spectrum was

determined by multiplying the scatter factor by the spectral shape determined from a lookup table based on the refractive index of the spheres, wavelength, and the scatter size. Figure 16 shows an example of the extrapolation into the NIR for μ_a and μ_s' for a phantom contained in the master reference set.

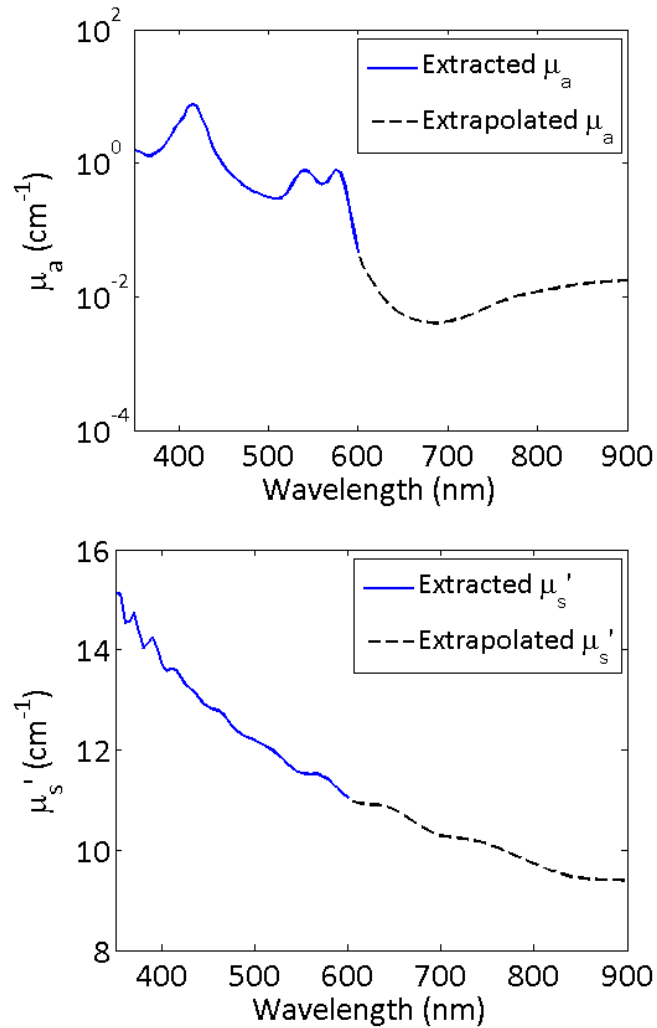


Figure 16: Phantom-extracted μ_a (top) and μ_s' (bottom) from 350-600 nm (solid blue line) and corresponding extrapolated optical properties (dashed black line) from 600-900 nm. The μ_a is plotted on a log-y scale, so that the spectral features at all wavelengths are evident. This data was from a phantom measured with the PMT-based instrument. The phantoms contained only oxyhemoglobin as the absorber. The reduction of spectral absorption features is evident in the NIR.

Upon determining the extrapolated μ_a and μ_s' , the reflectance for the entire wavelength range of 350-900 nm could be determined from a lookup table using a scaling object generated for the desired probe geometry, along with the μ_a and μ_s' over the entire wavelength range. Two probe geometries were used for this: 1) the forward-firing probe that was used to measure the phantoms and 2) a side-firing geometry that has been used previously

to measure phantoms and tissues in the NIR [22]. The fiber configurations for the two probe geometries are shown in Figure 17.

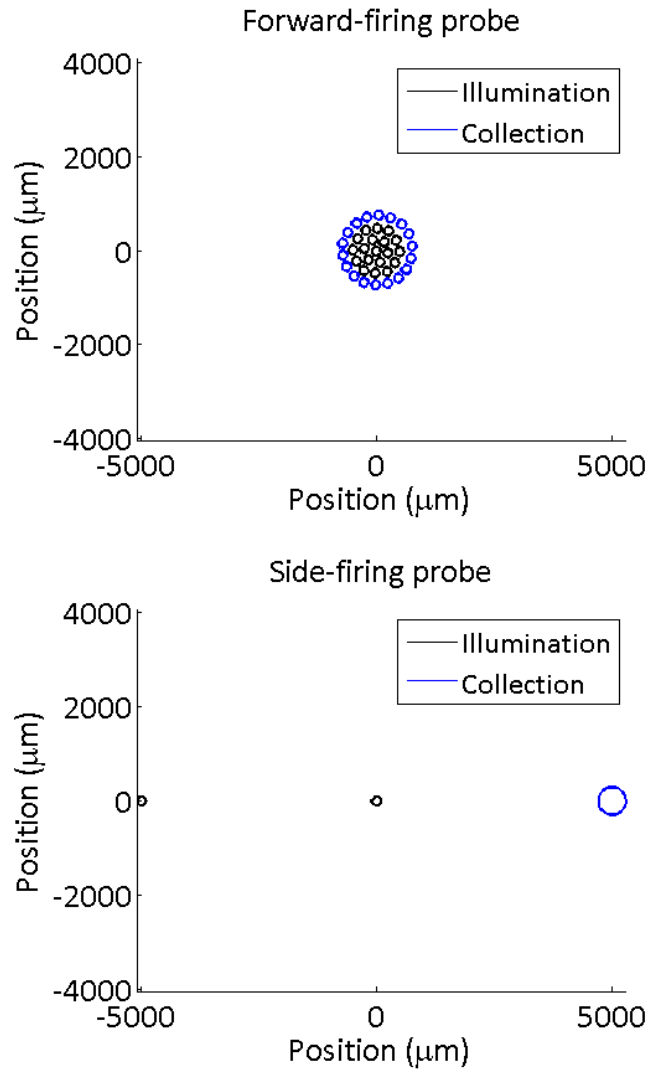


Figure 17: Probe geometries for the forward- (top) and side-firing (bottom) probes. The forward-firing geometry was determined from a microscopic image of the fiber end of the probe, whereas the side-firing geometry was defined based on an ideal configuration of a previously used probe. Both plots have the same scales; the forward-firing probe has short source-detector separations, which are applicable for the UV-VIS, while the side-firing geometry includes longer separations, applicable for the NIR.

The forward-firing probe had 19 illumination fibers surrounded by an 18-fiber collection ring. The side-firing probe had two illumination fibers, spaced 5 and 10 mm from a single collection fiber. The illumination fibers for the side-firing probe, as well as both the

illumination and collection fibers in the forward-firing probe, had diameters of 200 μm . The collection fiber for the side-firing probe was 600 μm . For the purposes of these simulations, the side-firing probe was not modeled with 45° fibers, which is the configuration of the actual probe, but the illumination-collection spacing matched the side-firing probe discussed in [22], and so the name was retained. The side-firing probe was designed for measurements in the NIR, which is why it was considered for these simulations.

4.2.2 Phantoms

Phantoms were measured using a portable diffuse reflectance spectroscopy system, comprised of a tungsten halogen lamp (HL-2000, Ocean Optics, Dunedin, FL) as the source and a miniature spectrometer with a linear CCD array as the detector (USB2000, Ocean Optics, Dunedin, FL). This system will be referred to as the USB-based system. The lamp and spectrometer were coupled to a probe custom-designed and constructed in-house. The probe consisted of one illumination fiber and one collection fiber, separated by 1 mm. A side-firing probe was not available for the USB-system, and this 1 mm-separation probe had been validated in other phantom studies. The USB-system was used because it is more sensitive to NIR wavelengths than the CCD- and PMT-based instruments; the grating efficiency for the CCD instrument and the efficiency of the Xe lamp for both instruments are reduced past 600 nm [82]. The USB-based instrument has a detector range of 200-1100 nm, and the tungsten-halogen lamp has increased efficiency in the NIR compared to the Xe lamp [82].

Two sets of phantoms similar to SA_Hb_a and SA_Hb_b, as described in “2.2.2.1 Single absorber phantoms” (Table 3), were measured on different days. The only difference was that the first μ_a level for these phantoms had hemoglobin set to be in series with the remaining μ_a levels rather than being much lower. This modification was made because phantoms with the lowest μ_a were shown to be poor targets in Chapter 2. The range of collected signal was from 178-889 nm, split into increments corresponding to the 3648 pixels in the CCD array. The best signal levels were achieved from 450-800 nm, and so the spectra were only analyzed within

portions of that range. Each diffuse reflectance spectrum was dark-corrected, and the lights were turned off for the measurements. The phantoms were each measured at two to four different integration times, ranging from 100 to 200 ms. Prior to data analysis, the spectra were all divided by their respective integration time.

Prior to measuring the spectra from the phantom, the diffuse reflectance from a reflectance standard was measured using the same instrument settings as used for the phantoms, but with integration times ranging from 400-500 ms. The integration times for the phantoms and reflectance standard were selected based on the linear range of the detector. Because of the presumed issues with repeatable probe positioning on the standard, an adaptor was custom-designed to ensure repeatable probe placement (Figure 18).

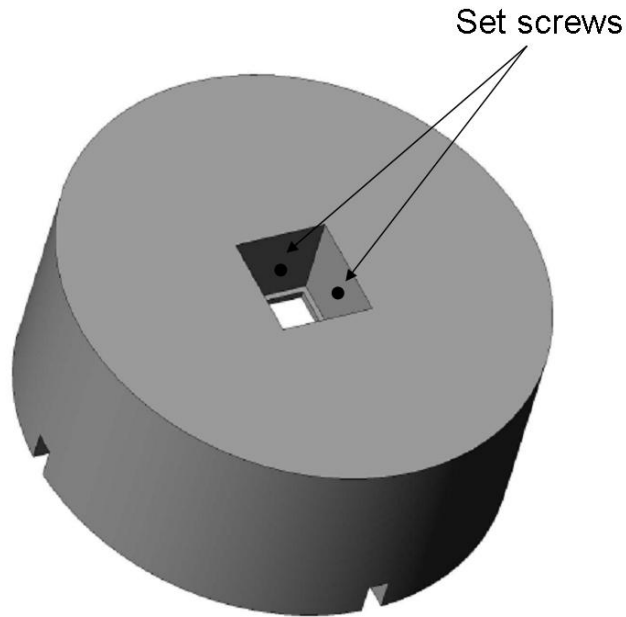


Figure 18: Computer model of the top piece for the probe-reflectance standard adaptor. The adaptors were made of black Delrin®, so that the light reflection off the surface would be minimized. The notches fit over a second piece which was secured to the reflectance standard. The set screws ensured the probe could be held firmly in place during the measurements.

The adaptor fit snugly over a smaller ring that could be secured on the reflectance standard (not shown). The smaller ring had two screws that emerged from the outside of the

piece that corresponded with the notches seen in the figure. The two screws indicated by the arrows were in place to secure the probe into the adaptor. The probe had a rectangular plastic covering around the fibers that fit securely in the adaptor. The probe rested on the ledge, so that it was 0.04 inches above the reflectance standard. Thus the probe did not actually touch the reflectance standard, eliminating concerns about the standard getting dirty over time. The reflectance standard was secured into the inner ring in the same position during the course of these experiments, and so the placement was repeatable. In addition, the probe was placed into the adaptor with the same orientation of the fibers each time.

4.3 Results

4.3.1 Simulated NIR Data from Phantoms

The generated diffuse reflectance spectra for each phantom are shown for the forward- and side-firing probes in Figure 19. The legend indicates which phantom the reflectance corresponds to; the number refers to the relative scattering level and the letter refers to relative absorber level (i.e. “1C” is a phantom with the lower scattering level and the third absorber level). The scattering levels were similar to S2 and S4, and with the exception of the lowest absorber level, the absorption levels correspond to A2-A5 (Table 3). The lowest absorber level was higher than the A1 level, so that it was in series with the other four levels.

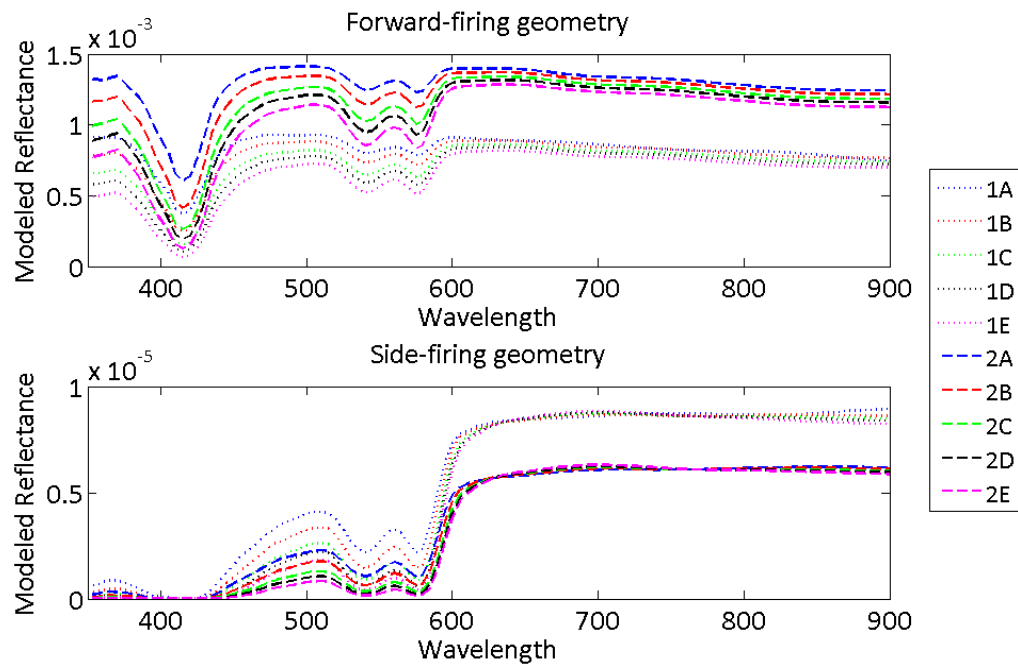


Figure 19: Diffuse reflectance generated for the forward- (top) and side-firing (bottom) probes from 350-900 nm. The legend indicates the phantom; the number represents the scattering level and the letter indicates the hemoglobin level (i.e. 2E has the highest scattering and absorption levels). It is of interest to note the increased reflectance at NIR wavelengths with the side-firing probe. Because of the larger separations, this probe is more sensitive to NIR wavelengths. Comparison between the absolute magnitudes of the modeled reflectance spectra is not necessary, since the probes had different numbers of illumination and collection fibers.

The reflectance at the UV-VIS wavelengths was much lower than at the NIR wavelengths with the side-firing geometry, whereas the forward-firing probe collected comparable signal levels at all wavelengths. Studies of photon migration have indicated that photons detected at greater lateral distances from the source travel further in depth in the medium [81, 83]. Because the detector configuration for the side-firing probe consists of large separations, it follows that the collection efficiency for the NIR photons, which have traveled deeper in the phantom, would be higher than the UV-VIS photons. Because the absorption of hemoglobin is higher in the UV-VIS compared to the NIR, it is intuitive that much of the signal would be lost due to absorption when the separations are large. Because of the number of

fibers and because the separations are much closer for the forward-firing probe, this discrepancy between the UV-VIS and NIR is not as notable as it is for the side-firing probe.

In addition, the relative reflectance between low and high scattering is opposite for the forward versus side-firing probe. For the forward-firing probe, the phantoms with higher scattering have higher reflectance, whereas for the side-firing probe, the phantoms with lower scattering have higher reflectance. This signifies that when the scattering is high, more of the photons may be lost when the separations are too large and there are fewer fibers. The overall signal from the forward-firing probe is orders of magnitude higher than that from the side-firing probe, attributable to the number of illumination and collection fibers in the forward-firing probe.

The ability to extract μ_a and μ_s' using Monte Carlo-generated NIR diffuse reflectance was tested for the forward- and side-firing geometries. For both probe geometries, the diffuse reflectance was generated from phantoms measured from 350-600 nm with the forward firing probe. All reference-target combinations were tested for the ability to extract μ_a and μ_s' from the Monte Carlo-generated spectra from 600-900 nm. Table 11 summarizes the average percent errors for both probe geometries.

Table 11: Average percent errors for μ_a and μ_s' using diffuse reflectance generated from 600-900 nm with a forward- and side-firing geometry probe. The errors for the forward-firing probe indicate it performs nearly perfectly, which is expected because the forward-firing geometry was used to measure the phantoms from which this data was generated. The side-firing probe performs excellently, with some minor errors in μ_a and μ_s' , which could be attributed to the mismatch between the probe used to measure the phantoms and generate the NIR data.

| | Forward-firing | Side-firing |
|----------------------------|-----------------------|--------------------|
| Mean error in μ_a (%) | 0.03 ± 0.01 | 1.47 ± 1.6 |
| Mean error in μ_s' (%) | 0.00 ± 0.0 | 0.15 ± 0.1 |

The errors were nearly perfect (0%) for the forward-firing geometry, while they were slightly higher for the side-firing geometry. Because the phantoms for which the data was extrapolated were measured with the forward-firing probe, it is not concerning that the side-firing probe errors were not perfect.

Additionally, the ability to extract μ_a , μ_s' , and hemoglobin concentration using different-day reference and target NIR generated data was tested. Here, the forward-firing probe was considered to illustrate the best-case scenario. The reference and target phantom studies were similar to the ones described in “2. Assessment of the Robustness of the Inverse Monte Carlo Model,” where the reference phantoms consisted of 17 additions of hemoglobin for one scattering level (like Conc_Hb), and the target phantoms consisted of five additions of hemoglobin for two scattering levels (like SA_Hb_a, as described earlier). Figure 20 shows the average percent error in extracted μ_a and μ_s' for inversions for 350-900 nm. The μ_a and μ_s' had perfect agreement between expected and extracted values, indicating the theoretical feasibility of NIR measurements with the inverse Monte Carlo model.

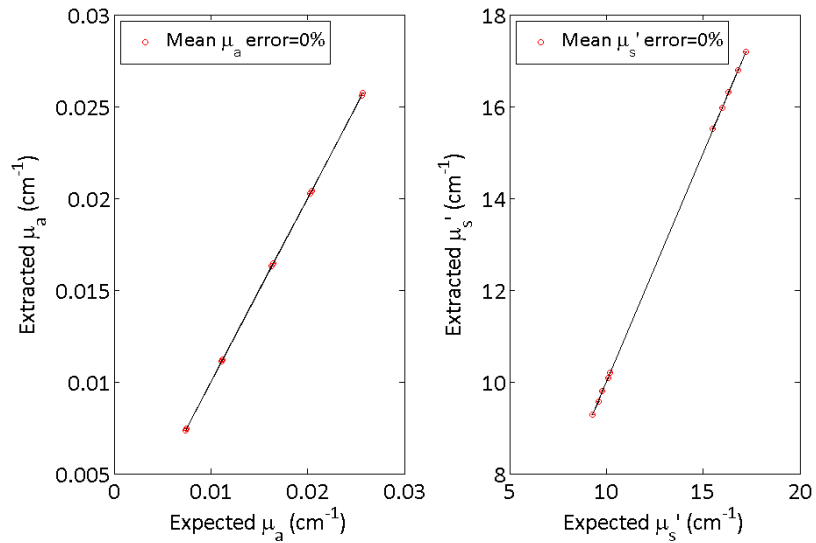


Figure 20: Extracted versus expected μ_a (left) and μ_s' (right) for different-day reference-target inversions using extrapolated data from 600-900 nm. The solid lines are the lines of perfect agreement for the expected parameters. The perfect agreement between extracted and expected μ_a and μ_s' can be explained because the extrapolated data on which the inversions were performed were generated by Monte Carlo.

4.3.2 Phantoms

In the previous section, the “no-noise” case of extracting optical parameters in the NIR with Monte Carlo was validated. In order to assess the impact of instrumentation factors on the

feasibility of steady-state Monte Carlo with NIR wavelengths, experimental measurements were conducted on phantoms. These phantoms had the same μ_a and μ_s' levels as were described in the previous section, but a different instrument and probe were used than the ones which formed the basis for the extrapolated data. The extraction accuracy for μ_a and μ_s' was tested for 450-600 and 600-800 nm for both the reference and target phantoms (Table 12).

Table 12: Average percent errors in μ_a and μ_s' for inversions from 450-600 and 600-800 nm in phantom studies. The errors for μ_s' seem mostly independent of wavelength range, while the μ_a errors increased when the 600-800 nm range was used. The errors are higher than those seen in previous phantoms, perhaps due to the simplified probe geometry.

| | 450-600 nm | 600-800 nm |
|----------------------------|---------------------------|--------------|
| | <i>Reference phantoms</i> | |
| Mean error in μ_a (%) | 7.69 ± 2.9 | 27.20 ± 6.9 |
| Mean error in μ_s' (%) | 10.74 ± 2.2 | 12.33 ± 4.2 |
| | <i>Target phantoms</i> | |
| Mean error in μ_a (%) | 12.95 ± 7.0 | 30.47 ± 10.5 |
| Mean error in μ_s' (%) | 10.23 ± 2.5 | 8.97 ± 5.0 |

The μ_a errors were worse when the inversions were performed over 600-800 nm, but the μ_s' errors seem independent of wavelength range.

In addition, the extraction of optical parameters from target phantoms measured on a different day from the reference set was tested. In an effort to reduce the noise in the NIR wavelengths (where the absorption of hemoglobin is much lower than in the VIS), the stock itself was measured from 600-800 nm. This contrasts with the general method of measuring a diluted stock solution to maximize the absorbance at the Soret band of hemoglobin. Despite this effort, the ability to extract μ_a and μ_s' was very poor (Figure 21).

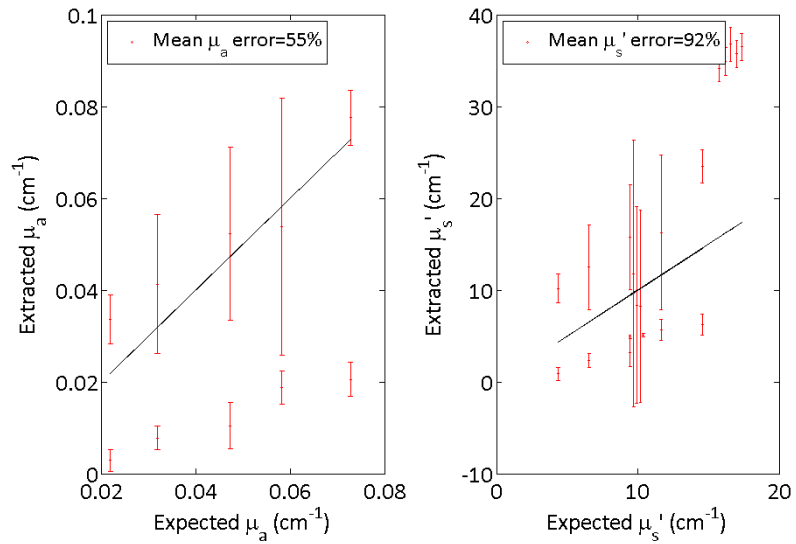


Figure 21: Errors in μ_a and μ_s' for 600-800 nm using different-day reference-target phantoms. The extraction ability of both optical parameters is very poor. The μ_a errors may be attributed to the fact that the absorption in the 600-800 nm wavelengths is much lower than in the UV-VIS wavelengths, which are where the inverse Monte Carlo model has been previously validated.

4.4 Discussion

One of the major limitations consistently seen with the steady-state instrument coupled with Monte Carlo is the inability to accurately extract μ_s' when the reference and target phantoms are from different days. This was touched upon in “2.4 Discussion”. The frequency-domain system is expected to suffer much less from different-day variations, as the absolute intensity does not matter but rather just changes in the amplitude and phase. Figure 22 shows the extraction accuracy in μ_s' for steady-state phantoms (top) and frequency-domain phantoms (bottom).

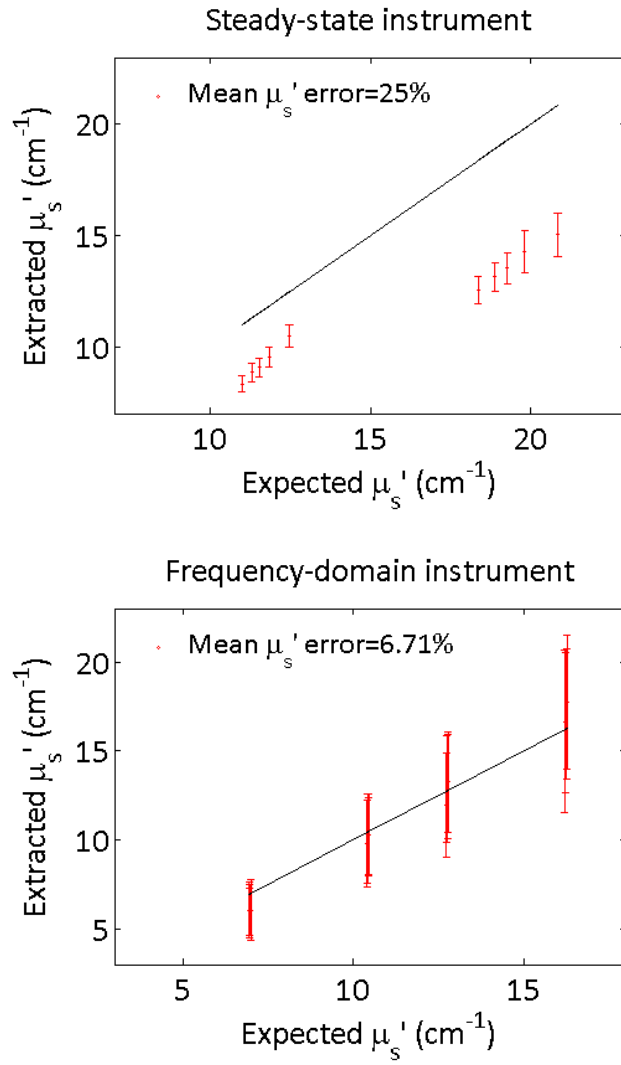


Figure 22: Average percent errors in μ_s' for the steady-state (top) and frequency-domain (bottom) phantoms inverted with different-day references. For the SS instrument, averages are for all reference phantoms, while for the FD instrument, averages are shown for each wavelength. Because there is a systematic offset seen with the extracted μ_s' from the SS instrument, it is hypothesized this is due to the inability to fully correct for lamp intensity from day-to-day. Because the μ_s' determined from the FD instrument is intensity-independent, the offset is not observed.

The different-day errors for μ_a were comparable between the steady-state and frequency-domain instruments because it is an intensity-independent measurement, but the errors in μ_s' were clearly worse for the steady-state instrument. The steady-state phantoms consisted of hemoglobin and polystyrene spheres, while the frequency-domain phantoms consisted of ink and Intralipid as the absorber and scatterer, respectively.

The results from this chapter have shown that NIR measurements with the steady-state instrument combined with Monte Carlo analysis results in high errors in estimation of both μ_a and μ_s' when the target and reference are measured on different days. The forward Monte Carlo simulations supported the feasibility of this method, and so it is assumed the reason it performed poorly experimentally was due to factors associated with the instrument or probe. Even with an adaptor (Figure 18) to ensure repeatable coupling with the reflectance standard, issues still exist with the steady-state Monte Carlo method. The inherent advantage of using the FD system is that a reflectance standard does not need to be measured to correct for different-day variations.

One of the major sources of error might be due to the measurements of the reflectance standard, even with an adaptor. For example, it was determined that the method of cleaning has an effect on the signal measured from the reflectance standard. After each phantom measurement, the probe tip must be cleaned to remove residual hemoglobin and polystyrene spheres. A simple experiment was conducted using the instrument and probe discussed in this chapter, where the probe was dipped in a phantom containing hemoglobin and polystyrene spheres then cleaned using one of six methods: 1) water → isopropyl alcohol (IPA) → compressed air, 2) water → Sparkleen → water → compressed air, 3) water → Sparkleen → IPA → compressed air, 4) Cavi wipe → air, 5) CaviWipe → IPA → compressed air, and 6) water → CaviWipe → compressed air. For “water,” the probe was dipped in a beaker of water, and for IPA, some of the IPA was squirted on the probe then dabbed off. Sparkleen (04-320-4, Fisher Scientific, Pittsburgh, PA) is a detergent that used to remove organic and inorganic deposits. Compressed air is used to ensure the probe tip is completely dry before the next measurement. CaviWipes (11-1100, Metrex, Orange, CA) are medical-grade disinfecting cloths. An initial measurement was made (dark blue line), and then three measurements per method were made in series (Figure 23).

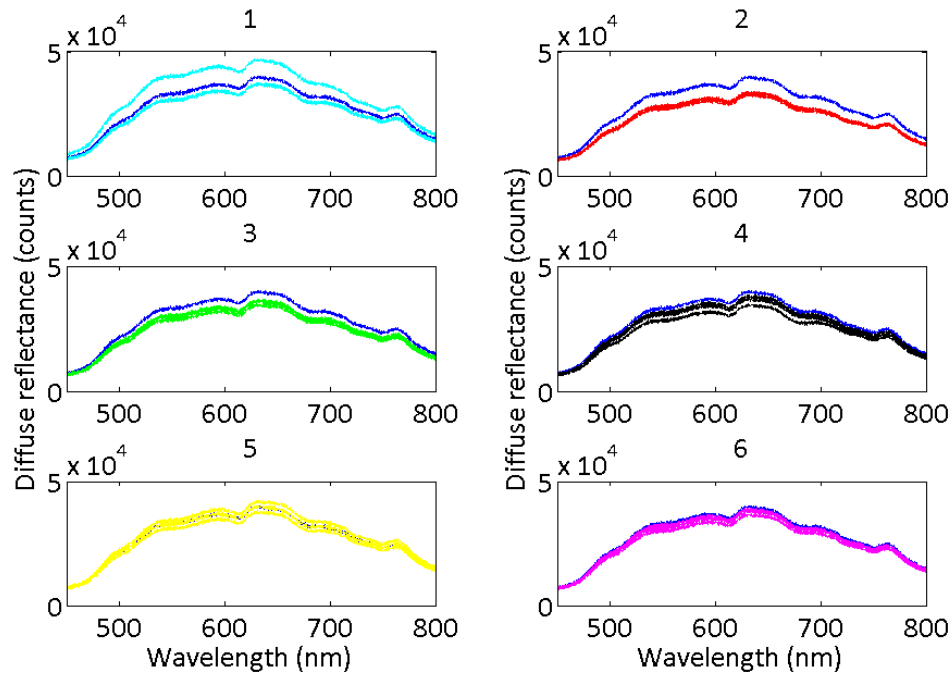


Figure 23: Measurements made on the reflectance standard with different probe cleaning methods. The blue line shows the diffuse reflectance before any cleaning was done. Then a series of cleaning methods were repeated three times each (different color lines) with the probe dipped in a phantom between each method. The six methods were as follows: 1) water → IPA → air (cyan), 2) water → Sparkleen → water → air (red), 3) water → Sparkleen → IPA → air (green), 4) CaviWipe → air (black), 5) CaviWipe → IPA → air (yellow), 6) water → CaviWipe → air (magenta).

From this figure, it is evident that the cleaning method affects the diffuse reflectance signal. The best methods appear to be methods #5 and #6. In any case, because of this discrepancy between cleaning methods, and because the NIR wavelengths with steady-state and Monte Carlo yield such high errors for different day reference-target combinations compared with the frequency-domain instrument, we made the choice to use the frequency-domain instrument for the hypovolemia study discussed in “5. *In Vivo* Diffuse Reflectance Measurements from the Thenar Eminence in Volunteers Undergoing Hypovolemia.”

5. *In Vivo* Diffuse Reflectance Measurements from the Thenar Eminence in Volunteers Undergoing Hypovolemia

5.1 Introduction

An FD system coupled with a side-firing optical probe [22] was used to take noninvasive measurements from the thenar eminence of human subjects undergoing induced hypovolemia and subsequent retransfusion. The goal of the study was to determine the sensitivity of noninvasive measurements of tissue oxygenation and hemoglobin concentration to hypovolemia. The choice of tissue site and instrument were guided by the difficulties in tissue probe interfacing discussed in “3. *In Vivo* Diffuse Reflectance Measurements from the Sublingual Mucosa in Patients Undergoing Surgery” coupled with the results from “4. NIR Measurements Using an Inverse Monte Carlo Model and a Steady-State System.” The thenar eminence, which is the muscular area below the base of the thumb, was used for several reasons. For one, the melanin content of the palm is less variable between people than other skin-covered areas. Plus, the thickness of the epithelium covering the palm is 1.7 ± 0.4 mm [31], which is suitable for NIR wavelengths and long source-detector separations, which have probing depths on the order of several mm up to cm. The probe used was a side-firing probe [22], which has the advantage of being placed flush against the tissue surface.

5.2 Methods

5.2.1 Patient Study

Fifteen healthy volunteers were enrolled in this study, which took place at the Duke University Medical Center (Durham, North Carolina). This study was conducted according to a protocol approved by the Duke University IRB and with the patient’s informed consent. Exclusion criteria for the study included smoking, low or abnormal hemoglobin blood levels, cardiorespiratory disease, gastrointestinal pathology, and pregnancy. This study was part of a

larger study which involved other noninvasive measurements of hemoglobin concentration and saturation using instruments and probes currently marketed in the United States. These additional methods will not be described in detail. Briefly, there were three VIS optical probes (Spectros T-Stat®) that measured tissue oxygenation in the oral mucosa, esophagus, and rectum. Three additional NIR probes - one from Masimo® and two from Casmed® - measured hemoglobin concentration from the fingertip. The two Casmed probes were placed on opposite fingers. The Casmed probes measured oxy- and deoxyhemoglobin, and so those were summed to obtain total hemoglobin concentration.

Once all the other probes were placed, the side-firing probe was situated on the thenar eminence of the non-dominant arm of the volunteer (Figure 24).

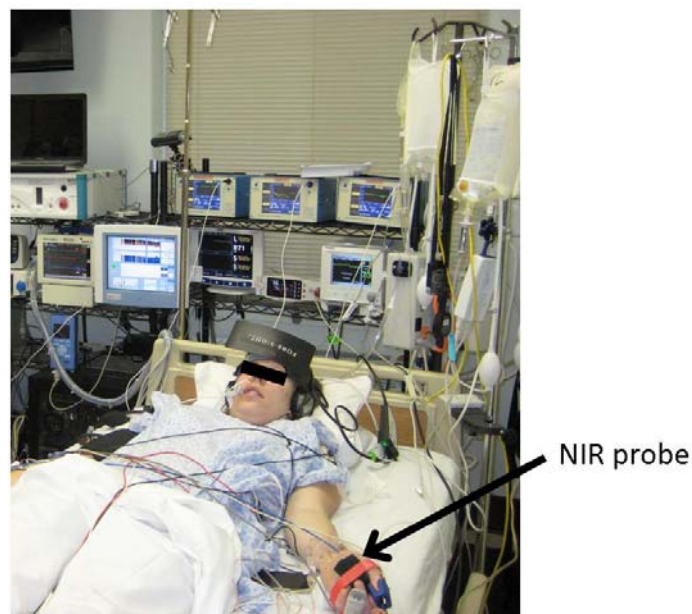


Figure 24: Photograph showing the setup of the hypovolemia study; the arrow indicates where the NIR probe was securely taped. The probe was placed on the non-dominant hand of the volunteer, because a blood pressure cuff was used on the dominant hand. Also visible in this photograph are the other noninvasive instruments used (back wall), two of the finger monitors, and a NIR forehead probe.

The probe was secured firmly with tape and stayed in place throughout the entire study. During the study, the subject underwent a series of three blood draws, or hemorrhages, and subsequent retransfusion. The total amount drawn was 25% of the total body volume of blood.

The total blood volume was estimated assuming the human body has blood concentration of 70 mL/kg. The volume per hemorrhage was then calculated such that 25% total blood volume would be taken, and then the mass of the blood was calculated using the density of blood, 1.05 g/mL. For each hemorrhage, a blood bag was placed on the scale and blood was withdrawn until the appropriate weight was reached.

The study design (Figure 25) involved nine clinical data points (CDP) and five ABG measurements.

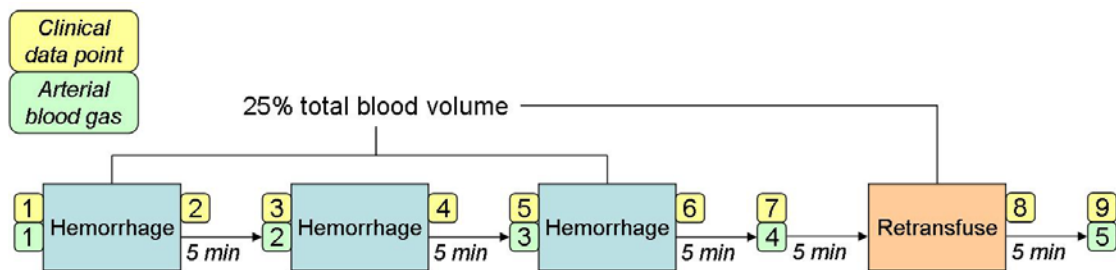


Figure 25: Timeline illustrating when each clinical data point (yellow box) and arterial blood gas (green box) were taken. 25% of the total blood volume was withdrawn over the course of three hemorrhages, indicated by the blue boxes. For the retransfusion, all withdrawn blood was returned to the body, indicated by the pink box. There were a total of nine CDPs and five ABGs. For each of the ABGs, a CDP was taken. CDPs were also taken after each of the three hemorrhages and at the end of retransfusion.

The CDPs were taken at baseline (first ABG), after the first hemorrhage, during the second ABG, after the second hemorrhage, during the third ABG, after the third hemorrhage, during the fourth ABG, after retransfusion, and during the fifth ABG. Each ABG following a hemorrhage was drawn five minutes after completion of the hemorrhage. The retransfusion was commenced 10 minutes after the completion of the last hemorrhage. For the retransfusion, all the blood that was withdrawn from the hemorrhage was returned to the subject, and the final ABG was drawn five minutes after the retransfusion was completed. The time between hemorrhage or retransfusion and ABG was shortened if the patient was having complications from the blood loss. Optical measurements were taken at each of these data points as well as approximately every five minutes.

Table 13 shows gender, age, body mass index (BMI), number of arterial blood gas measurements (ABG), and range of hemoglobin as determined from the ABG for each of the subjects. Out of all subjects, Subject #6 had the lowest range of ABG values (0.5 g/dl), and Subject #15 had the highest range (2.4 g/dl).

Table 13: Volunteer demographics and number and range of hemoglobin (Hgb) obtained from the ABG. The average age was 24.7 ± 4 years, and the average BMI was 23.4 ± 3 . The study was designed to have five ABG measurements, but for some subjects, the study had to be cut short due to complications with the status of the volunteer. For three of the subjects*, the fourth ABG was taken immediately following the end of the third hemorrhage. For three other subjects, only four ABG measurements were made.

| Subject | Gender | Age | BMI | # ABG | % drawn | Hgb range (g/dl) |
|---------|--------|-----|------|-------|---------|------------------|
| 1 | Male | 23 | 23.2 | 5 | 25 | 14.5-15.5 |
| 2 | Male | 23 | 19.3 | 4 | 16.7 | 14.8-15.7 |
| 3 | Male | 26 | 20.4 | 5 | 25 | 14.1-15.3 |
| 4 | Male | 21 | 22.5 | 5 | 25 | 14.2-14.8 |
| 5 | Male | 25 | 20.6 | 5 | 25 | 12.9-14.0 |
| 6 | Male | 28 | 24.4 | 5 | 25 | 14.6-15.1 |
| 7 | Male | 25 | 23.6 | 5 | 25 | 14.4-15.7 |
| 8 | Male | 23 | 25.1 | 5 | 25 | 12.0-12.6 |
| 9 | Male | 31 | 23.2 | 5* | 25 | 13.6-14.7 |
| 10 | Female | 20 | 21.8 | 4 | 25 | 11.4-12.2 |
| 11 | Male | 35 | 29.4 | 5 | 25 | 14.7-15.7 |
| 12 | Female | 25 | 25.7 | 5* | 20.8 | 13.1-15.0 |
| 13 | Female | 19 | 24.8 | 5* | 17.6 | 10.5-12.9 |
| 14 | Female | 27 | 20.8 | 5 | 25 | 10.8-12.4 |
| 15 | Female | 19 | 25.7 | 4 | 16.7 | 11.9-13.1 |

Three of the subjects only had four of the five ABG draws taken. For Subject #2, the third ABG was taken immediately following the second hemorrhage, and then the retransfusion was directly started, because the patient was feeling uncomfortable. For Subject #10, because a low volume constituted 25% of her total blood volume, the entire 25% was removed in only two hemorrhages. For Subject #15, the third hemorrhage was skipped because she began to feel lightheaded. The third ABG was still taken five minutes after the hemorrhage, but the retransfusion started immediately after that ABG was drawn. Thus, for these three subjects, the fourth ABG draw was not taken.

There were also some discrepancies in the timing between hemorrhages and ABG draws. For Subject #9, all three hemorrhages were completed, but because the subject was

hypotensive, the retransfusion started immediately after the third hemorrhage ended. The fourth ABG was drawn, but it was done so immediately following the hemorrhage. For Subject #12, the patient began to feel hypotensive during the third hemorrhage, and so that hemorrhage was stopped at approximately one-half the total that should have been drawn, and the fourth ABG was drawn immediately afterwards. For Subject #13, because the subject began to feel bad, the third hemorrhage was discontinued when it was about one-fourth the way through, and the fourth ABG was taken immediately afterwards followed by the beginning of retransfusion.

5.2.2 Optical Measurements

Diffuse reflectance measurements were taken using the FD system, which was described in “1.10 Ratiometric Method to Estimate Hemoglobin.” The system was coupled to a side-firing optical probe, described in [22]. Briefly, the probe consisted of two illumination fibers at separations of 5 and 10 mm from a single collection fiber. The source fibers were 200 μm in diameter, while the collection fiber was 600 μm . All fibers had NA of 0.22. The fibers of the side-firing probe are polished to a 45° angle and have mirrored coatings.

5.2.3 Data Analysis

The diffuse reflectance measurements were used to calculate the contributions of oxy- and deoxyhemoglobin, water, fat, and cytochrome oxidase in the tissue. The total hemoglobin and hemoglobin saturation could then be calculated from the concentrations of the two forms of hemoglobin. For the first five patients, the data was calibrated using 24 liquid phantoms containing ink as the absorber and Intralipid as the scatterer. The data from the remaining 10 patients was calibrated with a set of solid acrylic resin phantoms, consisting of graphite as the absorber and titanium dioxide as the scatterer. Our lab is transitioning from liquid to solid phantoms, as the latter are more stable over time and thus well-suited for calibration and routine validation [84]. Because of the differences in calibration procedure, the first five subjects and last ten subjects were separated for the analyses. The data was analyzed using

diffusion approximation as described in detail in [21, 22, 85]. A semi-infinite model was used, which has the following equations for amplitude attenuation, Att, and phase shift, $\Delta\phi$:

$$Att(r, \omega) = \frac{A}{4\pi D} \sqrt{REAL^2 + IMAG^2} \quad (12)$$

$$\Delta\phi(r, \omega) = k_{imag}(\omega)r_0 - \arctan\left(\frac{IMAG}{REAL}\right) \quad (13)$$

The REAL and IMAG components relate to the μ_s' , r is the source-detector separation, ω is the frequency, A is the net amplitude response of the instrument, D is the diffusion coefficient ($D=1/(3[\mu_a+\mu_s'])$), and r_0 is related to μ_s' and r [85].

The correlations between total hemoglobin measured optically and with the ABG were tested using the Pearson linear correlation test. In addition, correlations were tested between hemoglobin concentration and saturation measured with the FD system versus the other noninvasive instruments. The effects of separating the data by gender and BMI (cut-off point of 23.5) were also tested. Gender was considered, because the overall hemoglobin concentrations in males tend to be higher than for females, and BMI was considered in case there were variations in the thickness of the skin covering the palm dependent upon BMI. The data from the other noninvasive instruments was collected continuously. Rather than using exact CDP time points, that data was averaged over 30 second time periods.

5.2.4 Probe Pressure in Volunteers

The effect of probe pressure on the extracted hemoglobin concentration was tested in two volunteers. The instrumentation settings and tissue-probe interfacing were the same as in the hypovolemia study. For each volunteer, the pressure was varied from light to medium to high, determined qualitatively by the volunteer. For light pressure, the probe was taped to the hand but no additional pressure was added. For medium pressure, the volunteer applied slight pressure to the probe, and for high pressure, more pressure was applied. These steps were then repeated for the other hand. For each pressure, three optical measurements were taken

for a total of six measurements per volunteer. For the first volunteer, the left hand was measured first, and for the second volunteer, the right hand was.

5.3 Results

5.3.1 Correlations with Arterial Blood Gas Hemoglobin Concentration

The correlations of optical and ABG data points were tested for all patients combined, separated by type of calibration used for the FD data. For the subjects whose data was calibrated by the liquid phantoms, separation by gender and BMI was not considered, because all subjects were male and there were only five subjects. Figure 26 shows the hemoglobin concentration obtained optically versus the hemoglobin concentration from the ABG for these five subjects.

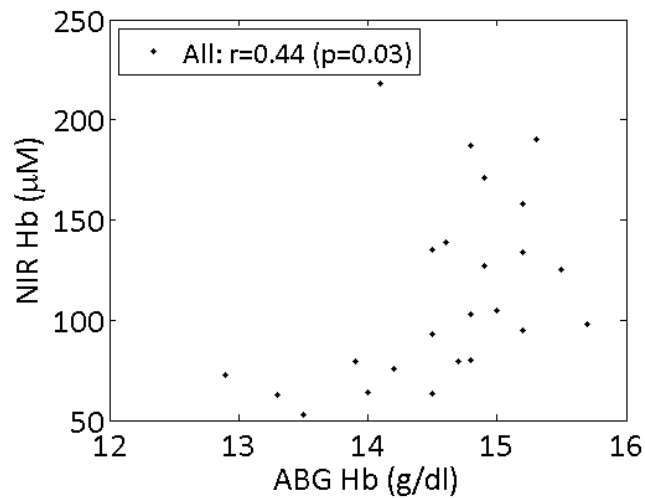


Figure 26: Total hemoglobin concentration as extracted from the optical measurements versus ABG hemoglobin for subjects 1-5. The correlation for all patients is weak but statistically significant.

For subjects 1-5, the correlation between NIR and ABG hemoglobin was significant, with $r=0.44$.

For subjects 6-15, the overall correlation between NIR and ABG hemoglobin was not significant ($r=0.18$). The effects of separating by gender and BMI were also investigated. The average BMI for subjects 6-15 was 24.5, so that was set as the cut off point for stratification.

Three of the five males and two of the five females had BMI < 24.5. The correlations for all patients and as separated by gender (top) and BMI (bottom) are shown in Figure 27.

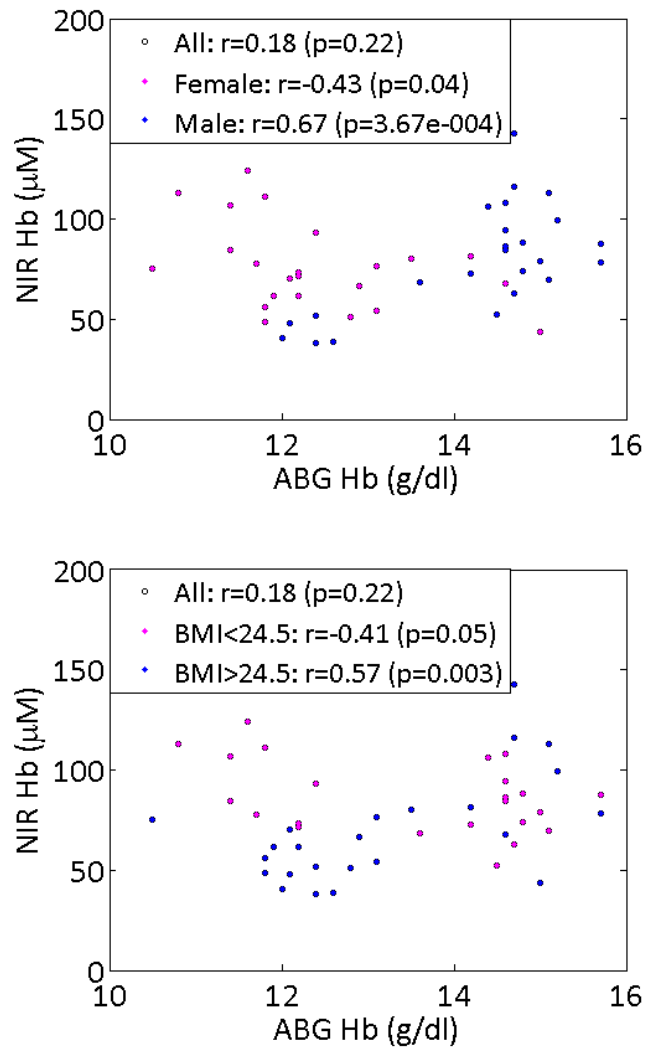


Figure 27: Total hemoglobin concentration as extracted from the optical measurements versus ABG hemoglobin for subjects 6-15, and separated by gender (top) and BMI (bottom). The correlation for all patients is not statistically significant. Interestingly, when split by gender, the female subjects actually had an inverse correlation between optical and ABG hemoglobin, while the male patients had a moderately strong positive correlation. A similar effect was seen when separated by BMI, where the lower BMI group had a strong negative correlation and the higher BMI group a stronger positive correlation.

When separated by gender and BMI, the correlations were significant but opposite, with the females and subjects with low BMI negatively correlating to ABG, but the males and subjects with high BMI positively correlating to ABG. One possible explanation for the discrepancies for

the female subjects is that out of the five females, only one completely adhered to the time line of the study design. Thus, for the remaining four females, there were differences in when the CDP and ABG measurements were taken in comparison to what is shown in Figure 25. There were fewer deviations from the study design for the males. The reason for the negative correlation for subjects with low BMI is not immediately clear.

5.3.2 Correlations with Other Noninvasive Measures of Hemoglobin Concentration

The correlations between the extracted total hemoglobin concentration measured with the FD system and two other NIR monitors were tested. Useable data was obtained from the Casmed monitor for 11 of the 15 subjects, and from the Masimo® monitor for only 8 of the subjects. Because not all patients had data measurements with these monitors, the stratification by gender and BMI was not considered here. In addition, data was not considered if the total hemoglobin concentration measured zero. The right Casmed monitor was not used on any of the female patients, so only the left monitor was considered here. The correlations between NIR and Casmed hemoglobin are shown in Figure 28 for subjects 1-5 (top) and subjects 6-15 (bottom).

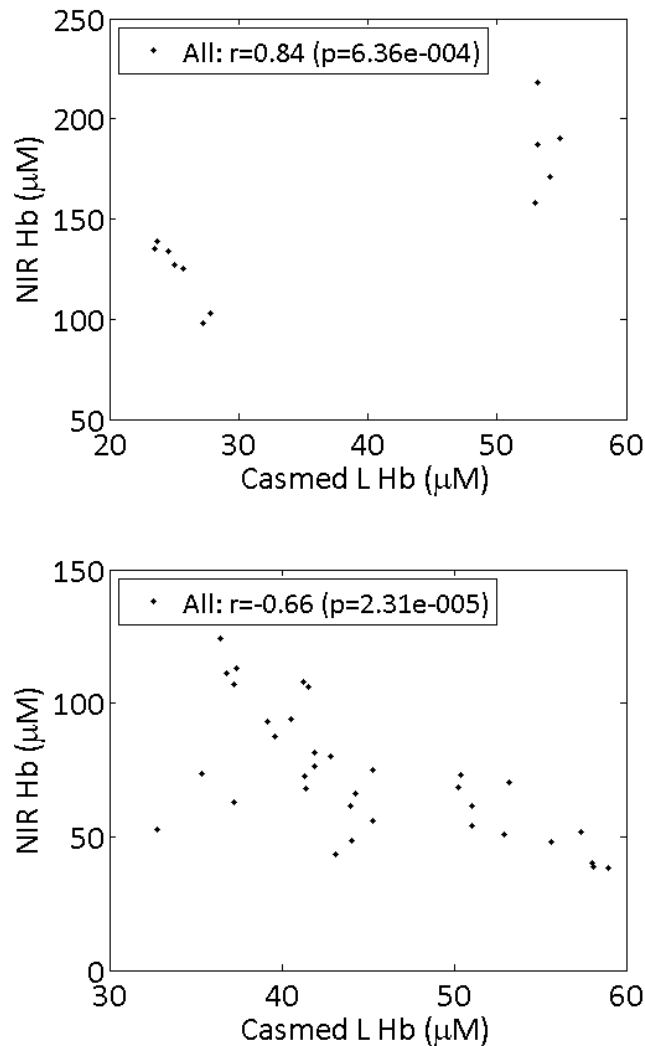


Figure 28: Correlation of NIR and Casmed hemoglobin for subjects 1-5 (top) and 6-15 (bottom). The correlations were statistically significant but in the opposite directions depending on the subject subset. The Casmed monitor was on the left finger, whereas the NIR probe was on the thenar eminence of the non-dominant hand.

The correlations for the first five subjects was significant with $r=0.84$, and for the latter ten subjects it was also significant but negatively correlated ($r=-0.66$). Again, the reason for the negative correlation is not clear.

For the Masimo device, there were only a total of 10 reliable measurements for subjects 1-5 and 11 for subjects 6-15. The correlation for those measurements to NIR

hemoglobin was $r=0.44$ and $r=-0.37$ for the first and second subset of patients, respectively, neither of which was statistically significant (data not shown).

In addition, there were not significant changes noted in the extracted optical hemoglobin concentration for just the FD instrument. Figure 29 shows the baseline-subtracted extracted hemoglobin, where for each volunteer, the first value was taken as baseline which was subtracted from all subsequent measurements. Because baseline-subtraction relies on relative measurements, all subjects could be combined for this figure.

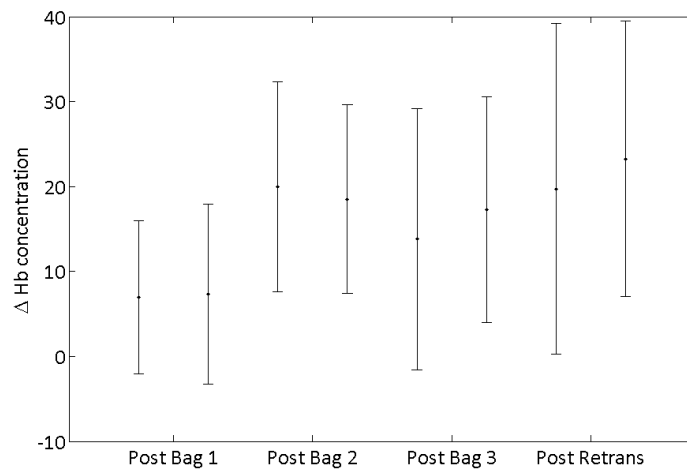


Figure 29: Baseline-subtracted concentrations averaged over all volunteers for each clinical data point. The initial point for a given time point was measured directly after the end of that perturbation, while the second point was typically five minutes later. The initial time point (baseline) was subtracted from each subsequent measurement to put all volunteers on the same relative scale.

The trend in optical hemoglobin was actually increasing as a function of increased hypovolemia, although there were not significant differences between each time point.

5.3.3 Correlations with Other Noninvasive Measures of Hemoglobin Saturation

The correlations between the extracted hemoglobin saturation measured with the NIR system and the three VIS probes were compared. Again, some of the probes were not used on all of the subjects. As such, some of the monitors compare less than the total subject

population. Because the VIS probes were mostly used on all subjects the data for all patients was combined and separations based on gender and BMI were again tested. Table 14 shows the correlations for hemoglobin saturation between the FD system and the three VIS probes, referred to by the site where the probe was placed.

Table 14: r values for correlations between hemoglobin saturation measured with the frequency-domain system and the three VIS probes. The p value is noted only if it was less than 0.05, otherwise “ns” indicates non-significance. The data was combined for all patients dependent upon the calibration method then separated based on gender and BMI for subjects 6-15. The only significant correlations were for males for the oral probe, BMI < 24.5 for the rectal probe, and BMI > 24.5 for the oral and rectal probes.

| Probe | Subj. 1-5 | Subj. 6-15 | Female | Male | BMI < 24.5 | BMI > 24.5 |
|--------|------------|------------|------------|---------------|--------------|---------------|
| Oral | 0.08 (ns) | -0.18 (ns) | 0.23 (ns) | -0.61 (0.001) | 0.09 (ns) | -0.60 (0.002) |
| Esoph. | 0.33 (ns) | 0.05 (ns) | 0.09 (ns) | -0.08 (ns) | -0.03 (ns) | -0.03 (ns) |
| Rectal | -0.22 (ns) | 0.10 (ns) | -0.10 (ns) | 0.17 (ns) | -0.43 (0.05) | 0.45 (0.03) |

There were no significant correlations when all data was combined for neither subjects 1-5 nor 6-15. When separated by gender, the oral probe had a significant negative correlation ($r=-0.61$) for males. When separated by BMI, the rectal probe had a significant negative correlation ($r=-0.43$) for BMI < 24.5, while for BMI > 24.5, the oral probe had a significant negative correlation ($r=-0.60$) but the rectal probe a significant positive correlation ($r=0.45$). Because of the lack of general correlation and the ambiguity in the direction of the correlation, these results do not seem particularly valuable.

5.3.3 Probe Pressure in Volunteers

Figure 30 shows the results for varying probe pressure in two volunteers.

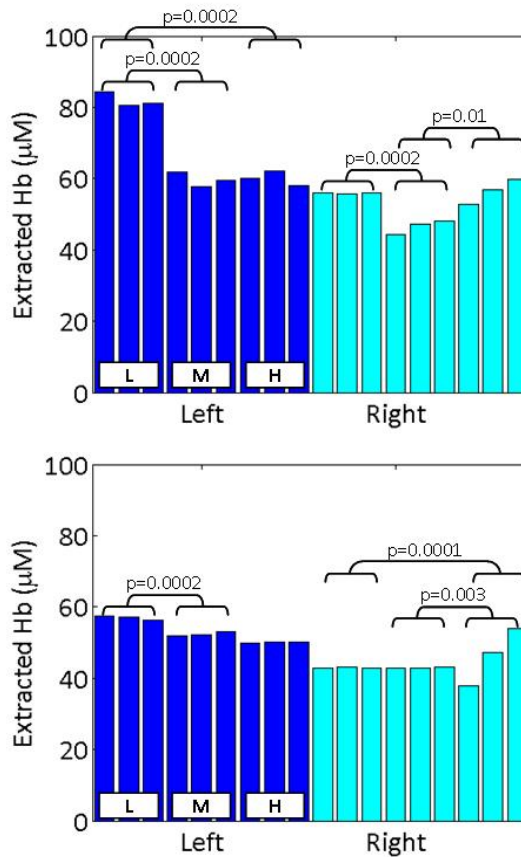


Figure 30: Diffusion approximation-extracted hemoglobin for Volunteer 1 (top) and Volunteer 2 (bottom) as a function of increasing probe pressure per site. The qualitative pressures are indicated for the first site as (L)ight, (M)edium, and (H)igh. The p values testing the statistical differences between the two measurements for any given set of pressures is shown if it was less than or equal to 0.05.

For both volunteers, there were statistically significant differences in hemoglobin concentration as a result of increased pressure. For the first volunteer, the hemoglobin concentration decreased when medium pressure was applied for both hands. For the left hand, there was also a decrease in hemoglobin from light to high pressure, while for the right hand there was an increase from medium to high pressure. For the second volunteer, there was a decrease in hemoglobin for the left site when the pressure was increased from light to medium. Additionally, there was an increase in hemoglobin with the high pressure on the right hand, compared to light and medium pressure. The discrepancy in trends may be attributed to

the time it takes for each optical measurement (close to 1 minute). Holding the probe in place at the same pressure for close to three minutes is a difficult task. In any case, this data supports the conclusion that probe pressure does affect extracted optical properties.

5.4 Discussion

In this study there were moderate correlations observed for hemoglobin concentration between the FD system and both the ABG and other noninvasive NIR monitors. However, the correlations were not consistent in whether they were negative or positive, and for some cases, there were opposing trends based on whether the data was separated by gender or BMI. The ABG measures total arterial hemoglobin, whereas the optical measurements reflect a combination of arterial and venous components at the capillary level. Again, because these methods are probing different areas, it is not even clearly understood whether or not the relationship can be expected to be linear.

The correlations between hemoglobin saturation measured with the frequency-domain system compared to the VIS probes were generally non-significant. Significance was only noted when separated by gender or BMI, and even then there were not consistencies and the direction of the correlation was variable depending upon which probe was considered. Because the frequency-domain system has not been validated for hemoglobin saturation measurements, it is not evident whether the lack of correlation is an issue of misestimation by any of the instruments or if there are just variability in the saturation measured at different organ sites. It is presumed the tissue oxygenation of the mucosal sites is more sensitive to hypovolemia than the thenar eminence, but this would need to be explored in more detail.

In addition, the CDPs for the other noninvasive points were averaged over 30 seconds of continuous measurements. If there are strong fluctuations in the hemoglobin saturation or concentration over 30 seconds, it could mask the correlations. Additionally, the FD measurements had to be separated based on the calibration method. Because of this, one

population had ten subjects and the other only five. Perhaps the data was not robust enough in sample size to see adequate correlations.

From the probe pressure data from two volunteers, a pressure-dependent effect on extracted hemoglobin concentration was observed. However, because the probe was taped to the hand during the hypovolemia study, there was not such a drastic variability in pressure as modeled in the volunteer measurements. Because of this, the pressure effect was not expected to be a significant problem for the hypovolemia measurements.

6. Development of a Ratiometric Method to Estimate Hemoglobin Concentration

6.1 Introduction

Rapid determination of hemoglobin is desirable in settings where there are large changes expected in the blood concentration. Examples of such settings include the operating room, the intensive care unit, the battlefield, and rural clinics. Because ratios can be calculated from data without post-processing, there is minimal training required for the operator. We investigated a simple ratiometric method to estimate hemoglobin concentration, independent of hemoglobin saturation and scattering, based on Monte Carlo simulations and tissue-mimicking phantoms. A large portion of this chapter comes from [9], and a patent has been submitted for this method. There are several reasons why we chose to pursue this method. For one, the ratiometric method has been shown to be less affected by probe pressure as compared to the inverse Monte Carlo method (3.3 Results). Additionally, this method essentially involves the division of diffuse reflectance at two wavelengths to predict hemoglobin concentration. Ratios at isosbestic wavelengths should theoretically be independent of hemoglobin saturation, because the extinction coefficients for oxy- and deoxyhemoglobin are the same at these points. Furthermore, this method could be further developed to be incorporated into less expensive diffuse reflectance systems, where LEDS, which have discrete wavelengths, are used as the light source [86, 87].

6.2 Methods

The goal of this study was to identify a set of isosbestic ratios that were best correlated to hemoglobin concentration independent of scattering and hemoglobin saturation. Figure 31 is a flowchart summarizing the steps taken to determine and test the best ratio(s).

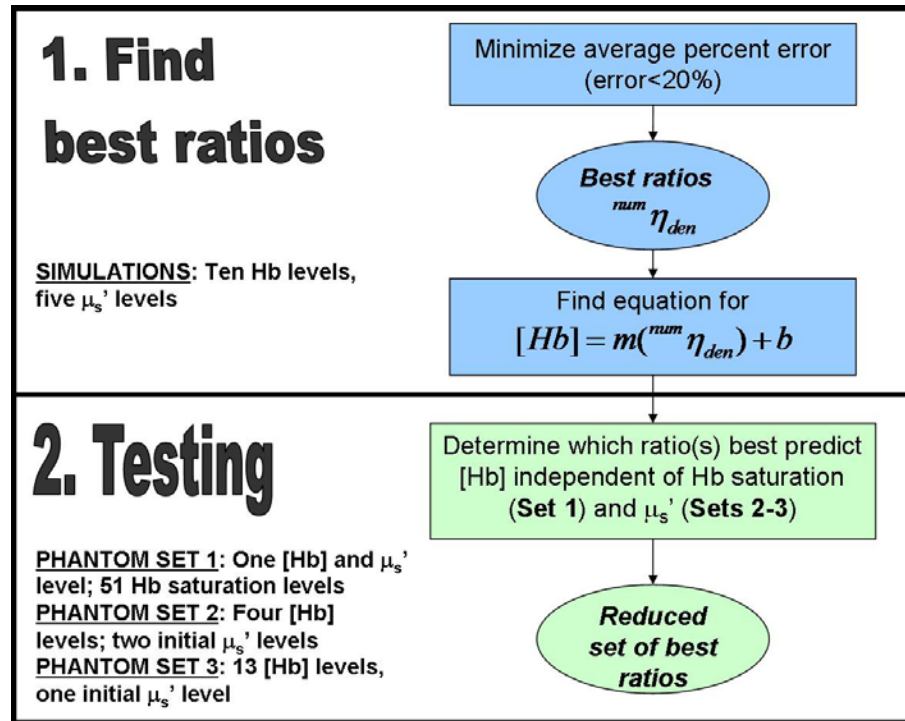


Figure 31: Flowchart summarizing steps taken to find and test the best ratios. The simulations were used to determine the first set of best ratios (${}^{num}\eta_{den}$). The linear regression equations of hemoglobin versus ratio from the simulations were directly applied to ratios from Phantom Set 1. From Set 1, a new set of best ratios was determined which were then tested with Sets 2-3.

The simulations consisted of 50 tissue models, with five scattering levels for each of ten absorption levels. Upon determining the best ratios, designated in the flow chart by ${}^{num}\eta_{den}$, where num is the numerator and den the denominator, tissue-mimicking phantoms were used to test the linear regression equations developed from the simulations. Because the testing was conducted using the linear regression equations derived directly from the simulations, no training on tissue phantoms was required. The three sets of phantoms were designed to test the independence of the ratiometric method to hemoglobin saturation (Set 1) and scattering (Sets 2-3). Phantom Set 1 contained 51 phantoms with variable hemoglobin saturation and constant hemoglobin concentration and scattering. Phantom Set 2 had four hemoglobin levels for two initial scattering levels which decreased slightly due to addition of hemoglobin. Phantom Set 3 consisted of 13 hemoglobin levels for a single initial scattering

level which decreased to a greater extent due to addition of hemoglobin. Expansions of these phantom sets were described in detail in “2.2 Methods.” A subset of ratios was tested for Phantom Sets 2 and 3, based upon the best ratio(s) from Phantom Set 1. A new set of ratios was then selected and tested on Phantom Sets 2 and 3 measured with a different instrument, to ensure this method was independent of instrument response. Upon determining the best ratio(s), the extraction ability of hemoglobin concentration was compared between this ratiometric approach and an inverse Monte Carlo model [18] developed by our group on *in vivo* diffuse reflectance measurements from cervical tissues.

6.2.1 Determination of the Best Ratios Using Monte Carlo Simulations

Forward Monte Carlo simulations [18] were conducted to determine the best isosbestic ratios of oxy- and deoxyhemoglobin that could predict hemoglobin concentration. There are eight isosbestic points for oxy- and deoxyhemoglobin over the 350-600 nm wavelength range: 390, 422, 452, 500, 529, 545, 570, and 584 nm [59]. Combinations of ten absorption and five scattering levels were used to generate optical property inputs to the 400 simulated tissue models (10 hemoglobin levels, 5 scattering levels, 8 wavelengths). The absorption levels (Table 15) corresponded to total hemoglobin concentrations of 5-50 μM with different fractions of oxy- and deoxyhemoglobin (thus different hemoglobin saturations). The μ_a at each isosbestic wavelength was determined using the molar extinction coefficients for each hemoglobin species [59].

Table 15: Concentrations of oxy- and deoxyhemoglobin used in the Monte Carlo simulations. The concentration levels were selected to range from 5-50 μM , in 5 μM increments. Although the simulations were done for isosbestic points, variable saturations were imposed for clinical relevance. The saturation was varied from 25-100%, by adjusting the relative contributions of HbO_2 and HbH .

| [Oxy-Hb] (μM) | [Deoxy-Hb] (μM) | [Total Hb] (μM) | Hb saturation (%) |
|----------------------------|------------------------------|------------------------------|-------------------|
| 2.5 | 2.5 | 5 | 50 |
| 10 | 0 | 10 | 100 |
| 10 | 5 | 15 | 66.7 |
| 5 | 15 | 20 | 25 |
| 20 | 5 | 25 | 80 |
| 15 | 15 | 30 | 50 |
| 30 | 5 | 35 | 85.7 |
| 25 | 15 | 40 | 62.5 |
| 35 | 10 | 45 | 77.8 |
| 50 | 0 | 50 | 100 |

Five different scattering levels, S1-S5 (Table 16), were combined with each of the absorption levels. The μ_s' at each of the eight isosbestic wavelengths was calculated using freely available Mie theory software [72]. For a given wavelength pair, the ratio of scattering was independent of the scattering level. The choices of absorption and scattering levels were made based on phantoms described in “2.2 Methods.”

Table 16: μ_s' for each of the five scattering levels as a function of isosbestic wavelength. The scattering levels were selected to be approximately evenly spaced by 5 cm^{-1} per level.

| Wavelength (nm) | S1 (cm^{-1}) | S2 (cm^{-1}) | S3 (cm^{-1}) | S4 (cm^{-1}) | S5 (cm^{-1}) |
|-----------------|-------------------------|-------------------------|-------------------------|-------------------------|-------------------------|
| 390 | 10.0 | 15.0 | 20.1 | 25.0 | 30.0 |
| 422 | 9.4 | 14.1 | 18.8 | 23.4 | 28.1 |
| 452 | 9.0 | 13.5 | 18.0 | 22.5 | 27.0 |
| 500 | 8.4 | 12.5 | 16.7 | 20.9 | 25.0 |
| 529 | 8.1 | 12.1 | 16.1 | 20.1 | 26.2 |
| 545 | 8.0 | 12.0 | 16.0 | 20.0 | 24.0 |
| 570 | 7.9 | 11.8 | 15.8 | 19.7 | 23.6 |
| 584 | 7.7 | 11.5 | 15.4 | 19.2 | 23.0 |

The simulations were scaled for the exact probe geometry (Probe A from “2. Assessment of the Robustness of the Inverse Monte Carlo Model”) used in the experimental measurements on which the ratios were tested. The scaling process used an image of the common end of the fiber probe and has been discussed previously [18, 23]. The approximate

spatial resolution of this probe is 1 mm, as estimated by the full-width at half maximum of the collected fraction versus source detector separation distance. The collected fraction was determined based on the fiber probe geometry as described in [18]. The average 90% sensing depth over 350-600 nm is approximately 2.2 ± 0.7 mm [55]. For all tissue models, the anisotropy factor, g , was 0.8, and the refractive indices for the fibers and tissue were at 1.45 and 1.37, respectively [55, 77]. From the forward Monte Carlo model, the diffuse reflectance was determined using a lookup table method described previously [18]. Reflectance ratios were calculated from the modeled diffuse reflectance at each isosbestic point.

Determination of the best ratio: The simulations were used to determine which ratios best correlated to hemoglobin concentration. Reflectance ratios at isosbestic wavelengths were only computed when the numerator wavelength was higher than the denominator wavelength yielding a total of 28 possible ratio combinations. The criterion for the simulation data was to minimize the goodness of fit, or the average percent error, %error, defined by:

$$\%error = 100 \cdot \frac{\sum \left| \frac{fit - Hb}{Hb} \right|}{n} \quad (14)$$

N is the number of hemoglobin levels, Hb is the concentration of hemoglobin, and fit is the linear regression equation for hemoglobin versus ratio. The errors for the simulations were determined after the ratios were averaged over all scattering levels, and the best ratios were defined as having $\%error \leq 20\%$.

6.2.2 Testing on Synthetic Tissue-Mimicking Phantoms

The efficacy of correlating isosbestic ratios to hemoglobin concentration was evaluated by testing on three independent sets of tissue-mimicking phantoms. The linear regression equations for the best ratios from the simulations were applied to the phantom data. In order to correct for the instrument dependence, the simulated reflectance was first calibrated by a correction factor determined using a single phantom from the master reference set (Table 8) to put the Monte Carlo data and the experimental data on the same scale. The calibration

phantom was from the A3-S4 level for both instruments. The calibration phantom can be measured prior to taking the laboratory or clinical measurements, and so the time taken to measure it is not relevant to the time it would take to estimate hemoglobin concentration using this ratiometric method. All diffuse reflectance data from the phantoms were divided by the spectrum of a reflectance standard measured on the same day prior to taking the ratios, so that the ratios were calculated from the true diffuse reflectance spectrum of the interrogated medium independent of lamp and/or detector response. Theoretically, correction by a reflectance standard should not be required, because the phantom also contains information about the lamp and/or detector response; this is addressed in the discussion. For the phantom measurements, the percent error was calculated by Equation 14, where the fit now refers to the extracted hemoglobin concentration using the linear regression equation from calibrated simulation data.

Figure 32 describes the procedure for finding the best ratios using the phantom data. Instrument 1 refers to the CCD-based instrument, and Instrument 2 is the PMT-based instrument.

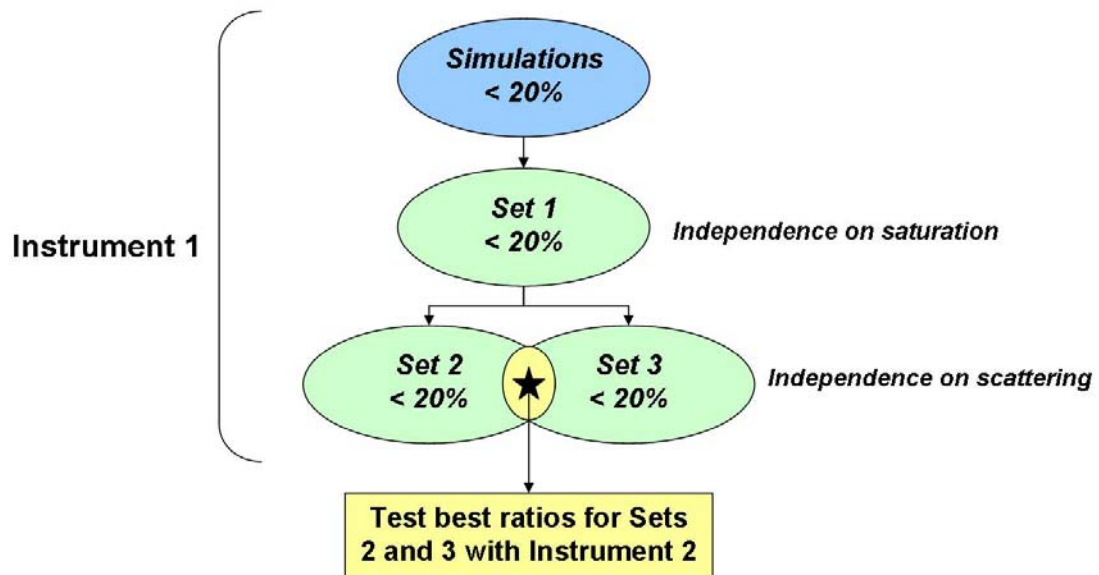


Figure 32: Expanded flowchart illustrating the steps taken for testing the best ratios from the simulations. Phantom Set 1 was used to narrow down the best ratios to be independent of hemoglobin saturation, and then Sets 2-3 were used to determine which of those ratios were independent of scattering for a larger range of hemoglobin concentrations. The ratios with %error $\leq 20\%$ common to Sets 2-3 (and also the simulations and Set 1) were then tested for phantoms measured with the PMT-based instrument.

Phantom Set 1 consisted of phantoms with variable levels of hemoglobin saturation and constant hemoglobin concentration and μ_s' . These phantoms are described in “2.2.2.3 Hemoglobin saturation phantoms;” only the phantoms measured during the desaturation process were considered in this analysis in order to keep the focus only on hemoglobin saturation. A reduced set of ratios with %error $\leq 20\%$ for Phantom Set 1 was tested by applying the regression from the simulations to Phantom Sets 2-3. Set 2 consisted of eight phantoms separated into two sets of four, where the sets referred to a lower and higher scattering level (2.2.2.1 Single absorber phantoms). For each set of four, hemoglobin concentration was increased by serial additions of stock solution. Set 3 consisted of 13 phantoms, which had increasing hemoglobin concentration for a single initial scattering level. They were similar to the phantoms described in “2.2.2.4 Hemoglobin concentration phantoms,” but the range of concentration only went up to 35 μM . For each of the sets, the addition of absorber caused a

reduction in the scattering. The best ratios were considered those for which the %error was within 20% for both Sets 2 and 3.

To test whether the ratiometric method had any instrument-dependence, the best ratios determined from the simulations and phantoms measured with the CCD-based instrument were tested with the PMT-based instrument. Again, the exact probe geometry was accounted for in the forward Monte Carlo model, and a single phantom was used to calibrate the experimental data for the instrument-dependence of the diffuse reflectance such that the diffuse reflectance from the phantoms and the forward Monte Carlo model were on the same scale. The phantom sets measured with the two instruments had similar absorption and scattering levels, but Set 2 for the PMT-based instrument was comprised of 15 phantoms covering a larger range of concentrations and thus μ_s' levels than those measured with the CCD-based instrument (as shown in “2.2.2.4 Hemoglobin concentration phantoms”). Phantoms with hemoglobin levels below 5 μM were omitted from the analysis, because the simulations only covered 5-50 μM . The illumination and collection light for both instruments was coupled to a fiber optic probe, which had the same illumination and collection geometry for both instruments (Probe A from “2. Assessment of the Robustness of the Inverse Monte Carlo Model”).

6.2.3 Sensitivity Analysis

The robustness of this method with regard to scattering slope was tested. The scattering was modeled as a power law, with $\mu_s' = a \cdot \lambda^{-b}$. For the μ_s' levels described in this paper, the value of b was approximately 0.6. Scattering slopes with values between 0.37-4 with an increment of 0.1 were tested, as those limits represent the range for particles much larger than the wavelength of light and the Rayleigh scattering regime, respectively [47, 88]. The different scattering slopes were applied to the μ_s' values in the simulations, then new linear regression equations were derived. To apply the new scattering slopes, the values for a (in $\mu_s' = a \cdot \lambda^{-b}$) were determined by fitting the original μ_s' values to a power law. Then, the new

values for μ_s' were calculated using new b values and the same a values determined from the original μ_s' values. Additionally the effect of using different values for g (0.7, 0.9, and 0.95) was tested on the results for the CCD-based instrument.

6.2.4 Clinical Applicability

The clinical applicability of isosbestic ratiometric correlations to hemoglobin concentration was tested on *in vivo* measurements of the human cervix, which have been described in a previously published paper [89]. The study protocol was reviewed and approved by the Institutional Review Board at Duke University Medical Center (DUMC). Patients referred to the DUMC Colposcopy Clinic following an abnormal Pap smear were recruited for the study. Diffuse reflectance, delivered to and collected via a fiber optic probe, was collected from one to three visually abnormal site(s) immediately following colposcopic examination of the cervix with the application of 5% acetic acid. This was followed by an optical measurement on a colposcopically normal site from the same patient. Optical interrogation of colposcopically normal and abnormal sites was conducted prior to biopsy to avoid confounding absorption due to superficial bleeding. Diffuse reflectance from 76 sites in 38 patients were normalized by a reflectance standard and interpolated prior to calculating the reflectance ratios. Scattering, absorption, and hemoglobin concentration were also extracted from the same data using the scalable inverse Monte Carlo model [18, 23]. The instrumentation used to collect diffuse reflectance *in vivo* is identical to those described in Section 6.2.2 (both the CCD- and PMT-based instruments were used).

6.3 Results

6.3.1 Determination of the Best Ratios

The optical ratios were averaged over all scattering levels for a given hemoglobin concentration in the simulations. Of the 28 total ratios, the average percent error was within 20% for 25 ratios. Figure 33 shows a histogram of the average percent errors for those 25 ratios;

four ratios had %error below 5%, nine had %error between 5-10%, seven had %error between 10-15%, and five had %error between 15-20%. For the 25 best ratios, all slopes and intercepts were statistically different from zero, as determined from linear regression t-tests.

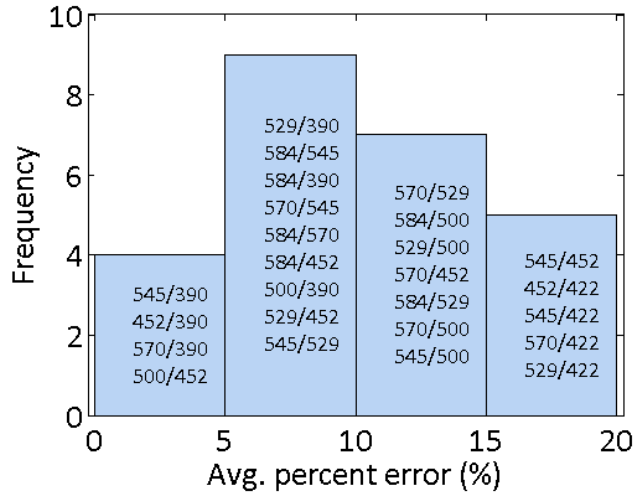


Figure 33: Histogram showing the %error from the simulations for ratios with %error within 20%. The ratios within each histogram bin are labeled on the figure in order of increasing %error (i.e. the top ratio in a given bin has the lowest relative %error).

Figure 34 shows the averaged ratios and fit for the ratio which had the lowest %error (545/390 nm).

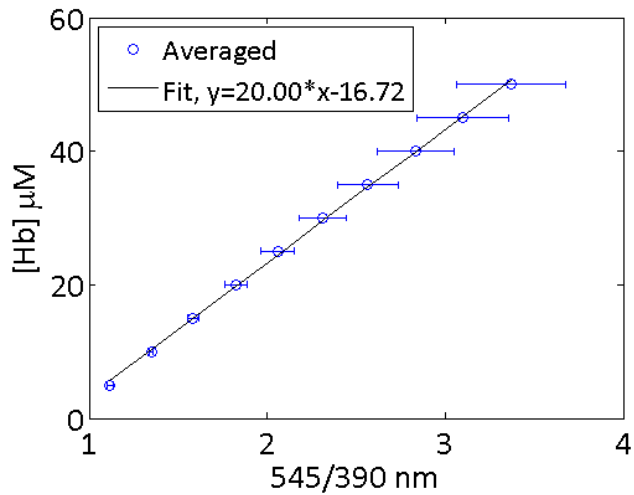


Figure 34: Hemoglobin versus averaged ratio for the 545/390 nm, which had the lowest %error of 2.3%. The error bars reflect the variation of the ratio as a function of scattering level.

6.3.2 Testing: Phantoms with Variable Hemoglobin Saturation

The ability to utilize ratiometric linear regression equations from the simulations to extract hemoglobin concentration from experimentally measured phantoms with variable saturation was tested. Figure 35 shows the average percent errors for each of the 25 best ratios from the simulations. The averages and standard deviations were taken over all 51 phantom measurements.

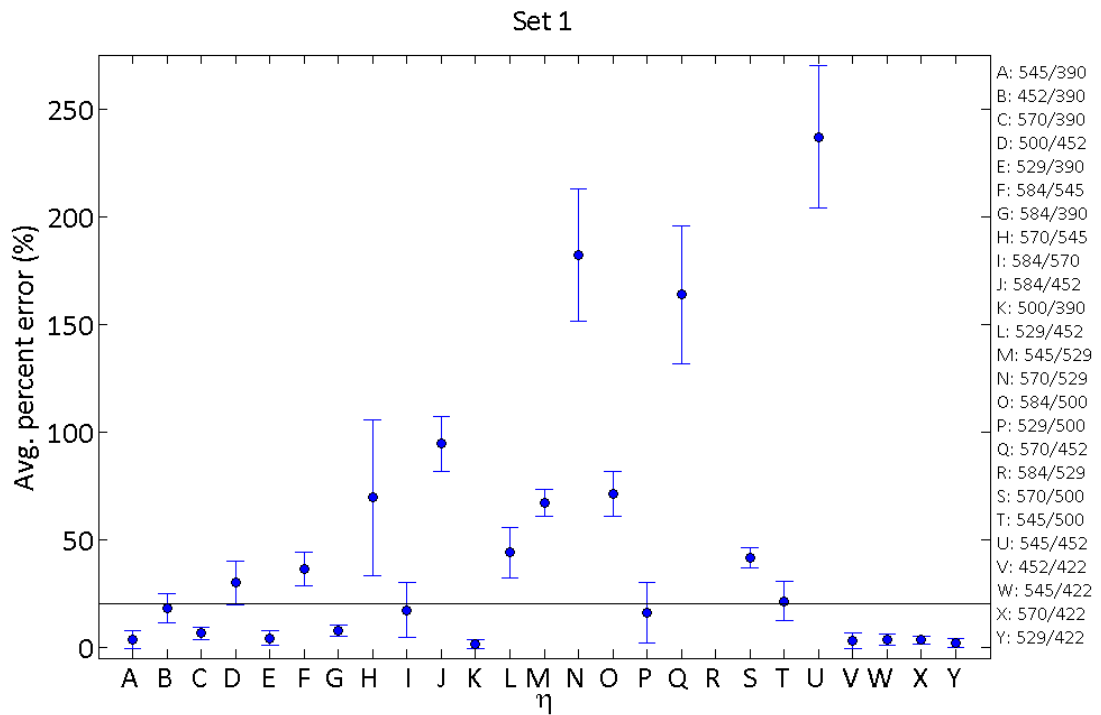


Figure 35: %error with corresponding standard deviation for Phantom Set 1 for the 25 best ratios from the simulations. The average and standard deviation were taken over the 51 phantom measurements. The black line shows the cut-off of 20% error. Of the 12 ratios under the cut-off line, only three have standard deviations stretching across 20% even though the average error is below 20% (452/390, 584/570, and 529/500 nm).

There were 12 ratios with %error \leq 20% for the hemoglobin saturation phantoms, seven of which had errors below 5%, two which had errors between 5-10%, and three of which had errors between 15-20%.

6.3.3 Testing: Phantoms with Variable Scattering and Hemoglobin Concentration

Figure 36 shows the average percent error with corresponding standard deviation for the 12 best ratios determined from Phantom Set 1. The top figure shows the results for Set 2, which had two distinct scattering levels, while the bottom figure is for Set 3, which covered a wide range of hemoglobin concentration levels for a single scattering level.

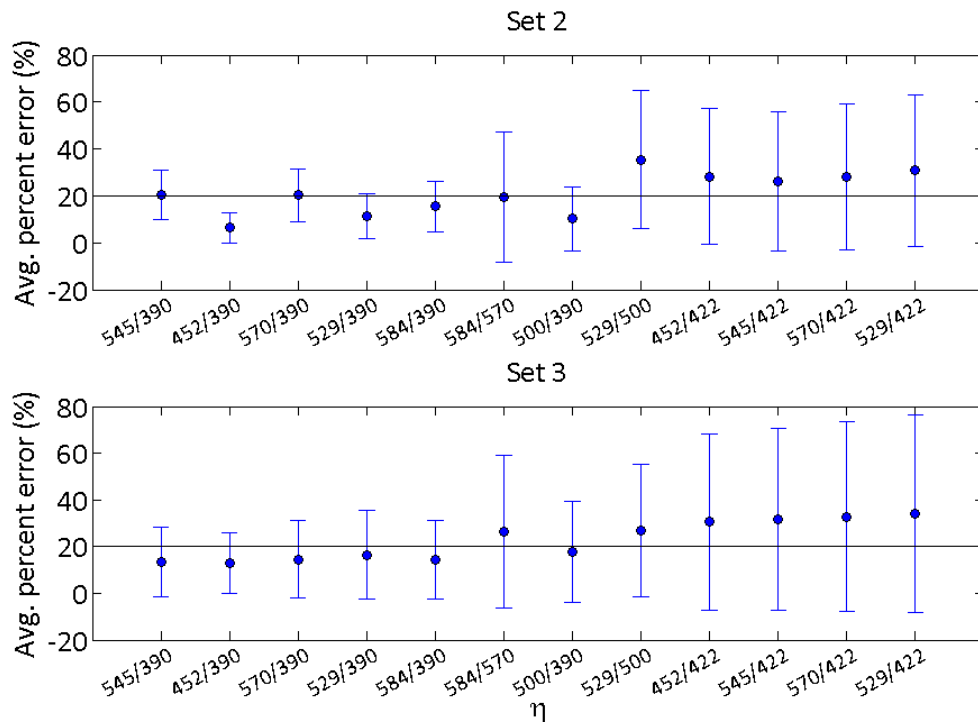


Figure 36: %error for Phantom Set 2 (top) and Phantom Set 3 (bottom) measured with the CCD-based instrument. Sets 2 and 3 were tested using the 12 best ratios from the simulations, indicated by the x-axis, which is in increasing order of %error from the simulations. The black line shows the cut-off of 20% average percent error. There were six overlapping ratios with %error \leq 20% between Sets 2 and 3.

Set 2 had seven ratios with average percent error within 20%, while Set 3 had six. Between the two sets, there were six ratios which yielded %error \leq 20%: 545/390, 452/390, 570/390, 529/390, 584/390, and 500/390. For Phantom Sets 1, 2, and 3, these were the only

six ratios that resulted in $\leq 20\%$ error for each of the phantom sets. The average percent error for 452/390 nm was below 15% for both phantom sets.

The six best ratios between Set 2 and 3 measured with the CCD-based instrument were then tested on phantom measurements using the PMT-based instrument (Figure 37). Three of the ratios had percent errors within the 20% threshold for Set 2 (545/390, 452/390, and 529/390 nm), and four did for Set 3 (545/390, 452/390, 570/390, and 529/390 nm).

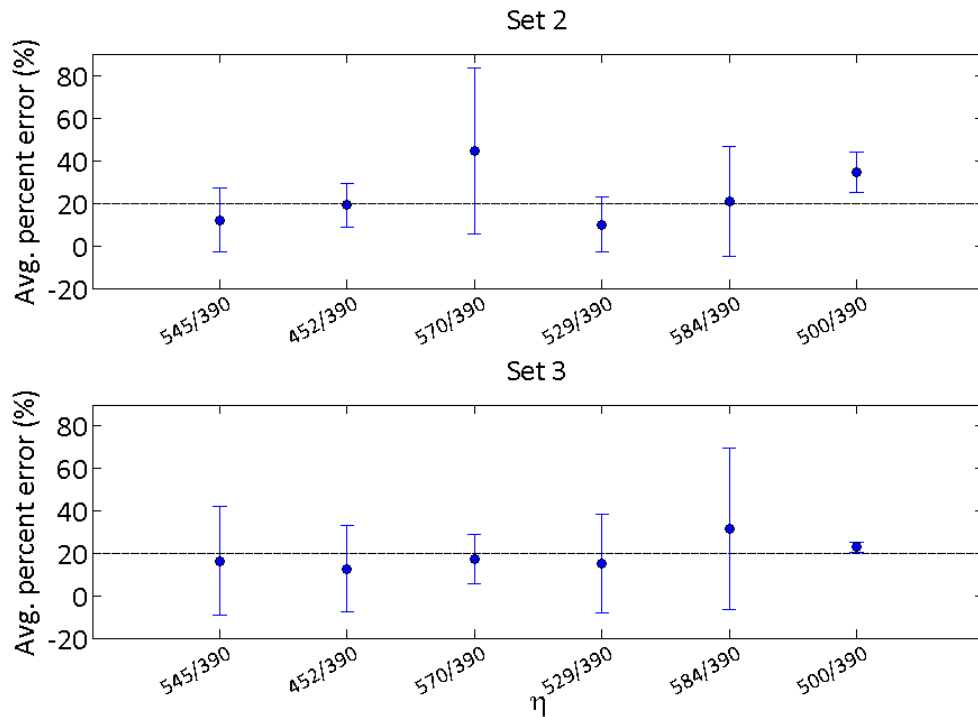


Figure 37: %error for Phantom Set 2 (top) and Phantom Set 3 (bottom) measured with the PMT-based instrument. Phantoms Sets 2 and 3 measured with the PMT-based instrument were tested using the six best ratios determined from the CCD-based instrument, indicated by the x-axis, which is in increasing order of %error from the simulations. The black line shows the cut-off of 20% average percent error. There were three overlapping ratios with %error $\leq 20\%$ between Sets 2 and 3.

Table 17 shows the average percent error for the six best ratios as determined from the CCD-based instrument and simulations for the simulations and all phantom sets.

Table 17: %error for the simulations and the three testing phantom sets. Set 1 had variable hemoglobin saturation, Set 2 had variations in hemoglobin concentration for two scattering levels, and Set 3 had large variations in hemoglobin concentration for one scattering level. Sets 2 and 3 were measured with both instruments.

| %error | | 545/390 | 452/390 | 570/390 | 529/390 | 584/390 | 500/390 |
|-------------|-------|---------|---------|---------|---------|---------|---------|
| Simulations | | 2.3 | 2.8 | 3.9 | 5.3 | 5.7 | 9.2 |
| CCD | Set 1 | 3.8 | 18.2 | 6.5 | 4.3 | 7.7 | 1.6 |
| | Set 2 | 20.4 | 6.3 | 20.3 | 11.4 | 15.5 | 10.2 |
| | Set 3 | 13.3 | 12.8 | 14.5 | 16.5 | 14.3 | 17.8 |
| PMT | Set 2 | 12.1 | 19.1 | 44.6 | 9.9 | 20.7 | 34.4 |
| | Set 3 | 16.5 | 12.7 | 17.4 | 15.2 | 31.7 | 22.8 |

The three ratios with errors below 20% for simulations and phantoms measured with both instruments (545/390, 452/390, and 529/390 nm) were applied to the diffuse reflectance measurements from human cervical tissues as described in Section 6.3.5.

6.3.4 Sensitivity Analysis

The ranges of b for which each of the six best ratios still yielded within 20% error for simulations and Sets 1-3 when measured with the CCD-based instrument are shown in Table 5. The “best ratios” here were considered ones which had resulted in $\leq 20\%$ error when they were tested on both Phantom Sets 2 and 3 measured with the CCD-based instrument. Beyond $b=0.83$, no ratios gave within 20% error. At the low end of possible scattering slopes (0.37), only 500/390 nm had errors within 20%.

Table 18: Ranges of scattering slope, b , for which the six best ratios were still considered best ratios. To still be considered a best ratio, these values of b had to result in $\leq 20\%$ error for simulations and Sets 1-3 measured with the CCD-based instrument.

| | 545/390 | 452/390 | 570/390 | 529/390 | 584/390 | 500/390 |
|-----------|----------|----------|-----------|-----------|-----------|-----------|
| b range | 0.67-0.8 | 0.57-0.8 | 0.64-0.83 | 0.55-0.78 | 0.59-0.79 | 0.37-0.68 |

When different values of g were tested, all phantom sets measured with the CCD-based instrument generally maintained %error within 20%. The average percent errors are shown in Table 6 for Sets 1-3 measured with the CCD-based instrument.

Table 19: Average percent error when $g=0.7$, 0.9 , and 0.95 were used for Sets 1-3 measured with the CCD-based instrument. The average percent error for 545/390 and 570/390 nm with Set 2 and $g=0.7$ slightly exceeded the 20% limit.

| %error | | 545/390 | 452/390 | 570/390 | 529/390 | 584/390 | 500/390 |
|--------|----------|---------|---------|---------|---------|---------|---------|
| Set 1 | $g=0.7$ | 4.8 | 16.9 | 8.4 | 3.4 | 9.5 | 2.2 |
| | $g=0.9$ | 3.5 | 19.5 | 4.6 | 5.7 | 5.8 | 1.8 |
| | $g=0.95$ | 3.5 | 19.8 | 4.0 | 6.3 | 5.1 | 2.0 |
| Set 2 | $g=0.7$ | 23.2 | 5.4 | 22.0 | 13.0 | 15.6 | 17.2 |
| | $g=0.9$ | 18.3 | 7.6 | 18.5 | 9.9 | 13.8 | 10.9 |
| | $g=0.95$ | 17.5 | 8.2 | 17.7 | 9.3 | 13.1 | 11.3 |
| Set 3 | $g=0.7$ | 12.3 | 11.8 | 13.5 | 15.6 | 13.4 | 17.2 |
| | $g=0.9$ | 14.4 | 13.8 | 15.5 | 17.4 | 15.2 | 18.4 |
| | $g=0.95$ | 14.9 | 14.2 | 16.0 | 17.8 | 15.7 | 18.7 |

6.3.5 Clinical Applicability

Data measured from an *in vivo* dysplastic cervical study [89] were used to test the correlations between ratiometrically-extracted hemoglobin and hemoglobin extracted with the inverse Monte Carlo model [18]. Briefly, a reference phantom was used to put the Monte Carlo-generated and experimentally measured data on the same scale. The Pearson linear correlations between the ratiometrically- and Monte Carlo-extracted hemoglobin were 0.75, 0.76, and 0.88 for 545/390, 452/390, and 529/390 nm, respectively. Figure 38 shows the ratio-extracted versus Monte Carlo-extracted hemoglobin for each of the three ratios for all 76 *in vivo* measurements.

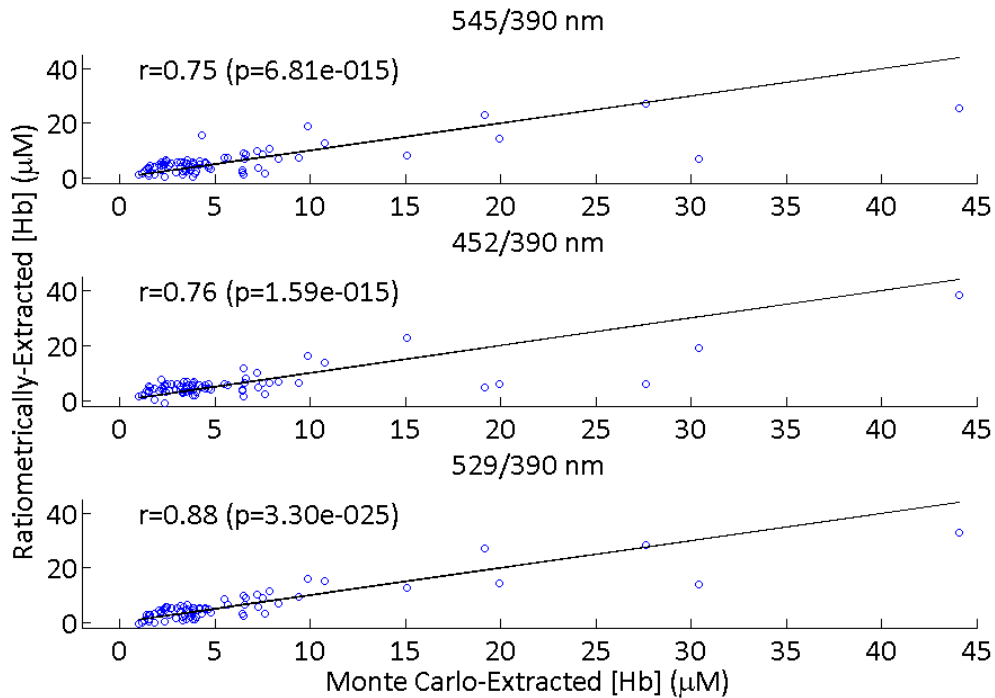


Figure 38: Monte Carlo and ratiometrically-extracted hemoglobin concentration for the three best ratios from the simulations and phantoms: 545/390 (top), 452/390 (middle), and 529/390 nm (bottom) for the *in vivo* cervical measurements. The solid line is the line of perfect agreement for the Monte Carlo-extracted hemoglobin concentration. The text in the upper left corner of each plot gives the Pearson linear correlation coefficient and corresponding p-value for the comparisons.

6.4 Discussion

We have developed an algorithm that can be used to predict the concentration of hemoglobin using simple isosbestic ratios of diffuse reflectance spectra. This algorithm employs linear regression equations from Monte Carlo simulations which were modeled for the exact probe geometry used in the experimental measurements. The linear regression equations from the simulations were determined from instrument-calibrated diffuse reflectance and could be directly applied to the experimental spectral data. Only one phantom was required to put the measured reflectance on the same scale as the Monte Carlo-generated reflectance, and this phantom only has to be measured one time for any instrument-probe combination. Based on the simulations and tissue-mimicking phantom studies, a set of three isosbestic ratios was

determined to be best correlated to hemoglobin concentration: 545/390, 452/390, and 529/390 nm. The feasibility for this method to be implemented without correction by a reflectance standard was also tested. Five of the six best ratios determined from the simulations and CCD-based instrument phantoms were retained (all except 452/390 nm). The two best ratios based on the PMT-based instrument phantoms were 545/390 and 584/390 nm. Future work will further investigate the effect of raw signal on the ratiometric data.

While the simulations showed very low errors, there were some increases in error with the phantoms. This method will be tested on additional phantom sets, because as with any laboratory experiment, there are several sources of potential errors in the preparation of phantom that can reduce the accuracy of the results. These sources of error include pipetting and ensuring the phantom and stock solutions remain thoroughly mixed.

In “3.3 Results,” we showed that the intercepts determined from linear regression of the 529/500 nm isosbestic ratio with hemoglobin concentration were similar to the ratio of scattering at the two wavelengths (i.e. $\mu_s'(529 \text{ nm}):\mu_s'(500 \text{ nm})$) [55]. For the three best ratios of 545/390, 452/390, and 529/390 nm, the corresponding ratios of μ_s' were 0.80, 0.90, and 0.80, respectively. The intercepts determined from linear regression averaged over the five scattering levels were 0.84 ± 0.07 , 0.93 ± 0.05 , and 0.72 ± 0.1 for the three ratios, respectively, indicating excellent agreement between the intercepts and μ_s' ratios for 545/390 and 452/390 nm. For 529/390 nm, when the lowest two scattering levels were omitted, the average intercept was 0.80 ± 0.06 , which indicates this ratio is more sensitive to scattering than the other two ratios. This dependence on scattering can be seen from the average percent errors shown in Figure 33.

One caveat of this method was that when hemoglobin concentration levels below 5 μM were used for the phantom testing, the errors increased (data not shown). Because the simulations had hemoglobin concentrations starting at 5 μM , the lower levels in the phantoms were omitted from the analysis. Interestingly the errors were generally lower for Set 2 versus

Set 3, even though the reference phantom was from Set 3, which shows this method is also largely independent of reference phantom.

Previous work has been focused on empirical determination of one or two ratios that could be used to grade disease, or estimate hemoglobin concentration, hemoglobin saturation, or vessel depth. Here we provide three ratios that show feasibility for predicting hemoglobin concentration in laboratory phantom and clinical *in vivo* measurements using regression equations generated from simulated data. Any one of the three ratios can be used to predict hemoglobin concentration, which is useful in any application where rapid quantitative measurements are needed, such as in the operating room. In addition, this provides hemoglobin concentrations that are concordant with those extracted using a more sophisticated inverse Monte Carlo model. Based on the current state of this method, it can be expected to improve the time taken to estimate hemoglobin concentration by a factor of almost 2000 as compared to the inverse Monte Carlo model.

In “3.2.3.2 Ratiometric method,” 529/500 nm was shown to correlate well with hemoglobin concentration in patients undergoing surgery. In this chapter, 545/390, 452/390, and 529/390 nm were shown to correlate well to hemoglobin concentration in simulations and phantoms. There were several differences between the simulations in Chapter 3 and this chapter. For one, the Monte Carlo model was different. In Chapter 3, the exact probe geometry could not be accounted for in the Monte Carlo model, because of the multiple illumination fibers, and the simulations only covered one scattering level (similar to the lowest scattering level used here). In this chapter, a Monte Carlo model in which the exact probe geometry could be accounted for was used. In addition, the simulations were expanded to include more scattering levels. In light of these differences, the best ratio from Chapter 3 was assessed for the comparisons in this chapter, and vice versa for the surgical *in vivo* data with the three best ratios from this chapter.

For the simulations described in this chapter, 529/500 nm yielded an average percent error of 11.7% when the fit was compared to the expected hemoglobin in the simulations. For

the hemoglobin saturation phantoms, the %error was $16.1 \pm 14.2\%$. The errors were somewhat higher for the Phantom Sets 2-3, where the %errors were $35.4 \pm 29.4\%$ and $26.9 \pm 28.2\%$, respectively. This indicates there may be some dependence on scattering with the 529/500 nm ratio.

When the best ratios from this chapter were applied to data from Chapter 3, there were generally weak correlations of the ratio to ABG hemoglobin. For 545/390 nm, the Pearson linear correlation coefficients were $r=-0.28$ for raw data and $r=-0.52$ for baseline-subtracted data, for 452/390 nm the raw correlation was $r=-0.10$ and baseline-subtracted was $r=-0.11$, and for 529/390 nm, the raw correlation was $r=-0.13$ and baseline-subtracted was $r=-0.19$. The baseline-subtracted correlations for 545/390 nm were significant with $p=0.006$.

Furthermore, the effect of pressure on the best ratios from this chapter was tested on the volunteer data shown in “3.3 Results.” For 545/390 nm, there were significant differences between light and medium pressure for Right 1 ($p=0.008$) and Left 2 ($p=0.02$) for Volunteer 1 and Right 1 ($p=0.01$) for Volunteer 2. There were also significant differences for Right 1 between high and both light ($p=0.02$) and medium pressure ($p=0.04$) for Volunteer 2. For 452/390 nm, there were significant differences between light and medium pressure for Right 1 ($p=0.04$) and Left 2 ($p=0.04$) and between medium and high pressure for Right 1 ($p=0.03$) for Volunteer 1. For Volunteer 2, there were significant differences between light and high pressure for Right 1 ($p=0.02$) and Left 2 ($p=0.02$), as well as between medium and high pressure for the same two sites ($p=0.03$ for both). For 529/390 nm, there were no differences between light and medium pressure. For Volunteer 1, light and medium pressure gave significant differences for Right 1 ($p=0.005$) and Left 2 ($p=0.02$) and medium and high pressure gave significant differences for Left 1 ($p=0.003$). For Volunteer 2, only Right 1 for light and high pressure ($p=0.02$) yielded significant differences.

The discrepancies between the best ratios from Chapter 3 and this chapter are not immediately clear. Because only one scattering level was tested in Chapter 3, the effect of

scattering on 529/500 nm was not made evident. Part of these ambiguities could also be attributed to issues with probe-tissue or probe-reflectance standard coupling in the surgery study from Chapter 3. The probe did not always maintain the same positioning or pressure during an individual patient’s measurements, and so this could have caused some degradation of the consistency of the reflectance spectra. The reflectance standard was measured with the lights on, and so depending on which operating room we were in, there could have been differences in the light contamination in the spectra. In addition, the hemoglobin measurements from the ABG may not be expected to correlate linearly with the ratiometric measurements from the optical data. Therefore, the efficacy of these ratios in estimating hemoglobin concentration during surgery would have to be explored in a more robust clinical study with a better gold standard measurement of hemoglobin taken at the site where the optical measurements are probing.

Table 20 shows some potential applications where the ratiometric isosbestic method could be used.

Table 20: Applications of the ratiometric isosbestic method, which can provide rapid measurements of hemoglobin concentration independent of hemoglobin saturation and scattering.

| | |
|---------------------|---|
| Applications | <ul style="list-style-type: none"> • To measure blood loss and guide transfusions in the operating room, emergency room, or the battlefield • To screen for anemia in the clinic or in rural settings • As a surrogate indicator for neovascularization <ul style="list-style-type: none"> ○ Disease prognosis ○ Disease staging ○ Response to therapy |
|---------------------|---|

7. Conclusions and Future Directions

7.1 Conclusions

This dissertation explored different diffuse reflectance implementations (wavelengths, instrumentation, and method of analysis) for the quantification of hemoglobin concentration *in vivo*. The wavelength ranges assessed were UV-VIS and NIR, the instrumentation varied between steady-state and frequency-domain devices, and the methods of analysis tested were an inverse Monte Carlo model, diffusion approximation, and a ratiometric method using isosbestic wavelengths. The Monte Carlo model and diffusion approximation methods have been previously developed, but the ratiometric method was developed during the course of the research included in this dissertation.

First, the robustness of the inverse Monte Carlo algorithm with UV-VIS wavelengths and steady-state instruments was tested using tissue-mimicking phantoms (Chapter 2). A set of “master reference phantoms” was established, which yielded less than 10% error for both absorption and scattering over a large range of optical properties. In addition, excellent quantitative accuracy was established for extracting hemoglobin saturation and hemoglobin concentration over large ranges. The ability to extract concentrations of different absorbers (hemoglobin and crocin) when they were contained separately as well as in combination, was very good. Some of the limitations of this implementation included the ability to extract μ_s' when the reference and target phantoms were measured on a different day. Also, from these studies, the bandpass of the instrument was shown to be important: a 10 nm bandpass was too wide to properly capture the spectral features of hemoglobin and achieve as accurate of absorption estimates as was encountered with a 1.9 or 5 nm bandpass.

Having shown accuracy in the laboratory for measuring hemoglobin concentration using a specific set of reference phantoms, clinical *in vivo* measurements in patients undergoing surgery were evaluated (Chapter 3). Because UV-VIS wavelengths were used, which is where the absorption of hemoglobin is high, a mucosal site where the vasculature was close to the

surface was chosen: the sublingual tissue of the mouth. For this study, 10 patients undergoing surgeries where a large degree of blood loss was expected were evaluated. Diffuse reflectance measurements were taken approximately every 15 minutes and every time blood draws were warranted according to the standard of care. The Monte Carlo results from this study did not yield excellent correlations of extracted hemoglobin concentration with systemic concentration as measured with a blood draw, and so a simple ratiometric method was tested. For the ratiometric method, all wavelength combinations from 350-600 nm were tested as simple correlates to hemoglobin concentration. Emphasis was placed on the isosbestic wavelengths of hemoglobin, where the molar extinction coefficient of oxy- and deoxyhemoglobin are equal, thus yielding independence to hemoglobin saturation. The results from this study indicated the 529/500 nm ratio was a better correlate of hemoglobin concentration than were the Monte Carlo-extracted values. The Monte Carlo algorithm depends on correction of the reference phantom and target measurement by a reflectance standard, and inconsistencies of the way these standards were measured was expected to contribute to the errors in the Monte Carlo extracted values.

Chapter 4 discussed the quantitative accuracy of diffuse reflectance measurements of NIR wavelengths using the inverse Monte Carlo model coupled with a steady-state instrument. NIR wavelengths were tested, so that the probe positioning could be more secure: hemoglobin absorption is lower in the NIR versus the UV-VIS, and so tissue sites with overlying skin can be used. The ability to position a probe on a skin-covered surface is much easier than on a mucosal surface. To test the feasibility of the inverse Monte Carlo model with NIR wavelengths, extracted phantom optical properties (from phantoms measured in the UV-VIS) were extrapolated to the NIR, then a lookup table was used to generate the corresponding reflectance. These generated spectra were used to show the theoretical feasibility of this method and wavelength combination. Next, the feasibility was tested in laboratory studies, via measurements of phantom diffuse reflectance using a portable system capable of measurements from the VIS to NIR. This combination of inverse Monte Carlo with steady-state

instrumentation suffered from errors in extracted μ_a and μ_s' when the reference and target phantoms were measured on different days. The errors for different day reference-target combinations using a frequency-domain system and diffusion approximation were much lower, and so this implementation was used for further studies using NIR measurements.

Chapter 5 discussed a volunteer study which involved measurements of the thenar eminence using NIR diffuse reflectance with a frequency-domain and diffusion approximation implementation. Here, the degree of blood loss was highly controlled. For this study, 15 volunteers were recruited. Each volunteer had 25% of their total blood withdrawn (typically into three separate bags, depending on the total blood volume) then subsequently replaced. Optical measurements were taken approximately every five minutes and during each systemic blood draw. Systemic blood draws were taken at baseline, three times corresponding to the end of each blood draw, and one time after all the blood was retransfused, for a maximum total of five ABG measurements. Taken concurrently to the measurements with the frequency-domain instrument were measurements of hemoglobin saturation or concentration from other noninvasive monitors. The results from this study indicated the extracted concentration of hemoglobin did not correlate strongly to the systemic hemoglobin. There are several explanations for this: first, the systemic hemoglobin measures arterial blood alone, whereas the optical measurements are a volume-averaged capillary measurement. Secondly, even though the degree of blood loss was stringently controlled in this study, a healthy body is able to restore hemoglobin upon loss, and so the overall variation in hemoglobin concentration was minimal. There were no systematic correlations in hemoglobin concentration or saturation between the frequency-domain instrument and other noninvasive monitors. For concentration comparisons, two other NIR-based monitors were used on the fingertips, and for saturation comparisons, VIS-based probed were placed in the mouth, esophagus, and rectum. The lack of consistent correlations may be due to the variability in probe positioning and the study design in general.

Chapter 6 detailed the development and preliminary validation of the empirical ratiometric isosbestic method for quantification of hemoglobin concentration. This method was shown in Chapter 3 to outperform the inverse Monte Carlo model for *in vivo* quantification and it indicated a lower dependence on the pressure-induced effects on extracted optical values. This chapter included Monte Carlo simulations to develop linear regression equations between total hemoglobin and isosbestic ratios that could be directly applied to experimental measurements. A forward Monte Carlo model was used, which enabled scaling for the instrument and probe geometry used for the experimental measurements. From these studies, the quantitative accuracy in extracting hemoglobin concentration was shown to be best with a set of three isosbestic ratios: 545/390, 452/390, and 529/390 nm. The best ratios were determined from both the simulations and phantom measurements using two different steady-state instruments. Upon determining the best ratios, they were applied to measurements taken *in vivo* from the cervix. The correlations between the ratiometrically-extracted hemoglobin concentration and the concentration extracted from the inverse Monte Carlo model were strong, indicating the robustness of this ratiometric method.

7.2 Future Directions

The work described in this dissertation provides groundwork for future studies performed using steady-state diffuse reflectance spectroscopy to noninvasively estimate hemoglobin concentration. The selection of UV-VIS or NIR wavelengths is largely dependent upon the organ site being interrogated.

UV-VIS wavelengths: UV-VIS wavelengths are suitable for biological sites where the vasculature is close to the tissue surface. The inverse Monte Carlo model performs well in extracting hemoglobin concentration and scattering in phantoms, but there still remains some misestimation of tissue hemoglobin as compared to systemic hemoglobin. In addition, the quantification of scattering using different-day reference-target phantoms still indicates some error, presumably due to the process by which the lamp is corrected for between days. Our lab

is currently developing a system that has the capability for self-calibration which should help mitigate the issues of misestimation of scattering [90].

By using a simple ratiometric method involving ratios of isosbestic points for hemoglobin, the correlations to total hemoglobin have been shown to be improved over the inverse Monte Carlo model for *in vivo* measurements. Because the ratiometric method does not require extensive calibration, it can be used rapidly to estimate hemoglobin. One drawback of the ratiometric method is that it cannot be used to measure tissue scattering in its current state. Further investigation would be required to find ratiometric correlates that could estimate scattering. However, for the purposes of rapid hemoglobin estimates, the ratiometric technique shows great promise.

Additionally, because this method uses discrete wavelengths, it serves as a framework towards future endeavors involving the transition to more portable systems using light-emitting diodes (LED) [86]. LEDs are advantageous as they are cheaper and allow for more compact and thus portable packaging. In addition, improvements to the probe-tissue interfacing methods must be explored to ensure better security. A side-firing probe that could be used with the steady-state system would be one option that would allow for ratiometric measurements and better probe security.

NIR wavelengths: NIR wavelengths can be used to probe deeper into the tissue thus enabling probe-based measurements from tissue surfaces with overlying skin or where the vascular is further from the tissue surface. The inverse Monte Carlo model was shown to suffer from the same errors in estimation for scattering as was shown for the UV-VIS wavelengths. Simulations indicated the extraction of μ_a and μ_s' should be feasible with Monte Carlo, so it is assumed there are some instrument-dependent factors prohibiting accurate estimates. Future studies in our lab will investigate the self-calibration probe in the NIR with instrumentation more tailored towards NIR measurements. Results from the *in vivo* study measuring subjects undergoing induced hypovolemia showed there was a discrepancy between optically and

arterially measured hemoglobin. In this application and other applications using diffuse reflectance spectroscopy, the optically measured hemoglobin is not a perfect correlate to systemic hemoglobin unless the diffuse reflectance measurements are taken where the blood supply is curtailed.

Future studies will explore more robust probe positioning. One option would be to have a probe adaptor that houses the probe and can be secured directly to the site, such as the cheek. Another option would be to measure directly from organ sites where blood supply is most crucial, such as the gut. By suturing the probe directly to the organ during surgeries, it is predicted the optical measurements would more closely describe organ status. Because the probe system is measuring a volume-averaged tissue space, the measurement of acute changes in blood delivery to capillary beds would essentially be a direct measure. Studies have shown there to be a decrease in patient outcome with a decrease in gut perfusion during surgery [91]. Using optical spectroscopy intraoperatively could potentially give real-time measurements of gut perfusion. Furthermore, areas where the least fluctuations in temperature are expected to occur, such as the head, axilla, or groin, could be explored as potential sites for probe placement.

In addition, the methods described in this thesis could be used to measure blood loss during cardiopulmonary bypass surgery, an application where pulse oximetry is not useable, due to the non-pulsatile blood flow introduced by the heart-lung bypass machine. In addition, this technology could be implemented in the assessment of the watershed blood distribution in the brain during surgery. The watershed areas in the brain are located at the most distal ends of the arteries, and thus poor perfusion can strongly impact these areas. The ability to measure the perfusion in the watershed area could perhaps decrease morbidity.

Appendix A: Neutron Stimulated Emission Computed Tomography for the Diagnosis of Breast Cancer

A.1 Introduction

Neutron Stimulated Emission Computed Tomography (NSECT) is a relatively new technique pioneered by the late Dr. Carey E. Floyd that can non-invasively image the elemental composition of tissues within the human body [92-95]. NSECT is based on inelastic scattering of high-energy fast neutrons (2.5-5 MeV), where upon being bombarded by a neutron, the atomic nucleus reaches an excited state. The nucleus then emits a gamma ray, with energy characteristic of the atomic nucleus with which it interacted. By analyzing the energy levels of the emitted gammas when a sample is bombarded with neutrons, the elemental composition of a sample can be determined.

Many studies have shown there to be a difference in the composition of trace elements of normal, benign, and malignant tissue in humans for a large variety of cancers, including breast cancer [96-99]. To determine compositional differences, these studies have required invasive methods, such as biopsy. The NSECT technique has the potential to measure these differences non-invasively, *in vivo*, with a reduced dose compared to four-view screening mammography [92], indicating NSECT has the potential to evolve into a powerful, low-dose screening or diagnostic technology for breast cancer .

We present NSECT as an imaging modality that has the potential to be translated to the clinic, due to its noninvasive nature. The work discussed in this appendix is largely drawn from [92]. This study incorporates Monte Carlo simulations and Receiver Operating Characteristic (ROC) analysis to investigate the performance of different elements in differentiating malignant and normal breast tissue at appreciably low dose levels. This study is restricted to single projection spectra of models of bulk breast tissue to investigate the feasibility of NSECT in trace element quantification to detect breast cancer.

A.2 Methods

A.2.1 Simulations

Monte Carlo simulations were designed using Geant4 software. Bulk breast tissue was modeled as an ellipsoid 10 cm x 6 cm x 5 cm. The detector elements were two high-purity germanium (HPGe) detectors, modeled as 12 cm diameter x 5 cm height cylinders of 5.32 g/cm³ density germanium. The two detectors flanked the breast tissue and were separated by 11.6 cm. The neutron source was modeled in Geant4 as a fast neutron (2.5 MeV) beam of 1 cm² area with a square profile, which was directed incident upon bulk breast tissue. A pictorial representation of the Geant4 environment is shown in Figure 39.

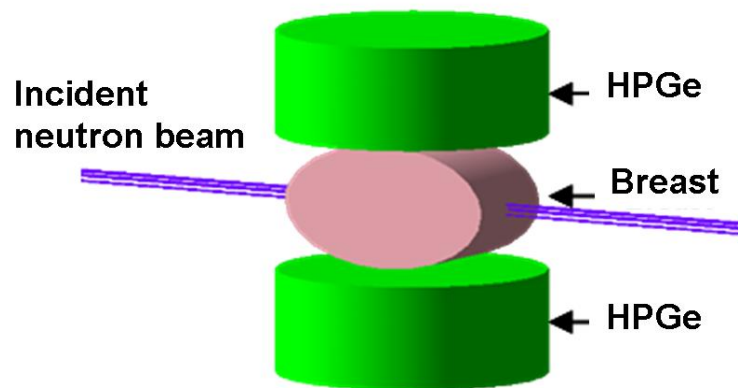


Figure 39: Orientation of the bulk breast tissue and surrounded HPGe detectors used in the Monte Carlo simulations. Incoming neutrons strike the face of the breast tissue. The Geant4 software allows the user to modify the positioning and elemental construction of all elements in the simulation environment. The software also has the capability for the user to visualize the Monte Carlo processes or simply collect the data.

The Geant4 code involves random sampling to determine the direction of the emitted gamma, which may get deposited in one of the two gamma detectors. The gamma ray energy deposited in each detector was tabulated to form a gamma spectrum showing energy levels and corresponding gamma counts. The energy levels were then matched to an element, using a look-up table from the Evaluated Nuclear Data Files (ENDF) database [100].

Breast tissue was modeled as either being normal or malignant, with elemental compositions defined based on values in the literature [101]. The normal breast tissue was modeled with a density corresponding to adipose tissue (0.93 g/cm^3), and the malignant breast tissue was modeled with a density corresponding to masses (1.058 g/cm^3) [102]. The 2.5 MeV neutron energy was selected to be low enough to avoid excitation of oxygen, carbon, and nitrogen, which along with hydrogen constitute over 99% of the breast elemental composition, and high enough to excite the trace elements, which were the targets of interest. Table 21 shows the composition of elements in normal and malignant breast tissue [101].

Table 21: Percent composition of the four major elements and twelve primary trace elements in normal and malignant breast tissue. The majority of the tissue is comprised of oxygen, carbon, hydrogen, and nitrogen, but by selecting a low enough incident neutron energy, the excitation of oxygen, carbon, and nitrogen could be avoided. The hydrogen peak was easily distinguishable in the spectra, and so the identification of the trace elements was not confounded by its presence.

| Element | Normal (%) | Malignant (%) |
|-----------|------------|---------------|
| Oxygen | 61.43 | 61.43 |
| Carbon | 22.86 | 22.86 |
| Hydrogen | 12.65 | 12.51 |
| Nitrogen | 2.57 | 2.57 |
| Chlorine | 1.98E-1 | 2.15E-1 |
| Sodium | 1.85E-1 | 2.00E-1 |
| Potassium | 8.94E-2 | 1.96E-1 |
| Iron | 9.80E-3 | 7.85E-3 |
| Calcium | 8.29E-3 | 1.13E-2 |
| Zinc | 1.17E-3 | 1.14E-3 |
| Bromine | 7.07E-4 | 6.55E-4 |
| Aluminum | 6.67E-4 | 5.70E-4 |
| Rubidium | 5.98E-4 | 5.84E-4 |
| Manganese | 3.88E-5 | 3.16E-5 |
| Cobalt | 2.06E-5 | 1.98E-5 |
| Cesium | 3.27E-7 | 3.60E-7 |

One hundred simulations of 10 million incident neutrons were run on both the normal and malignant models. For each simulation, a new Monte Carlo random seed was generated, which was different between the malignant and normal runs, so that the runs were uncorrelated. Additionally, 100 simulations were run for each of 0.5 million, 1 million, 2

million, 3 million, and 5 million incident neutrons. This yielded a total of 600 spectral scans per tissue type.

A.2.2 Peak-Identification Algorithm

Each Geant4 output file contained tabulated energies and corresponding gamma intensities. The spectral output contains information at every energy level, so an algorithm was developed to determine whether or not the intensity could be considered a significant peak. To be called a peak, three criteria had to be met: (1) the peak had to exceed a set minimum number of counts above the noise level (40 counts), (2) the peak had to be larger than all other peaks in a specified window, and (3) the peak energy had to match to one of the elements in the breast tissue model as determined from the ENDF database. An iterative technique was used to optimize the window width, where window widths were varied from ± 2 to ± 20 keV, and correlations between the number of detected peaks and the number of expected peaks were tested. The best results were seen for a window width of ± 10 keV. Figure 40 shows an example of the peak-identification technique for one of the simulations using 10 million incident neutrons. The circles mark the energies that fit the first two criteria, and the labels note the corresponding element if the peak fit the third criterion.

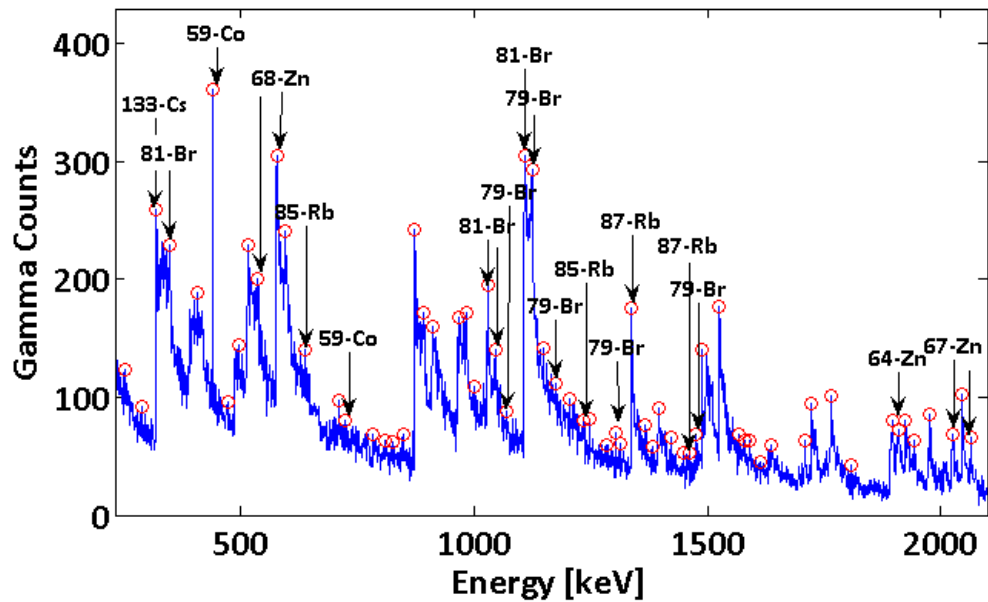


Figure 40: Peak-identification results from one of the 10 million incident neutron simulations for normal breast tissue. The red circles indicate energy levels where the number of gamma counts exceeded 40 and the peak was the highest in a ± 10 keV window, and the arrows show which of these energies matched an elemental isotope contained in the breast tissue.

A.2.3 ROC Analysis

The performance of the elemental isotopes in differentiating normal from malignant tissue was tested using the area under the binormal ROC curve, or A_z . In order to test the effect of dose, the significance of a peak at lower levels of incident neutrons was determined by monitoring the degradation in the area under the ROC curve as the number of incident neutrons was reduced. In order for a specific energy peak to be used in the ROC analysis, more than 50 of the 100 files for each case (normal or malignant) had to register the given peak from the peak identification algorithm. The purpose of this criterion was to focus only on the peaks found in the majority of each tissue model. As long as more than half of the files registered the peak, the counts for all files were entered for ROC analysis. The ROC analysis was conducted for each of the matched energies using the counts for that energy level from all 100 runs for normal and 100 runs for malignant as the input data to the software, ROCKIT, which uses

maximum likelihood estimation to fit a binormal ROC curve to continuously-distributed and/or categorical data [103]. The two possible results from the ROC analysis were “actually-negative” and “actually-positive,” which respectively correspond to normal and malignant status.

Because ROC analysis was performed on a moderately small sample size (n=200), it was expected that A_z estimates would have a relatively large variance. To ensure that the peaks selected had good discriminatory ability, we applied a minimum threshold of $A_z = 0.85$ to call an isotope significant.

A.2.4 Dose Calculations

One of the primary concerns with any prospective clinical imaging technique is the absorbed patient dose. The dose was estimated using a separate Monte Carlo simulation with the same parameters and setup as described in A.2 Methods. As the neutrons irradiated a 10 cm³ volume of tissue, corresponding to a neutron beam surface of 1 cm² over a 10 cm depth, the total irradiated mass could be calculated using the density of the breast tissue. This was then converted into the absorbed dose, $D_{T,R}$, in a tissue or organ T due to radiation R. The equivalent dose, $H_{T,R}$, was then calculated by:

$$H_{T,R} = \omega_R \cdot D_{T,R} \quad (15)$$

The radiation weighting factor, ω_R , was set to 10, the value for neutrons with energy between 2 MeV to 20 MeV [104]. The effective dose, E , to the breast tissue was calculated by:

$$E = \omega_T \cdot H_{T,R} \quad (16)$$

ω_T is the tissue weighting factor, which is equal to 0.05 for breast [105].

Using the method described above, the effective dose was estimated to be 1.12E-8 mSv/neutron.

A.3 Results

For the 100 normal tissue runs of 10 million incident neutrons, 28 energy levels were identified to be peaks in over half of the runs, and for the 100 corresponding malignant runs,

30 energy levels were designated as peaks in over half of the runs. These energy levels were queried in the ENDF tables; eight levels in the normal model and ten levels in the malignant model corresponded to elements from the breast tissue model. All eight energy peaks from the normal model were also found in the malignant model, suggesting that they robustly appear in the majority of tissue samples from each population. Table 22 summarizes the energy levels and the corresponding number of matches for normal and malignant models.

Table 22: Energy levels for the isotopes that registered in over half of the normal or malignant models using the peak identification algorithm. The last two columns show the number of simulations (out of 100 total) for which the isotope registered as a peak. For 1124 and 1697 keV, the isotopes were only identified in over half of the malignant simulations. Only one isotope, ⁵⁹Co matched in all 100 normal and malignant simulations.

| Energy (keV) | Isotope | Normal matches | Malignant matches |
|--------------|-------------------|----------------|-------------------|
| 319 | ¹³³ Cs | 98 | 90 |
| 439 | ⁵⁹ Co | 100 | 100 |
| 1029 | ⁸¹ Br | 100 | 99 |
| 1109 | ⁸¹ Br | 85 | 56 |
| 1124 | ⁷⁹ Br | 43 | 51 |
| 1191 | ⁷⁹ Br | 51 | 60 |
| 1338 | ⁸⁷ Rb | 95 | 97 |
| 1476 | ⁷⁹ Br | 79 | 61 |
| 1697 | ⁴¹ K | 49 | 54 |
| 2065 | ⁶⁷ Zn | 60 | 70 |

The peaks shown in Table 22 were further analyzed with ROC at the six different incident neutron levels to determine how well they could differentiate between normal and malignant tissue. ROC analysis on the 60 total energy level/incident neutron combinations yielded 12 total combinations with ROC $A_z > 0.85$ (Table 23). The combinations corresponded to one of five separate energy levels - 319 keV, 1029 keV, 1109 keV, 1124 keV, and 1338 keV, representing ¹³³Cs, ⁸¹Br, ⁸¹Br, ⁷⁹Br, and ⁸⁷Rb respectively. Aside from 1124 keV, all these prominent energy levels satisfied the condition of element matching in over 50 of 100 normal and malignant output files. For 1124 keV, this condition was satisfied only for the malignant tissue model. One combination - 1338 keV (⁸⁷Rb) with 10 million incident neutrons - yielded a perfect A_z value of 1.00.

Table 23: ROC A_z values for each of the 10 isotopes determined to be peaks in over half of the normal or malignant models for each of the six incident neutron levels. The gray shading indicates the isotope did not exceed the threshold of $A_z=0.85$. There were a total of five energy levels that surpassed the A_z threshold.

| keV: isotope | Millions of incident neutrons | | | | | |
|------------------------|-------------------------------|-----------------|-----------------|-----------------|-----------------|-----------------|
| | 0.5 | 1 | 2 | 3 | 5 | 10 |
| 319: ^{133}Cs | 0.68 \pm 0.04 | 0.71 \pm 0.04 | 0.79 \pm 0.03 | 0.81 \pm 0.03 | 0.88 \pm 0.02 | 0.95 \pm 0.01 |
| 439: ^{59}Co | 0.54 \pm 0.04 | 0.58 \pm 0.04 | 0.58 \pm 0.04 | 0.64 \pm 0.04 | 0.61 \pm 0.04 | 0.67 \pm 0.04 |
| 1029: ^{81}Br | 0.60 \pm 0.04 | 0.65 \pm 0.04 | 0.79 \pm 0.03 | 0.83 \pm 0.03 | 0.87 \pm 0.02 | 0.97 \pm 0.01 |
| 1109: ^{81}Br | 0.66 \pm 0.04 | 0.81 \pm 0.03 | 0.89 \pm 0.02 | 0.91 \pm 0.02 | 0.95 \pm 0.02 | 0.99 \pm 0.01 |
| 1124: ^{79}Br | 0.63 \pm 0.04 | 0.67 \pm 0.04 | 0.67 \pm 0.04 | 0.67 \pm 0.04 | 0.81 \pm 0.03 | 0.89 \pm 0.02 |
| 1191: ^{79}Br | 0.57 \pm 0.04 | 0.57 \pm 0.04 | 0.58 \pm 0.04 | 0.64 \pm 0.04 | 0.64 \pm 0.04 | 0.74 \pm 0.03 |
| 1338: ^{87}Rb | 0.64 \pm 0.04 | 0.71 \pm 0.04 | 0.81 \pm 0.03 | 0.87 \pm 0.02 | 0.93 \pm 0.02 | 1.00 |
| 1476: ^{79}Br | 0.60 \pm 0.04 | 0.67 \pm 0.04 | 0.72 \pm 0.04 | 0.75 \pm 0.03 | 0.76 \pm 0.03 | 0.85 \pm 0.03 |
| 1697: ^{41}K | 0.52 \pm 0.04 | 0.49 \pm 0.04 | 0.50 \pm 0.04 | 0.56 \pm 0.04 | 0.58 \pm 0.04 | 0.66 \pm 0.04 |
| 2065: ^{67}Zn | 0.47 \pm 0.04 | 0.54 \pm 0.04 | 0.54 \pm 0.04 | 0.58 \pm 0.04 | 0.60 \pm 0.04 | 0.66 \pm 0.04 |

Figure 41 summarizes the mean and standard deviation of the A_z values as a function of number of neutrons for all five energy levels that surpassed the A_z threshold.

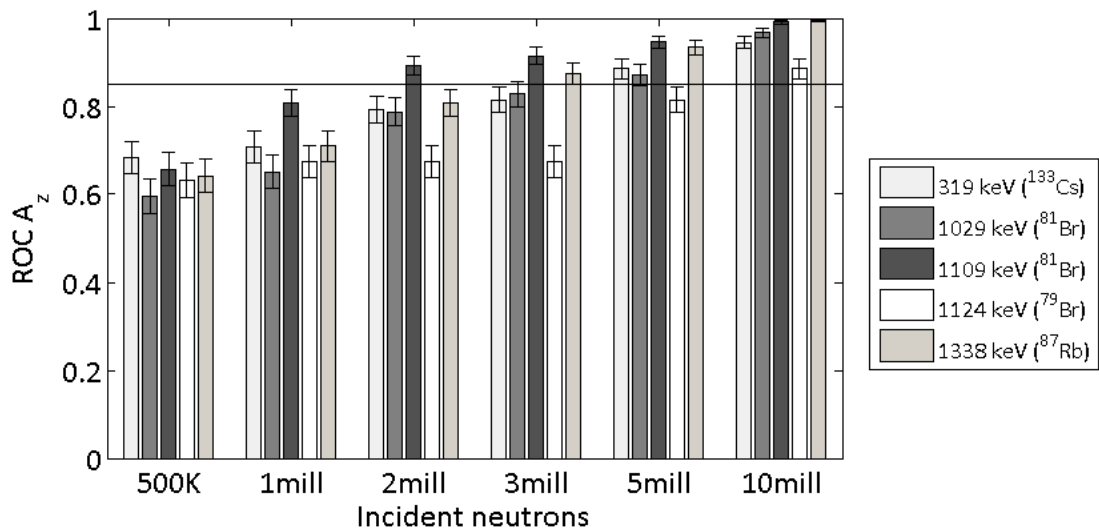


Figure 41: Average A_z values for the five prominent energy levels as a function of number of incident neutrons. The horizontal line indicates the cutoff threshold of 0.85. The lowest number of incident neutrons that could feasibly be used to differentiate malignant for normal tissue was two million, for the 1109 keV energy level.

Figure 42 shows the summation of all normal and malignant runs for 10 million incident neutrons and indicates the peaks which were found to be prominent in the ROC analysis.

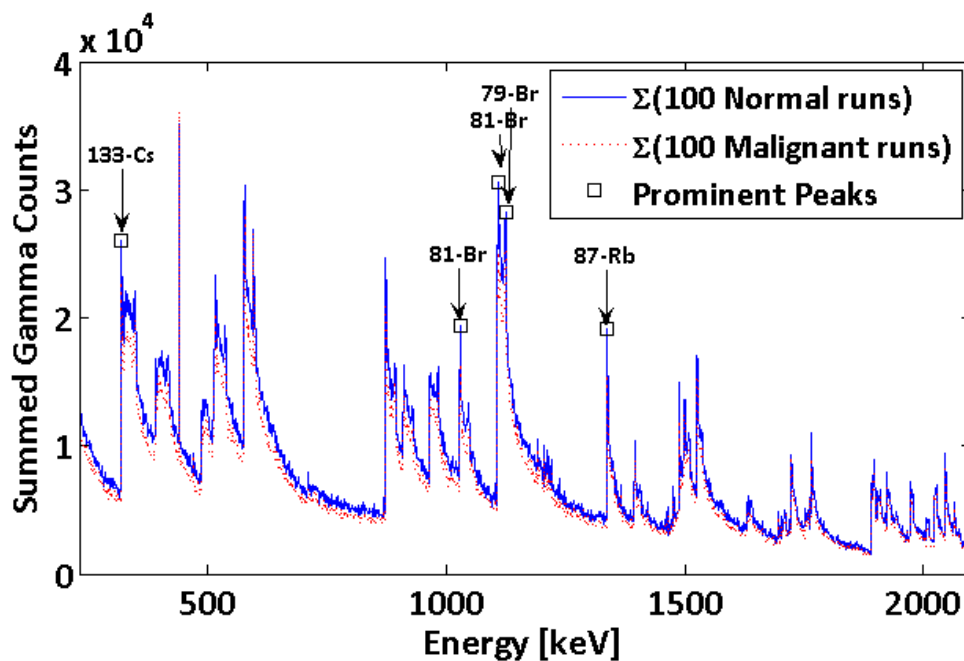


Figure 42: Combined normal (blue) and malignant (red) spectra with arrows indicating the five isotopes which were found to have high discriminatory ability. The combined spectra are shown for the 10 million incident neutron simulations. For each of the discriminatory isotopes, the normal counts exceeded the malignant counts, presumably due to the increased amount of hydrogen in the normal breast tissue model.

The dose values calculated for the neutron count levels which yielded prominent elements ranged from 0.0224 mSv to 0.112 mSv, depending on the number of incident neutrons. For 2 million neutrons, the total dose to the volume of breast tissue that was irradiated was only 0.0224 mSv, which is only a fraction of the dose reported for other breast cancer screening methods [106], and even when the number of incident neutrons is maximized to 10 million, the dose to the breast tissue still low enough to indicate NSECT's potential as a breast cancer screening technique.

A.4 Discussion

This simulation study demonstrates NSECT's feasibility to detect differences in the concentration of several discriminatory trace elements that indicate cancer in breast tissue. The results indicate that four elemental isotopes - ^{133}Cs (319 keV), ^{81}Br (1029 and 1109 keV), ^{79}Br (1124 keV), and ^{87}Rb (1338 keV) - are prominent in differentiating normal from malignant

tissue at neutron flux values corresponding to clinically relevant dose levels. ^{87}Rb achieved perfect classification at 10 million neutrons, and was able to differentiate normal and malignant tissue at a neutron flux as low as 3 million neutrons. As low neutron flux directly implies low dose, these elements are vital for a low-dose clinical implementation of NSECT for breast cancer detection and as a potential breast cancer screening modality.

Dose calculated in this study indicates that the dose from an NSECT scan for cancer detection is only a fraction of the dose delivered from a screening mammogram. The ROC analysis from this simulation study suggests that cancer detection can be achieved using 2 million incident neutrons with ^{81}Br at 1109 keV with a dose of 0.0224 mSv. Although the present work calculates the dose from a single projection image, which is not directly comparable to the dose calculated for current high-resolution screening technologies, this serves as a first-pass at estimating the dose for NSECT.

The dose value obtained in this study is calculated for a model of the breast that does not account for sources of background which would otherwise be present in the clinical scanning environment. Before translating this technique to the clinic, an expansion of this study is required to determine the performance when noise is added into the signal. Simulation experiments to model the sources of noise in a clinical environment are currently underway. This study assumes a relatively clean, low-noise signal in detecting an element peak, which results in a low dose estimate. The presence of noise in the system will raise the detection threshold, requiring a larger total concentration of the element for successful detection. Experiments to determine the detection threshold of NSECT in both simulation and clinical environments are being conducted.

From a detection point of view, a logical extension of this study is to develop a fusion classifier to test whether combining elements could be used to detect differences in normal and malignant breast tissue with greater accuracy at lower neutron fluxes. Another extension would be to perform the same set of simulations using a benign breast tissue model to test NSECT's ability to distinguish malignant from benign breast, which is of clinical interest

diagnostically. We are encouraged because our current dose estimate is only a fraction of a standard mammography dose. Thus, there is plenty of room to increase the dosage to overcome noise and still conduct an NSECT scan that is within clinically acceptable dose limits.

References

1. "Tutorial and In-Service Training for AVOXimeters 1000 and 1000E," (Nucleon, Ltd.).
2. W. Tjalma, E. Van Marck, J. Weyler, L. Dirix, A. Van Daele, G. Goovaerts, G. Albertyn, and P. van Dam, "Quantification and prognostic relevance of angiogenic parameters in invasive cervical cancer," *Br J Cancer* **78**, 170-174 (1998).
3. J. S. Lee, H. S. Kim, J. J. Jung, M. C. Lee, and C. S. Park, "Angiogenesis, cell proliferation and apoptosis in progression of cervical neoplasia," *Anal Quant Cytol Histol* **24**, 103-113 (2002).
4. N. Weidner, P. R. Carroll, J. Flax, W. Blumenfeld, and J. Folkman, "Tumor angiogenesis correlates with metastasis in invasive prostate carcinoma," *Am J Pathol* **143**, 401-409 (1993).
5. J. F. Jansen, J. A. Koutcher, and A. Shukla-Dave, "Non-invasive imaging of angiogenesis in head and neck squamous cell carcinoma," *Angiogenesis* (2010).
6. K. Maeda, Y. S. Chung, S. Takatsuka, Y. Ogawa, T. Sawada, Y. Yamashita, N. Onoda, Y. Kato, A. Nitta, Y. Arimoto, Y. Kondo, and M. Sowa, "Tumor angiogenesis as a predictor of recurrence in gastric carcinoma," *J Clin Oncol* **13**, 477-481 (1995).
7. S. C. Vieira, L. C. Zeferino, B. B. Da Silva, G. Aparecida Pinto, J. Vassallo, G. A. Carasan, and N. G. De Moraes, "Quantification of angiogenesis in cervical cancer: a comparison among three endothelial cell markers," *Gynecol Oncol* **93**, 121-124 (2004).
8. T. J. Farrell, M. S. Patterson, and B. Wilson, "A diffusion theory model of spatially resolved, steady-state diffuse reflectance for the noninvasive determination of tissue optical properties *in vivo*," *Med Phys* **19**, 879-888 (1992).
9. J. E. Phelps, K. Vishwanath, V. T. C. Chang, and N. Ramanujam, "Rapid ratiometric determination of hemoglobin concentration using UV-VIS diffuse reflectance at isosbestic wavelengths," *Opt Express* (under revision).
10. G. A. Thibodeau, and K. T. Patton, *Anatomy and Physiology* (Mosby, Inc., St. Louis, 2003).
11. M. H. Friedman, *Principles and Models of Biological Transport* (Springer, 2008).
12. G. R. Kelman, "Digital computer subroutine for the conversion of oxygen tension into saturation," *J Appl Physiol* **21**, 1375-1376 (1966).
13. G. J. Kost, ed. *Principles & Practice of Point-of-Care Testing* (Lippincott Williams & Wilkins, Philadelphia, 2002).

14. "Functional and Fractional Oxygen Saturation: A Technical Overview," (Smiths Medical PM, Inc., Waukesha).
15. A. N. Yaroslavsky, A. V. Priezzhev, J. Rodriguez, I. V. Yaroslavsky, and H. Battarbee, "Optics of Blood," in *Handbook of Optical Biomedical Diagnostics*, V. V. Tuchin, ed. (SPIE - The International Society for Optical Engineering, Bellingham, 2002).
16. S. Chandrasekhar, *Radiative Transfer* (Courier Dover Publications, 1960).
17. L. Wang, and H. Wu, *Biomedical Optics: Principles and Imaging* (John Wiley & Sons, Inc., Hoboken, 2007).
18. G. M. Palmer, and N. Ramanujam, "Monte Carlo-based inverse model for calculating tissue optical properties. Part I: Theory and validation on synthetic phantoms," *Appl Opt* **45**, 1062-1071 (2006).
19. S. J. Matcher, "Signal Quantification and Localization in Tissue Near-Infrared Spectroscopy," in *Handbook of Optical Biomedical Diagnostics*, V. V. Tuchin, ed. (SPIE - The International Society for Optical Engineering, Bellingham, 2002).
20. B. J. Tromberg, O. Coquoz, J. B. Fishkin, T. Pham, E. R. Anderson, J. Butler, M. Cahn, J. D. Gross, V. Venugopalan, and D. Pham, "Non-invasive measurements of breast tissue optical properties using frequency-domain photon migration," *Philos Trans R Soc Lond B Biol Sci* **352**, 661-668 (1997).
21. B. J. Tromberg, N. Shah, R. Lanning, A. Cerussi, J. Espinoza, T. Pham, L. Svaasand, and J. Butler, "Non-invasive in vivo characterization of breast tumors using photon migration spectroscopy," *Neoplasia* **2**, 26-40 (2000).
22. B. Yu, E. S. Burnside, G. A. Sisney, J. M. Harter, C. Zhu, A. H. Dhalla, and N. Ramanujam, "Feasibility of Near-Infrared Diffuse Optical Spectroscopy on Patients Undergoing Image-Guided Core-Needle Biopsy," *Optics Express* **15**, 7335-7350 (2007).
23. J. E. Bender, K. Vishwanath, L. K. Moore, J. Q. Brown, V. Chang, G. M. Palmer, and N. Ramanujam, "A robust Monte Carlo model for the extraction of biological absorption and scattering *in vivo*," *IEEE Trans Biomed Eng* **56**, 960-968 (2009).
24. L. Wang, S. L. Jacques, and L. Zheng, "MCML--Monte Carlo modeling of light transport in multi-layered tissues," *Comput Methods Programs Biomed* **47**, 131-146 (1995).
25. L. G. Henyey, and J. L. Greenstein, "Diffuse radiation in the galaxy," *Astrophysical Journal* **93**, 70-83 (1941).
26. R. Graaff, M. H. Koelink, F. F. M. de Mul, W. G. Zijlstra, A. C. M. Dassel, and J. G. Aarnoudse, "Condensed Monte Carlo simulations for the description of light transport," *Applied Optics* **32**, 426-434 (1993).

27. G. M. Palmer, and N. Ramanujam, "Monte-Carlo-based model for the extraction of intrinsic fluorescence from turbid media," *J Biomed Opt* **13**, 024017 (2008).
28. G. M. Palmer, C. Zhu, T. M. Breslin, F. Xu, K. W. Gilchrist, and N. Ramanujam, "Monte Carlo-based inverse model for calculating tissue optical properties. Part II: Application to breast cancer diagnosis," *Appl Opt* **45**, 1072-1078 (2006).
29. M. J. Rathbone, *Oral Mucosal Drug Delivery* (Marcel Dekker, Inc., 1996).
30. S. T. Sonis, "The pathobiology of mucositis," *Nat Rev Cancer* **4**, 277-284 (2004).
31. B. D. Fornage, and J. L. Deshayes, "Ultrasound of normal skin," *J Clin Ultrasound* **14**, 619-622 (1986).
32. J. W. McMurdy, G. D. Jay, S. Suner, and G. Crawford, "Noninvasive optical, electrical, and acoustic methods of total hemoglobin determination," *Clin Chem* **54**, 264-272 (2008).
33. Y. Mendelson, "Pulse oximetry: theory and applications for noninvasive monitoring," *Clin Chem* **38**, 1601-1607 (1992).
34. T. Ahrens, and K. Rutherford, *Essentials of oxygenation* (Jones & Bartlett Publishers, Boston, 1993).
35. M. R. Macknet, S. Norton, P. Kimbal-Jones, and R. Applegate, "Continuous noninvasive measurement of hemoglobin via pulse CO-oximetry," in *Society of Technology in Anesthesia 17th Annual Meeting*(Orlando, Florida, 2007).
36. M. R. Macknet, P. Kimball-Jones, R. Applegate, and M. Allard, "Continuous Non-Invasive Measurement of Hemoglobin via Pulse CO-oximetry During Liver Transplantation, a Case Report," *Anesthesia Analgesia* **104**, S-31 (2007).
37. R. O. Esenaliev, Y. Y. Petrov, O. Hartrumpf, D. J. Deyo, and D. S. Prough, "Continuous, noninvasive monitoring of total hemoglobin concentration by an optoacoustic technique," *Appl Opt* **43**, 3401-3407 (2004).
38. W. Secomski, A. Nowicki, P. Tortoli, and R. Olszewski, "Multigate Doppler measurements of ultrasonic attenuation and blood hematocrit in human arteries," *Ultrasound Med Biol* **35**, 230-236 (2009).
39. R. G. Nadeau, and W. Groner, "The role of a new noninvasive imaging technology in the diagnosis of anemia," *J Nutr* **131**, 1610S-1614S (2001).
40. D. A. Benaron, I. H. Parachikov, W. F. Cheong, S. Friedland, B. E. Rubinsky, D. M. Otten, F. W. H. Liu, C. J. Levinson, A. L. Murphy, J. W. Price, Y. Talmi, J. P. Weersing, J. L.

Duckworth, U. B. Horchner, and E. L. Kermit, "Design of a visible-light spectroscopy clinical tissue oximeter," *Journal of Biomedical Optics* **10**, - (2005).

41. X. Wu, S. Yeh, T. W. Jeng, and O. S. Khalil, "Noninvasive determination of hemoglobin and hematocrit using a temperature-controlled localized reflectance tissue photometer," *Anal Biochem* **287**, 284-293 (2000).

42. S. Zhang, B. R. Soller, S. Kaur, K. Perras, and T. J. Vandersalm, "Investigation of noninvasive in vivo blood hematocrit measurement using NIR reflectance spectroscopy and partial least-squares regression," *Applied Spectroscopy* **54**, 294-299 (2000).

43. J. W. McMurdy, G. D. Jay, S. Suner, F. M. Trespalacios, and G. P. Crawford, "Diffuse reflectance spectra of the palpebral conjunctiva and its utility as a noninvasive indicator of total hemoglobin," *J Biomed Opt* **11**, 014019 (2006).

44. J. Lee, J. G. Kim, S. Mahon, B. J. Tromberg, K. L. Ryan, V. A. Convertino, C. A. Rickards, K. Osann, and M. Brenner, "Tissue hemoglobin monitoring of progressive central hypovolemia in humans using broadband diffuse optical spectroscopy," *J Biomed Opt* **13**, 064027 (2008).

45. Q. Luo, S. Zeng, and B. Chance, "Monitoring of Brain Activity with Near-Infrared Spectroscopy," in *Handbook of Optical Biomedical Diagnostics*, V. V. Tuchin, ed. (SPIE - The International Society for Optical Engineering, Bellingham, 2002).

46. E. K. Chan, B. Sorg, D. Protsenko, M. O'Neil, M. Motamedi, and A. J. Welch, "Effects of Compression on Soft Tissue Optical Properties," *IEEE Journal of Selected Topics in Quantum Electronics* **2**, 943-950 (1996).

47. R. Reif, M. S. Amoroso, K. W. Calabro, O. A'Amar, S. K. Singh, and I. J. Bigio, "Analysis of changes in reflectance measurements on biological tissues subjected to different probe pressures," *J Biomed Opt* **13**, 010502 (2008).

48. Y. Ti, and W. C. Lin, "Effects of probe contact pressure on in vivo optical spectroscopy," *Opt Express* **16**, 4250-4262 (2008).

49. J. A. Delgado-Atencio, E. E. Orozco-Guillén, S. Vázquez y Montiel, M. Cunill-Rodríguez, J. Castro-Ramos, J. L. Gutiérrez, and F. Martínez, "Influence of Probe Pressure on Human Skin Diffuse Reflectance Spectroscopy Measurements," *Optical Memory and Neural Networks* **18**, 6-14 (2009).

50. A. Cerussi, S. Siavoshi, A. Durkin, C. Chen, W. Tanamai, D. Hsiang, and B. J. Tromberg, "Effect of contact force on breast tissue optical property measurements using a broadband diffuse optical spectroscopy handheld probe," *Appl Opt* **48**, 4270-4277 (2009).

51. US Department of Health and Human Services. The 2007 Nationwide Blood Collection and Utilization Survey Report. DHHS: Washington, DC (2007).

52. N. M. Dietz, M. J. Joyner, and M. A. Warner, "Blood substitutes: fluids, drugs, or miracle solutions?," *Anesth Analg* **82**, 390-405 (1996).
53. T. J. Gan, E. Bennett-Guerrero, B. Phillips-Bute, H. Wakeling, D. M. Moskowitz, Y. Olufolabi, S. N. Konstadt, C. Bradford, P. S. Glass, S. J. Machin, and M. G. Mythen, "Hextend, a physiologically balanced plasma expander for large volume use in major surgery: a randomized phase III clinical trial. Hextend Study Group," *Anesth Analg* **88**, 992-998 (1999).
54. "Practice guidelines for perioperative blood transfusion and adjuvant therapies: an updated report by the American Society of Anesthesiologists Task Force on Perioperative Blood Transfusion and Adjuvant Therapies," *Anesthesiology* **105**, 198-208 (2006).
55. J. E. Bender, A. B. Shang, E. W. Moretti, B. Yu, L. M. Richards, and N. Ramanujam, "Noninvasive monitoring of tissue hemoglobin using UV-VIS diffuse reflectance spectroscopy: a pilot study," *Opt Express* **17**, 23396-23409 (2009).
56. J. Lee, J. G. Kim, S. Mahon, B. J. Tromberg, D. Mukai, K. Kreuter, D. Saltzman, R. Patino, R. Goldberg, and M. Brenner, "Broadband diffuse optical spectroscopy assessment of hemorrhage- and hemoglobin-based blood substitute resuscitation," *J Biomed Opt* **14**, 044027 (2009).
57. B. A. Crookes, S. M. Cohn, S. Bloch, J. Amortegui, R. Manning, P. Li, M. S. Proctor, A. Hallal, L. H. Blackbourne, R. Benjamin, D. Soffer, F. Habib, C. I. Schulman, R. Duncan, and K. G. Proctor, "Can near-infrared spectroscopy identify the severity of shock in trauma patients?," *J Trauma* **58**, 806-813; discussion 813-806 (2005).
58. F. Torella, R. D. Cowley, M. S. Thorniley, and C. N. McCollum, "Regional tissue oxygenation during hemorrhage: can near infrared spectroscopy be used to monitor blood loss?," *Shock* **18**, 440-444 (2002).
59. S. Prahl, "Optical Properties Spectra," (Oregon Medical Laser Center, 2003).
60. C. Zakian, I. Pretty, R. Ellwood, and D. Hamlin, "*In vivo* quantification of gingival inflammation using spectral imaging," *J Biomed Opt* **13**, 054045 (2008).
61. Y. Ishimoto, K. Hattori, H. Ohgushi, K. Uematsu, Y. Tanikake, Y. Tanaka, and Y. Takakura, "Spectrocolorimetric evaluation of human articular cartilage," *Osteoarthritis Cartilage* **17**, 1204-1208 (2009).
62. M. Chandra, J. Scheiman, D. Simeone, B. McKenna, J. Purdy, and M. A. Mycek, "Spectral areas and ratios classifier algorithm for pancreatic tissue classification using optical spectroscopy," *J Biomed Opt* **15**, 010514 (2010).
63. R. Mallia, S. S. Thomas, A. Mathews, R. Kumar, P. Sebastian, J. Madhavan, and N. Subhash, "Oxygenated hemoglobin diffuse reflectance ratio for in vivo detection of oral pre-cancer," *J Biomed Opt* **13**, 041306 (2008).

64. R. J. Mallia, S. S. Thomas, A. Mathews, R. Kumar, P. Sebastian, J. Madhavan, and N. Subhash, "Laser-induced autofluorescence spectral ratio reference standard for early discrimination of oral cancer," *Cancer* **112**, 1503-1512 (2008).
65. S. L. Jacques, I. S. Saidi, and F. K. Tittel, "Average depth of blood vessels in skin and lesions deduced by optical fiber spectroscopy," *SPIE Proceedings of Laser Surgery: Advanced Characterization, Therapeutics, and Systems IV* **2128**, 231-237 (1994).
66. I. Nishidate, Y. Aizu, and H. Mishina, "Depth visualization of a local blood region in skin tissue by use of diffuse reflectance images," *Opt Lett* **30**, 2128-2130 (2005).
67. I. Nishidate, T. Maeda, Y. Aizu, and K. Niizeki, "Visualizing depth and thickness of a local blood region in skin tissue using diffuse reflectance images," *J Biomed Opt* **12**, 054006 (2007).
68. M. L. Ellsworth, R. N. Pittman, and C. G. Ellis, "Measurement of hemoglobin oxygen saturation in capillaries," *Am J Physiol* **252**, H1031-1040 (1987).
69. R. N. Pittman, and B. R. Duling, "A new method for the measurement of percent oxyhemoglobin," *J Appl Physiol* **38**, 315-320 (1975).
70. Q. Liu, and T. Vo-Dinh, "Spectral filtering modulation method for estimation of hemoglobin concentration and oxygenation based on a single fluorescence emission spectrum in tissue phantoms," *Med Phys* **36**, 4819-4829 (2009).
71. T. M. Breslin, F. Xu, G. M. Palmer, C. Zhu, K. W. Gilchrist, and N. Ramanujam, "Autofluorescence and diffuse reflectance properties of malignant and benign breast tissues," *Ann Surg Oncol* **11**, 65-70 (2004).
72. S. Prahl, "Mie Scattering Program," (Oregon Medical Laser Center, 2005).
73. E. L. Hull, M. G. Nichols, and T. H. Foster, "Quantitative broadband near-infrared spectroscopy of tissue-simulating phantoms containing erythrocytes," *Phys Med Biol* **43**, 3381-3404 (1998).
74. E. L. Hull, and T. H. Foster, "Noninvasive near-infrared hemoglobin spectroscopy for in vivo monitoring of tumor oxygenation and response to oxygen modifiers," *Proceedings SPIE* **2979**, 355-364 (1997).
75. W. S. Rasband, "ImageJ," (U. S. National Institutes of Health, Bethesda, Maryland, USA, 1997-2004).
76. Q. Liu, and N. Ramanujam, "Scaling method for fast Monte Carlo simulation of diffuse reflectance spectra from multilayered turbid media," *J Opt Soc Am A Opt Image Sci Vis* **24**, 1011-1025 (2007).

77. T. M. Bydlon, S. A. Kennedy, L. M. Richards, J. Q. Brown, B. Yu, M. K. Junker, J. Gallagher, J. Geradts, L. G. Wilke, and N. Ramanujam, "Performance metrics of an optical spectral imaging system for intra-operative assessment of breast tumor margins," *Opt Express* **18**, 8058-8076 (2010).
78. B. R. Duling, and C. Desjardins, "Capillary hematocrit-what does it mean?," *News Physiol. Sci.* **2**, 66-69 (1987).
79. R. D. Braun, M. W. Dewhirst, and D. L. Hatchell, "Quantification of erythrocyte flow in the choroid of the albino rat," *Am J Physiol* **272**, H1444-1453 (1997).
80. R. R. Anderson, and J. A. Parrish, "The optics of human skin," *J Invest Dermatol* **77**, 13-19 (1981).
81. R. Nossal, J. Kiefer, G. H. Weiss, R. Bonner, H. Taitelbaum, and S. Havlin, "Photon migration in layered media," *Applied Optics* **27**, 3382-3391 (1988).
82. R. A. Capobianco, "Xenon: The Full Spectrum vs. Deuterium Plus Tungsten," (PerkinElmer, 2003).
83. G. H. Weiss, and J. E. Kiefer, "A numerical study of the statistics of penetration depth of photons reemitted from irradiated media," *J Modern Opt* **45**, 2327-2337 (1998).
84. B. W. Pogue, and M. S. Patterson, "Review of tissue simulating phantoms for optical spectroscopy, imaging and dosimetry," *J Biomed Opt* **11**, 041102 (2006).
85. T. H. Pham, O. Coquoz, J. B. Fishkin, E. Anderson, and B. J. Tromberg, "Broad bandwidth frequency domain instrument for quantitative tissue optical spectroscopy," *Review of Scientific Instruments* **71**, 2500-2513 (2000).
86. J. Y. Lo, B. Yu, H. L. Fu, J. E. Bender, G. M. Palmer, T. F. Kuech, and N. Ramanujam, "A strategy for quantitative spectral imaging of tissue absorption and scattering using light emitting diodes and photodiodes," *Opt Express* **17**, 1372-1384 (2009).
87. B. Yu, J. Y. Lo, T. F. Kuech, G. M. Palmer, J. E. Bender, and N. Ramanujam, "Cost-effective diffuse reflectance spectroscopy device for quantifying tissue absorption and scattering *in vivo*," *J Biomed Opt* **13**, 060505 (2008).
88. J. R. Mourant, T. Fuselier, J. Boyer, T. M. Johnson, and I. J. Bigio, "Predictions and measurements of scattering and absorption over broad wavelength ranges in tissue phantoms," *Appl Opt* **36**, 949-957 (1997).
89. V. T. Chang, P. S. Cartwright, S. M. Bean, G. M. Palmer, R. C. Bentley, and N. Ramanujam, "Quantitative physiology of the precancerous cervix *in vivo* through optical spectroscopy," *Neoplasia* **11**, 325-332 (2009).

90. B. Yu, H. Fu, T. Bydlon, J. E. Bender, and N. Ramanujam, "Diffuse reflectance spectroscopy with a self-calibrating fiber optic probe," *Opt Lett* **33**, 1783-1785 (2008).
91. M. G. Mythen, and A. R. Webb, "Intra-operative gut mucosal hypoperfusion is associated with increased post-operative complications and cost," *Intensive Care Med* **20**, 99-104 (1994).
92. J. E. Bender, A. J. Kapadia, A. C. Sharma, G. D. Tourassi, B. P. Harrawood, and C. E. Floyd, Jr., "Breast cancer detection using neutron stimulated emission computed tomography: prominent elements and dose requirements," *Med Phys* **34**, 3866-3871 (2007).
93. C. E. Floyd, Jr., J. E. Bender, A. C. Sharma, A. Kapadia, J. Xia, B. Harrawood, G. D. Tourassi, J. Y. Lo, A. Crowell, and C. Howell, "Introduction to neutron stimulated emission computed tomography," *Phys Med Biol* **51**, 3375-3390 (2006).
94. C. E. Floyd, Jr., A. J. Kapadia, J. E. Bender, A. C. Sharma, J. Q. Xia, B. P. Harrawood, G. D. Tourassi, J. Y. Lo, A. S. Crowell, M. R. Kiser, and C. R. Howell, "Neutron-stimulated emission computed tomography of a multi-element phantom," *Phys Med Biol* **53**, 2313-2326 (2008).
95. C. E. Floyd, A. C. Sharma, J. E. Bender, A. Kapadia, J. Q. Xia, B. P. Harrawood, G. D. Tourassi, J. Y. Lo, M. R. Kiser, A. S. Crowell, R. S. Pedroni, R. A. Macri, S. Tajiima, and C. R. Howell, "Neutron stimulated emission computed tomography: Background corrections," *Nucl Instrum Meth B* **254**, 329-336 (2007).
96. A. N. Garg, V. Singh, R. G. Weginwar, and V. N. Sagdeo, "An elemental correlation study in cancerous and normal breast tissue with successive clinical stages by neutron activation analysis," *Biol Trace Elem Res* **46**, 185-202 (1994).
97. K. H. Ng, D. A. Bradley, L. M. Looi, C. S. Mahmood, and A. K. Wood, "Differentiation of elemental composition of normal and malignant breast tissue by instrumental neutron activation analysis" *Appl Radiat Isotopes* **44**, 511-516 (1993).
98. S. L. Rizk, and H. H. Sky-Peck, "Comparison between concentrations of trace elements in normal and neoplastic human breast tissue," *Cancer Res* **44**, 5390-5394 (1984).
99. A. E. Schwartz, G. W. Leddicotte, R. W. Fink, and E. W. Friedman, "Trace elements in normal and malignant human breast tissue," *Surgery* **76**, 325-329 (1974).
100. "Cross Section Evaluation Working Group, ENDEIB-VI Summary Documentaion, Report BNL-NCS-17541 (ENDF-201)," (National Nuclear Data Center, Brookhave National Laboratory, Upton, 1991).
101. K. H. Ng, D. A. Bradley, and L. M. Looi, "Elevated trace element concentrations in malignant breast tissues," *Br J Radiol* **70**, 375-382 (1997).

102. G. Ullman, M. Sandborg, R. Hunt, D. R. Dance, and G. A. Carlsson, "Implementation of pathologies in the Monte Carlo model in chest and breast imaging," (2003).
103. C. E. Metz, B. A. Herman, and J. H. Shen, "Maximum likelihood estimation of receiver operating characteristic (ROC) curves from continuously-distributed data," *Stat Med* **17**, 1033-1053 (1998).
104. J. E. Turner, *Atoms, Radiation, and Radiation Protection* (John Wiley & Sons, Inc., New York, NY, 1995).
105. "International Commission on Radiological Protection, 1990 recommendations of the International Commission on Radiological Protection," (Oxford, 1991).
106. J. Law, "The development of mammography," *Phys Med Biol* **51**, R155-167 (2006).

Biography

Name: Janelle Elise Phelps (maiden name Janelle Bender)

Date of Birth: February 25, 1982

Place of Birth: Downingtown, Pennsylvania

Education

Duke University, Durham, North Carolina

Ph.D. in Biomedical Engineering, September 2010

Rice University, Houston, Texas

B.S. in Bioengineering, May 2004

Publications

Peer-Reviewed

- **J. E. Phelps**, K. Vishwanath, V. Chang, N. Ramanujam, “Rapid ratiometric determination of hemoglobin concentration using UV-VIS diffuse reflectance at isosbestic wavelengths,” *Optics Express*, under revision.
- K. Vishwanath, K. Chang, D. Klein, V. Chang, Y. F. Deng, **J. E. Phelps**, N. Ramanujam, “Portable Fiber Based Diffuse Reflectance Spectroscopy Systems for Estimating Tissue Optical Parameters,” submitted, 2010.
- S. Millon, J. Ostrander, S. Yazdanfar, Q. Brown, **J. Bender**, A. Rajeha, N. Ramanujam, “Preferential Accumulation of 5-Aminolevulinic Acid-Induced Protoporphyrin IX in Breast Cancer: A Comprehensive Study on Six Breast Cell Lines with Varying Phenotypes,” *Journal of Biomedical Optics* 15(1), Jan. 2010.
- **J. E. Bender**, A. B. Shang, E. W. Moretti, B. Yu, L. M. Richards, N. Ramanujam, “Noninvasive Monitoring of Tissue Hemoglobin Using UV-VIS Diffuse Reflectance Spectroscopy: A Pilot Study,” *Optics Express* 17(26), 23396-23409, Dec. 2009 (Selected for publication in the *Virtual Journal for Biomedical Optics* 5(1), 2010).
- **J. E. Bender**, K. Vishwanath, L. K. Moore, J. Q. Brown, V. Chang, G. M. Palmer, N. Ramanujam, “A Robust Monte Carlo Model for the Extraction of Biological Absorption and Scattering *in Vivo*,” *IEEE Transactions on Biomedical Engineering* 56(4), 960-968, Apr. 2009.
- J. Y. Lo, B. Yu, H. L. Fu, **J. E. Bender**, G. M. Palmer, T. F. Kuech, N. Ramanujam, “A Strategy for Quantitative Spectral Imaging of Tissue Absorption and Scattering Using Light Emitting Diodes and Photodiodes,” *Optics Express* 17(3), 1372-1384, Feb. 2009.
- B. Yu, J. Y. Lo, T. F. Kuech, G. M. Palmer, **J. E. Bender**, N. Ramanujam, “Cost-Effective Diffuse Reflectance Spectroscopy Device for Quantifying Tissue Absorption and Scattering *in Vivo*,” *Journal of Biomedical Optics* 13(16), 060505, Nov./Dec. 2008.
- B. Yu, H. Fu, T. Bydlon, **J. E. Bender**, N. Ramanujam, “Diffuse Reflectance Spectroscopy with a Self-Calibrating Fiber Optic Probe,” *Optics Letters* 33(16), 1783-1786, Aug. 2008.

- C. E. Floyd Jr., A. J. Kapadia, **J. E. Bender**, A. C. Sharma, J. Q. Xia, B. P. Harrawood, G. D. Tourassi, J. Y. Lo, A. S. Crowell, M. R. Kiser, C. R. Howell, "Neutron Stimulated Emission Computed Tomography of a Multi-Element Phantom," *Physics in Medicine and Biology* 53, 2313-2326, May 2008.
- A. J. Kapadia, A. C. Sharma, **J. E. Bender**, G. D. Tourassi, C. R. Howell, A. S. Crowell, M. R. Kiser, B. P. Harrawood, C. E. Floyd, Jr., "Neutron Stimulated Emission Computed Tomography for Diagnosis of Breast Cancer," *IEEE Transactions on Nuclear Science* 55(1), 501-509, Feb. 2008.
- **J. E. Bender**, A. J. Kapadia, A. C. Sharma, G. D. Tourassi, B. P. Harrawood, C. E. Floyd, Jr., "Breast Cancer Detection Using Neutron Stimulated Emission Computed Tomography: Prominent Elements and Dose Requirements," *Medical Physics* 34(10), 3866-3871, Oct. 2007.
- A. C. Sharma, B. P. Harrawood, **J. E. Bender**, G. D. Tourassi, A. J. Kapadia, "Neutron Stimulated Emission Computed Tomography: A Monte Carlo Simulation Approach," *Physics in Medicine and Biology* 52, 6117-6131, Oct. 2007.
- A. C. Sharma, G. D. Tourassi, A. J. Kapadia, B. P. Harrawood, **J. E. Bender**, A. S. Crowell, M. R. Kiser, C. R. Howell, C. E. Floyd, "Design and Development of a High-Energy Gamma Camera for Use with NSECT Imaging: Feasibility for Breast Imaging," *IEEE Transactions on Nuclear Science* 54(5), 1498-1505, Oct. 2007.
- C. E. Floyd Jr., A. C. Sharma, **J. E. Bender**, A. J. Kapadia, J. Q. Xia, B. P. Harrawood, G. D. Tourassi, J. Y. Lo, M. R. Kiser, A. S. Crowell, R. S. Pedroni, R. A. Macri, S. Tajima, C. R. Howell, "Neutron Stimulated Emission Computed Tomography: Background Corrections," *Nuclear Instruments and Methods in Physics Research Section B* 254(2), 329-336, Jan. 2007.
- C. E. Floyd, **J. E. Bender**, A. C. Sharma, A. J. Kapadia, J. Q. Xia, B. P. Harrawood, G. D. Tourassi, J. Y. Lo, A. S. Crowell, C. R. Howell, "Introduction to Neutron Stimulated Emission Computed Tomography," *Phys. Med. Biol.* 51, 3375-3390, Jul. 2006 (Selected for abstract in the "Yearbook of Nuclear Medicine").
- A. M. Wang, **J. E. Bender**, J. Pfefer, U. Utzinger, R. A. Drezek, "Depth-Sensitive Reflectance Measurements Using Obliquely Oriented Fiber Probes," *Journal of Biomedical Optics* 10(4), 044017, Aug. 2005.

Conference Proceedings

- **J. E. Bender**, B. Yu, L. M. Richards, A. B. Shang, E. W. Moretti, N. Ramanujam, "Noninvasive Monitoring of Blood Loss Using Diffuse Reflectance Spectroscopy: A Preliminary Patient Study," *Engineering Conferences International: Advances in Optics for Biotechnology, Medicine, and Surgery XI*, Burlington, VT, Jun. 2009.
- **J. E. Bender**, L. K. Moore, K. V. Vishwanath, N. Ramanujam, "Factors Influencing the Accuracy of Determining Tissue Physiology Quantitatively Using Optical Spectroscopy," *Optical Society of America: Biomedical Optics Topical Meeting*, St. Petersburg, FL, Mar. 2008.
- K. Vishwanath, H. Yuan, L. Moore, **J. Bender**, M. Dewhirst, N. Ramanujam, "Longitudinal Monitoring of 4T1-Tumor Physiology *in Vivo* with Doxorubicin Treatment via Diffuse Optical Spectroscopy," *Optical Society of America: Biomedical Optics Topical Meeting*, St. Petersburg, FL, Mar. 2008.

- A. J. Kapadia, A. C. Sharma, G. D. Tourassi, **J. E. Bender**, C. R. Howell, A. S. Crowell, M. R. Kiser, C. E. Floyd, Jr., “Non-Invasive Estimation of Potassium (³⁹K) in Bovine Liver Using Neutron Stimulated Emission Computed Tomography (NSECT),” Proceedings of the 2006 IEEE NSS-MIC, San Diego, CA, Nov. 2006.
- A. J. Kapadia, A. C. Sharma, G. D. Tourassi, **J. E. Bender**, C. R. Howell, A. S. Crowell, M. R. Kiser, C. E. Floyd, Jr., “Neutron Spectroscopy of Mouse Using Neutron Stimulated Emission Computed Tomography (NSECT),” Proceedings of the 2006 IEEE NSS-MIC, San Diego, CA, Nov. 2006.
- A. J. Kapadia, A. C. Sharma, G. D. Tourassi, **J. E. Bender**, C. R. Howell, A. S. Crowell, M. R. Kiser, C. E. Floyd, Jr., “Neutron Stimulated Emission Computed Tomography (NSECT) for Early Detection of Breast Cancer,” Proceedings of the 2006 IEEE NSS-MIC, San Diego, CA, Nov. 2006.
- A. C. Sharma, G. D. Tourassi, A. J. Kapadia, **J. E. Bender**, J. Q. Xia, B. P. Harrawood, A. S. Crowell, M. R. Kiser, C. R. Howell, C. E. Floyd, Jr., “Development of a High-Energy Gamma Camera for Use with NSECT Imaging of the Breast,” Proceedings of the 2006 IEEE NSS-MIC, San Diego, CA, Nov. 2006.
- A. C. Sharma, G. D. Tourassi, A. J. Kapadia, B. P. Harrawood, **J. E. Bender**, A. S. Crowell, M. R. Kiser, C. R. Howell, C. E. Floyd, Jr., “Design and Construction of a Prototype Rotation Modulation Collimator for near-Field High-Energy Spectroscopic Gamma Imaging,” Proceedings of the 2006 IEEE NSS-MIC, San Diego, CA, Nov. 2006.
- **J. E. Bender**, C. E. Floyd, Jr., B. P. Harrawood, A. J. Kapadia, A. C. Sharma, J. L. Jesneck, “The Effect of Detector Resolution for Quantitative Analysis of Neutron Stimulated Emission Computed Tomography,” Proceedings of the 2006 SPIE Symposium on Medical Imaging, vol. 6142, 1597-1605, Mar. 2006.
- C. E. Floyd, Jr., **J. E. Bender**, A. J. Kapadia, A. C. Sharma, B. P. Harrawood, G. D. Tourassi, J. Y. Lo, C. Howell, “Breast Cancer Diagnosis Using Neutron Simulated Emission Computed Tomography: Dose and Count Requirements,” Proceedings of the 2006 SPIE Symposium on Medical Imaging, vol. 6142, 597-603, Mar. 2006.
- A. C. Sharma, C. E. Floyd, Jr., B. P. Harrawood, G. D. Tourassi, A. J. Kapadia, **J. E. Bender**, J. Y. Lo, C. Howell, “Rotating Slit Collimator Design for High-Energy Near-Field Imaging,” Proceedings of the 2006 SPIE Symposium on Medical Imaging, vol. 6142, 405-413, Mar. 2006.
- A. J. Kapadia, C. E. Floyd, Jr., **J. E. Bender**, C. R. Howell, A. S. Crowell, M. R. Kiser, “Non-Invasive Quantification of Iron (⁵⁶Fe) in Beef Liver Using Neutron Stimulated Emission Computed Tomography,” Proceedings of the 2005 IEEE Nuclear Science Symposium, Medical Imaging Conference, vol. 4, 2232-2234, Oct. 2005.
- A. M. Wang, **J. E. Bender**, T. J. Pfefer, U. Utzinger, R. A. Drezek, “Depth-Sensitive Reflectance Measurements Using Obliquely Oriented Fiber Probes,” Proceedings of the 2005 SPIE Symposium, Photonics West, Biomedical Optics, vol. 5691, 54-65, Mar. 2005.

Conference Presentations

- “Noninvasive Monitoring of Blood Loss Using Diffuse Reflectance Spectroscopy: A Preliminary Patient Study,” poster presentation at Engineering Conferences International: Advances in Optics for Biotechnology, Medicine, and Surgery XI 28 Jun.-3 Jul. 2009 Burlington, VT.

- "Factors Influencing the Accuracy of Determining Tissue Physiology Quantitatively Using Optical Spectroscopy," poster presentation at Optical Society of America: Biomedical Optics Topical Meeting 16-20 Mar. 2008 St. Petersburg, FL.
- "Breast Cancer Diagnosis Using Neutron Stimulated Emission Computed Tomography: Dose and Count Requirements," oral presentation at SPIE Medical Imaging Conference 11-16 Feb. 2006 San Diego, CA.
- "The Effect of Detector Resolution for Quantitative Analysis of Neutron Stimulated Emission Computed Tomography," poster presentation at SPIE Medical Imaging Conference 11-16 Feb. 2006 San Diego, CA.

Grants and Awards

- NIH Training Grant EB001040-01, 2004-2006
- Yearbook of Nuclear Medicine Abstract Selection: Publication titled "Introduction to Neutron Stimulated Emission Computed Tomography" selected for abstraction, 2006

Professional Affiliations

- Member of Optical Society of America (OSA), January 2008-present
- Member of International Society of Optical Engineering (SPIE), March 2005-present